Scuola di Dottorato di Ricerca in Fisica

XXXVIII ciclo

Programa de doctorado en tecnología nuclear 2023

A multiscale dosimetric approach to BNCT for Glioblastoma Multiforme: a theoretical and experimental journey from cell microdosimetry to patient treatment

Dissertation submitted by

Barbara Marcaccio

Submitted to the Graduate School of Physics and to the Instituto Dan Beninson in partial fulfillment of the requirements for the degree of
DOCTOR IN PHYSICS
at the University of Pavia (Italy)
and
DOCTOR IN NUCLEAR TECHNOLOGY
at the National University of San Martín (Argentina)

Supervisors

Prof. Silva Bortolussi - Prof. Sara González

Co-Supervisors

Prof. Ian Postuma - Prof. Agustina Portu

Fa sempre, ... , che in ogni seme,
ci sia un fiore, che torni poi a sbocciare,
così l'uomo amando le sue pene,
troverà un senso per vivere e sognare.

Massimo Marcaccio

A papone

Contents

LIST OF ABBREVIATIONS

GBM	Glioblastoma Multiforme
BBB	Blood–Brain Barrier
MSGs	Mutational Subgroups
RT	Radiotherapy
3D-CRT	Three-Dimensional Conformal Radiotherapy
CT	Computed Tomography
MRI	Magnetic Resonance Imaging
IMRT	Intensity-Modulated Radiotherapy
SRS	Stereotactic Radiosurgery
FSRT	Fractionated Stereotactic Radiotherapy
BNCT	Boron Neutron Capture Therapy
LET	Linear Energy Transfer
KERMA	Kinetic Energy Released per unit MAss
TCP	Tumor Control Probability
BPA	Boronophenylalanine
BSH	Borocaptate Sodium
MM	Malignant Melanoma
RFQ	Radiofrequency Quadrupole accelerator
INFN	Istituto Nazionale Fisica Nucleare
ANTHEM	AdvaNced Technologies for Human-centrEd Medicine
TESQ	Tandem-ElectroStatic- Quadrupole
BSA	Beam Shaping Assembly
nGBM	Newly diagnosed Glioblastoma Multiforme
rGBM	Recurrent Glioblastoma Multiforme
OS	Overall Survival
PFS	Progression-Free Survival
RFS	Recurrence-Free Survival
DNA	Deoxyribonucleic Acid
DSB	Double-Strand Break
RBE	Relative Biological Effectiveness
CBE	Compound Biological Effectiveness

LQ	Linear–Quadratic model
TDRA	Dual Theory of Radiation Action
SLD	Sublethal Damage
HSEF	Hit Size Effectiveness Function
MDCF	Microscopic Dose Correction Factor
SMK	Microdosimetric Kinetic Model
SSNTD	Solid State Nuclear Track Detector
NTD	Nuclear Track Detector
PBS	Phosphate Buffered Saline
GSM	Gliosarcoma
CPE	Charged Particle Equilibrium
DVH	Dose Volume Histogram
DMEM	Dulbecco's Modified Eagle Medium
FBS	Fetal Bovine Serum
PBS	Phosphate-Buffered Saline
KOH	Potassium hydroxide
RTD	Relative Track Density
FDG	luoroDeoxyglucose
1y-PFS	1-year Progression-Free Survival
OTT	Overall Treatment Time
BED	Biologically Effective Dose
EUD	Equivalent Uniform Dose

ABSTRACT

Boron Neutron Capture Therapy (BNCT) is a cancer radiotherapy based on the selective accumulation of boron in tumor cells and on the successive irradiation of the patients with a beam of low-energy neutrons. The rationale for the therapeutic action is the high cross section of neutron capture in the isotope 10-boron (^{10}B). When neutrons are captured in boron, high-linear energy transfer particles are released within micrometric ranges, causing lethal damage to cancer cells while sparing surrounding healthy tissues. This selectivity makes BNCT a promising option for treating brain tumors characterized by infiltrated cells, such as Glioblastoma Multiforme (GBM). The presented work was developed in the frame of a collaboration between Italy and Argentina in BNCT, and it is relevant for the plans to develop the clinical application of this therapy in the two countries.
The capacity to administer a safe and effective treatment requires a precise dose calculation in tumor and healthy tissues. BNCT dosimetry involves multiple radiation components with different biological effectiveness, and the absorbed dose alone does not uniquely describe the biological effect. To enable a comparison with conventional radiotherapy and predict the clinical outcomes, it is thus necessary to translate BNCT dose into photon equivalent units.
The first part of this thesis describes the development of a Photon Isoeffective Dose Model for GBM, supported by ad hoc radiobiological data. Clonogenic assays were performed on U-87 GBM cells irradiated with photons, neutrons, and neutrons in the presence of boron (BNCT). Survival curves were fitted with a modified linear quadratic model including sublethal damage repair and synergism between radiations. The resulting radiobiological parameters were used to construct the Photon Isoeffective Dose Model and applied to a clinical case of GBM treated in Taiwan. Results showed that Photon Isoeffective Dose values differ by up to 32% depending on the photon reference radiation and were on average 17% lower than the estimates obtained with the model currently employed in clinical trials.
The second part of this work zooms into the subcellular dimension, measuring and analyzing boron-10 microdistribution in U-87 cells. For the first time, using neutron autoradiography, boron was imaged in a GBM cell population, showing that it preferentially accumulates in the nucleus. These data were used to develop a *Mi-*

crodosimetric Photon Isoeffective Dose Model, explicitly accounting for the stochastic nature of energy deposition associated with intracellular boron distribution via a correction factor for the boron dose. The experimental nucleus-to-cytoplasm boron concentration ratio was described by a lognormal random variable, consistent with other biological uptake processes. The correction factor was applied to the dosimetry of U-87 radiobiological data to obtain updated radiobiological parameters. The subcellular-scale effects were thus integrated into the Photon Isoeffective Dose formalism and applied to a clinical case of GBM. Applied to U-87 data, these corrections led to a 47% reduction of the Compound Biological Effectiveness, the parameter that relates the effectiveness of BNCT compared to that of photon irradiation at the same fixed biological endpoint. This means that neglecting subcellular distribution substantially overestimates the boron dose. When applied to the clinical case, the total dose differed only by 4%, compared to conventional dosimetry. However, perturbation analyses indicated that under higher intracellular heterogeneity, plausible *in vivo*, the deviations could become substantial, up to 22%. The conclusion of this part of the work is that connecting biological effects to a dosimetric quantity requires accounting for the microdistribution of boron, which highlights the intrinsic complexity of BNCT dosimetry.
In the final part of this thesis, a preliminary model of 1-year Progression-Free Survival (1y-PFS) was developed, a figure of merit commonly used in clinical practice to evaluate treatment efficacy in GBM. A model for photon radiotherapy in a fractionated regimen was adapted to the single-fraction BNCT scenario. The proposed dose models, together with the one-year PFS model, were finally applied to two clinical cases of GBM patients treated with BNCT in China. The 1y-PFS model proved to be a suitable figure of merit for assessing the clinical relevance of the dosimetric differences observed in the clinical cases presented in this work.
Overall, this thesis provides the first set of radiobiological parameters for Photon Isoeffective Dose Model in BNCT of GBM, introduces a microdosimetric extension based on experimentally derived boron distributions and shows how to apply these tools to treatment planning, allowing a prediction of the clinical outcome. The proposed framework improves the accuracy and personalization of BNCT treatment planning with the ambition to contribute to the design of future clinical protocols.

ABSTRACT (ITALIAN)

La *Boron Neutron Capture Therapy* (BNCT) è una forma di radioterapia oncologica basata sull'accumulo selettivo del boro nelle cellule tumorali e sul successivo irraggiamento del paziente con un fascio di neutroni a bassa energia. Il principio terapeutico si fonda sull'elevata sezione d'urto per la cattura dei neutroni da parte dell'isotopo 10-boro (^{10}B). La cattura neutronica produce due particelle cariche ad alto trasferimento lineare di energia (LET) che depositano la loro energia su distanze micrometriche, causando danni letali alle cellule tumorali e risparmiando i tessuti sani circostanti. Questa selettività rende la BNCT un'opzione promettente per il trattamento di tumori cerebrali caratterizzati da cellule infiltranti, come il Glioblastoma Multiforme (GBM).
Il lavoro presentato è stato sviluppato nell'ambito di una collaborazione tra Italia e Argentina nel campo della BNCT, ed è rilevante per i piani di sviluppo clinico di questa terapia in entrambi i paesi.
La capacità di somministrare un trattamento BNCT sicuro ed efficace richiede un calcolo preciso della dose nei tessuti tumorali e in quelli sani. La dosimetria in BNCT coinvolge molteplici componenti di radiazione con diversa efficacia biologica, e la sola quantità della dose assorbita non descrive in modo univoco l'effetto biologico. Per consentire un confronto con la radioterapia convenzionale e prevedere i risultati clinici, è quindi necessario tradurre la dose BNCT in unità equivalenti ai fotoni. La prima parte di questa tesi descrive lo sviluppo del *Phonton Isoeffective Dose Model* per il GBM, supportato da dati radiobiologici generati appositamente. Le curve di sopravvivenza cellulare sono state ottenute mediante test clonogenici sulla linea cellulare U-87 (GBM umano) irraggiate con fotoni, neutroni e neutroni in presenza di boro (BNCT). Le curve sono state fittate mediante un modello lineare-quadratico modificato, che include la riparazione dei danni subletali e la sinergia tra le radiazioni. I parametri radiobiologici risultanti sono stati utilizzati per costruire il modello, applicato infine a un caso clinico di GBM trattato con BNCT a Taiwan.
I risultati mostrano che i valori della dose equivalente a fotoni differiscono fino al 32% a seconda della radiazione di riferimento scelta e risultano in media inferiori del 17% rispetto alle stime ottenute con il modello attualmente utilizzato nei trials

clinici.
La seconda parte di questo lavoro si concentra sulla scala subcellulare, misurando e analizzando la microdistribuzione del boro-10 nelle cellule U-87. Per la prima volta, utilizzando l'autoradiografia neutronica, è stato ottenuta la distribuzione del boro in una popolazione di cellule GBM, dimostrando un accumulo preferenziale nel nucleo. Questi dati sono stati impiegati per alimentare il modello microdosimetrico di dose isoeffettiva. Questo modello tiene conto della natura stocastica del deposito di energia associato alla distribuzione intracellulare del boro, tramite un fattore di correzione della componente di dose boro. Il rapporto sperimentale tra la concentrazione di boro nel nucleo e quella nel citoplasma è stato descritto mediante una variabile casuale lognormale, in linea con altri processi di assorbimento biologico.
Il fattore di correzione è stato applicato alla dosimetria dei dati radiobiologici U-87 per ottenere parametri radiobiologici corretti. Gli effetti su scala subcellulare sono stati quindi integrati nel formalismo della dose isoeffettiva a fotoni e applicati a un caso clinico di GBM.
Queste correzioni hanno portato a una riduzione del 47% del Compound Biological Effectiveness (CBE), parametro correlato all'efficacia della BNCT rispetto all'irraggiamento con fotoni a partià di effetto biologico. Ciò indica che trascurare la distribuzione subcellulare comporta una sostanziale sovrastima della dose boro. Quando applicata al caso clinico, la dose totale differisce solo del 4% rispetto alla dosimetria convenzionale. Tuttavia, le analisi di perturbazione hanno mostrato che, in presenza di una maggiore eterogeneità intracellulare, plausibile *in vivo*, le deviazioni raggiungono un 22% di differenza. La conclusione di questa parte del lavoro è che gli effetti biologici vadano correlati a una grandezza dosimetrica che consideri la microdistribuzione del boro, evidenziando la complessità intrinseca della dosimetria BNCT.
Nella parte finale di questa tesi è stato sviluppato un modello preliminare di *Progression Free Survival* a 1 anno (1y-PFS), parametro utilizzato nella pratica clinica per valutare l'efficacia del trattamento nel GBM. Un modello sviluppato per la radioterapia fotonica in regime frazionato è stato adattato allo scenario BNCT a singola frazione. I modelli di dose proposti, insieme al modello 1y-PFS, sono stati applicati a due casi clinici di pazienti affetti da GBM trattati con BNCT in Cina. Il modello 1y-PFS si è dimostrato uno strumento adeguato per valutare la rilevanza clinica dei diversi modelli dosimetrici proposti.
Nel complesso, questa tesi fornisce la prima serie di parametri radiobiologici per il modello di dose isoeffettiva ai fotoni nella BNCT del GBM, inoltre introduce un'estensione microdosimetrica basata su distribuzioni di boro derivate sperimentalmente e mostra come applicare questi strumenti alla pianificazione del trattamento, consentendo una previsione dell'esito clinico. Il quadro di strumenti sviluppati migliora l'accuratezza e la personalizzazione della pianificazione della BNCT, con l'ambizione di contribuire alla progettazione di futuri protocolli clinici.

ABSTRACT (SPANISH)

La terapia por captura neutrónica en boro (BNCT, por sus siglas en inglés, Boron Neutron Capture Therapy) es una radioterapia basada en la acumulación selectiva de boro en las células tumorales y en la irradiación sucesiva de los pacientes con un haz de neutrones de baja energía. La base de la acción terapéutica es la alta sección eficaz de captura de los neutrones en el isótopo 10-boro (^{10}B). Cuando los neutrones son capturados por el boro, se liberan partículas de alta transferencia de energía lineal en rangos micrométricos, lo que causa un daño letal a las células cancerosas sin afectar a los tejidos sanos circundantes. Esta selectividad hace que BNCT sea una opción prometedora para el tratamiento de tumores cerebrales caracterizados por células infiltrantes, como el Glioblastoma Multiforme (GBM).
El presente trabajo se desarrolló en el marco de una colaboración entre Italia y Argentina en el ámbito de BNCT, y es relevante para los proyectos en desarrollo de la aplicación clínica de esta terapia en ambos países.
La capacidad de administrar un tratamiento BNCT seguro y eficaz requiere un cálculo preciso de la dosis en los tejidos tumorales y sanos. La dosimetría en BNCT implica múltiples componentes de radiación con diferente eficacia biológica, y la dosis absorbida por sí sola no describe de manera unívoca el efecto biológico. Por lo tanto, para poder compararla con la radioterapia convencional y predecir los resultados clínicos, es necesario traducir la dosis de BNCT a unidades equivalentes a fotones.
La primera parte de esta tesis describe el desarrollo del modelo de *Dosis Isoefectiva a Fotones* para el GBM (en inglés, *Phonton Isoeffective Dose Model*), alimentado por datos radiobiológicos generados específicamente para este tumor. Las curvas de sobrevida celular se obtuvieron mediante ensayos clonogénicos en la línea U-87 (GBM humano) irradiada con fotones, neutrones y neutrones en presencia de boro (BNCT). Las curvas se ajustaron mediante un modelo lineal-cuadrático modificado, que incluye la reparación de daño subletal y sinergismo entre radiaciones. Los parámetros radiobiológicos resultantes se utilizaron para construir el modelo, que finalmente se aplicó a un caso clínico de GBM tratado con BNCT en Taiwán. Los resultados muestran que los valores de la dosis equivalente a fotones difieren hasta un 32% según la radiación de referencia elegida y son, en promedio, un 17%

inferiores a las estimaciones obtenidas con el modelo utilizado actualmente en los ensayos clínicos.

La segunda parte de este trabajo se centra en la escala subcelular, midiendo y analizando la microdistribución de boro-10 en las células U-87. Por primera vez, mediante autorradiografía neutrónica, se obtuvo la distribución de boro en células GBM, demostrando una acumulación preferencial en el núcleo. Estos datos se utilizaron para desarrollar y alimentar el modelo *Microdosimétrico de Dosis Isoefectiva a Fotones*. Dicho modelo tiene en cuenta la naturaleza estocástica de la deposición de energía asociada a la distribución intracelular del boro, mediante un factor de corrección de la componente de dosis boro. La relación experimental de concentración de boro entre núcleo y citoplasma se describió mediante una variable aleatoria lognormal, en concordancia con otros procesos biológicos de captación.

El factor de corrección se aplicó a la dosimetría de los datos obtenidos en la línea celular U-87 para obtener los parámetros radiobiológicos corregidos. De esta forma, los efectos a escala subcelular se integraron en el formalismo de la dosis isoefectiva a fotones y se aplicaron a un caso clínico de GBM. Estas correcciones dieron lugar a una reducción del 47% de la eficacia biológica del compuesto (CBE), parámetro relacionado con la eficacia de BNCT en comparación con la irradiación con fotones para un efecto dado. Esto indica que no considerar la distribución subcelular conduce a la sobreestimación significativa de la dosis de boro. Cuando se aplica al caso clínico, la dosis total difiere sólo un 4% con respecto a la dosimetría convencional. Sin embargo, los análisis de perturbación han mostrado que, en presencia de una mayor heterogeneidad intracelular, plausible *in vivo*, las desviaciones alcanzan una diferencia del 22%. Como conclusión de esta parte del trabajo, los efectos biológicos deben correlacionarse con una magnitud dosimétrica que tenga en cuenta la microdistribución del boro, lo que pone de relieve la complejidad intrínseca de la dosimetría en BNCT.

En la parte final de esta tesis se desarrolló un modelo preliminar de sobrevida libre de progresión a un año (en inglés, 1-year Progression Free Survival o 1y-PFS), parámetro utilizado en la práctica clínica para evaluar la eficacia del tratamiento de GBM. Se adaptó un modelo desarrollado para la radioterapia con fotones en régimen fraccionado al escenario BNCT en una sola fracción. Los modelos de dosis propuestos, junto con el modelo 1y-PFS, se aplicaron a dos casos clínicos de pacientes con GBM tratados con BNCT en China. El modelo 1y-PFS demostró ser una herramienta adecuada para evaluar la relevancia clínica de los diferentes modelos dosimétricos propuestos.

En síntesis, esta tesis presenta por primera vez el conjunto de parámetros radiobiológicos para el modelo de dosis isoefectiva a fotones en BNCT del GBM, introduciendo además una extensión microdosimétrica del modelo basada en distribuciones de boro obtenidas experimentalmente y mostrando cómo la aplicación de estas herramientas en la planificación del tratamiento permite predecir el resultado clínico. Los desarrollos presentados mejoran la precisión y la personalización de la planificación de BNCT, con la aspiración de contribuir al diseño de futuros

protocolos clínicos.

CHAPTER 1

INTRODUCTION

Boron Neutron Capture Therapy (BNCT) is a highly selective type of radiotherapy based on the neutron capture reaction: $^{10}B(n,\alpha)^{7}Li$. Boron is delivered to patients through compounds engineered to achieve higher concentrations within the tumor while minimizing accumulation in surrounding healthy tissue [1]. The formulations approved for Phase I/II clinical trials are sodium borocaptate (BSH), 4-boronophenylalanine (BPA) and decahydrodecaborate (GB-10) [2].

The treatment is based on the high cross section (around 3840 barn) of neutron capture in ^{10}B at thermal energies ($E_n < 0.5$ eV). The reaction yields two high LET charged particles: an α particle and a ^{7}Li nucleus, which in 93.7% of cases is in an excited state and decays by emitting a 478 keV photon. In the remaining 6.3% of cases, the ^{7}Li nucleus is produced directly in its ground state, and no prompt gamma emission occurs. The products of the neutron capture reaction are highly ionizing particles, which release all their energy in a region comparable with the cell dimension, thus depositing dose inside the cell only. For this reason, BNCT effectiveness depends on the ability to selectively convey a higher quantity of boron in tumor cells than in healthy tissues.

Glial tumors constitute the most common group of intracranial malignant lesions and among them, Glioblastoma Multiforme (GBM) stands out for its malignancy, rapid progression and resistance to conventional therapeutic protocols, consisting of photon irradiation and chemotherapy after surgery. This tumor is characterized by glial hypercellularity, atypical nuclei (nuclear pleomorphism, multinucleation, coarse nuclear chromatin), visible mitotic activity and prominent vascular proliferation with endothelial hyperplasia, often so intense as to cause vascular obstruction and thus abundant areas of tissue necrosis that in turn act as a hypoxic stimulus inducing angiogenesis [3]. Despite improvements in diagnostic modalities and the use of intensive multimodal therapies including also surgery, overall survival time remains less than one year [4].

BNCT is particularly interesting for the treatment of infiltrating brain tumors: being a biologically cell-directed radiotherapy, its application exerts deleterious

effects on tumor cells while preserving the surrounding healthy tissue, improving local tumor control and patient survival. Pre-clinical studies are ongoing in different research group to optimize the effectiveness of this modality by studying the relation between absorbed radiation dose and observed effects.

The complexity of BNCT arises from its mixed radiation field, resulting in a total absorbed dose composed by four components, each causing different effects on biological tissues. It is thus necessary to translate the absorbed dose into photon equivalent units to compare the dosimetric results with conventional radiotherapy, enabling the prediction of clinical outcomes. Since modern clinical trials began, BNCT dose has been calculated using fixed factors (Relative Biological Effectiveness - RBE/ Compound Biological Effectiveness - CBE) to weight the different components. The dose calculated in this way was called *biologically weighted dose*.

In recent years, it has been shown that this approach leads to artificially high dose values in tumors and the impossibility of interpreting clinical results in light of photon radiotherapy. Indeed, when analyzed retrospectively, tumors that received a high biologically weighted dose in a single fraction were not controlled as it would be expected based on the experience in conventional photon therapy. In Argentina, a different approach, based on the formalism called *Photon Isoeffective Dose* was proposed to calculate the BNCT photon-equivalent dose in a more reliable way. The model has demonstrated its ability to explain both tumor and normal tissue responses as a function of the dose. This approach has been tested in retrospective analyses of clinical cases treated at several centers.

To be used in specific clinical applications, the model needs to be fed with radiobiological data obtained from *in vivo* or *in vitro* BNCT experiments, in tumor and normal tissues. Pre-clinical studies are thus needed to produce the parameters of the model for its applications in different types of cancer.

This thesis adopts the Photon Isoeffective Dose Model, employs it to calculate dose in GBM with proper biological data and proposes a refinement of the formalism to include knowledge on boron distribution at the subcellular level.

The dosimetry of GBM patients has always been calculated using the radiobiological parameters of Gliosarcoma, GSM. Gliosarcoma contains a portion that matches the histological criteria for GBM and a mesenchymal component that can present a variety of morphologies originating from fibroblastic, cartilage, bone, smooth muscle, striated muscle, or adipose cells. GSM is considered a close sibling of GBM. Studies show that this tumor has a unique and distinct clinicopathological entity compared to GBM, and therefore, a precise classification is necessary for appropriate treatment planning [5].

This work defines a suitable model for calculating Photon Isoeffective Dose for GBM, producing ad-hoc *in vitro* radiobiological data. To this end, human Glioblastoma cell cultures (U-87 cell line) were irradiated in Pavia, evaluating the radiobiological parameters for an accurate Photon Isoeffective Dose Model for this tumor, it will be called *Macro Isoeffective Model*.

Once the GBM Macro Isoeffective Model was obtained, an improvement has been proposed, which integrates the stochastic aspects of energy deposition related to

the non-uniformity of boron concentration at the subcellular level, considering the nucleus-cytoplasm boron ratio as a stochastic variable, hereafter referred to *Micro Isoeffective Model*. Detailed information on boron concentration distribution has been obtained at the subcellular level using the human GBM U-87 cell line via the neutron autoradiography technique combined with UV-C sensitization. The impact of this change in the theoretical model and its implementation with boron experimental measurements has been evaluated in real clinical cases, by dosimetric calculations performed with and without the proposed changes.

For GBM, it is not adequate to use Tumor Control Probability (TCP) as a measure of treatment efficacy. In fact, the peculiar morphological characteristics of this tumor, such as diffuse infiltration into the brain tissue and the absence of sharp margins, make it difficult to precisely define and quantify the *local control* of the disease. Moreover, clinical factors such as the presence of edema or necrosis can confuse the interpretation of radiological images, further hampering a reliable assessment of TCP. For these reasons, alternative endpoints are often preferred, such as Overall Survival (OS) or, more commonly, a surrogate endpoint for OS: Progression-Free Survival at one year (1y-PFS), which represents the time elapsed since treatment without evidence of disease progression. The last part of this work is dedicated to the study of a Progression-Free Survival model for GBM, constructed from clinical data on patients treated with conventional photon radiotherapy.

The thesis is organized into four main parts, followed by a final Chapter that presents the conclusions and outlines future perspectives.

The first Part (I) is an introduction, dedicated to basics concepts that are necessary to frame the work described in the following part, also providing some theoretical fundamentals. The background starts with an overview of Glioblastoma Multiforme I.1 and Boron Neutron Capture Therapy I.2. Subsequently, the basic concepts of dosimetry in BNCT are presented, with a focus on the principles of microdosimetry I.3 and I.4.

In the second Part (II), the Macro Isoeffective Model for GBM is developed, starting with radiobiological experiments and ending with its application in a clinical case. The experimental procedures are detailed in Chapter II.1, while Chapter II.2 presents the development of the Isoeffective Dose Model for GBM and Chapter II.3 the application of the model to a GBM clinical case.

The third Part (III) is devoted to the Micro Isoeffective Model. Chapter III.1 introduces the mathematical framework for calculating the expected value of BNCT absorbed dose, incorporating microdosimetric aspects. In Chapter III.2, neutron autoradiography experiments are employed to determine boron concentration in the nucleus and cytoplasm, ultimately leading to Chapter III.4, where the model is applied to a representative clinical case.

In Part IV, 1 year Progression-Free Survival is analyzed as a figure of merit for evaluating treatment efficacy. In particular, it is described in Chapter IV.1. In Chapter IV.2, a retrospective analysis of two GBM patients treated with BNCT in China is presented, applying the dose models developed and discussed throughout

this thesis.
The final Chapter comprises the conclusions and the future perspectives of this work.
Overall, this thesis provides a deeper understanding of BNCT dosimetry for Glioblastoma Multiforme, opening the way for more accurate, effective, and personalised therapeutic strategies in the fight against this untreatable disease. By integrating radiobiological data with information on the intracellular distribution of boron-10 into subcellular-scale modeling and microdosimetric analyses, this work achieves a substantial advancement in the dose–effect description in BNCT.

Part I

Theoretical and Clinical Background

CHAPTER I.1

BRAIN TUMORS

Cancer is one of the leading causes of mortality worldwide and comprises a heterogeneous group of diseases characterized by uncontrolled cell proliferation.
Neoplasms can be classified according to the tissue from which they originate and their histological and molecular characteristics. Although significant advances have been made in the diagnosis and treatment of many forms of cancer, some neoplasms remain particularly difficult to tackle due to their biological complexity and resistance to conventional therapies.
Among these, brain tumors stand out as some of the most aggressive and difficult to treat neoplasms. Unlike many extracranial tumors, brain tumors are often characterized by rapid progression, high invasiveness, and a limited response to conventional therapies.

I.1.1 Glia tumors

The word *glia* derives from the Greek $\gamma\lambda o\iota\alpha$ (*gloía*), which means "glue": glial cells are those that, together with neurons and axons, form part of the brain nervous system. They provide a structure to support and sustain the actual nerve cells, also known as neurons. Brain tumors called *gliomas* are graded on a scale of one to four.

- Grade one I gliomas usually grow slowly and often behave more benignly.
- Grade two II and three III gliomas can grow more rapidly and often require more aggressive treatment.
- Grade four IV gliomas are the most aggressive type and are also known as Glioblastoma or Glioblastoma Multiforme: GBM.

Most gliomas require a biopsy to determine their grade and to predict their future behavior and growth rate.

Low-grade gliomas generally occur in younger patients. They often present with seizures and less commonly with neurological deficits such as paralysis or speech problems. Grade one gliomas can be treated with surgery alone and then monitored for regrowth without further treatment. However, grade two and three gliomas almost always require more aggressive treatment, which may include a combination of surgery, radiotherapy and chemotherapy. These gliomas can recur and, over time, progress to become GBM. Generally, the treatment of GBM needs to be more aggressive because it grows more rapidly, as further explained following.

I.1.2 Glioblastoma Multiforme

Glioblastoma multiforme is the most aggressive form of glioma. Although it occurs almost exclusively in the brain, it can also appear in the brainstem, cerebellum, and spinal cord.
GBM is classified as a **grade IV** central nervous system (CNS) tumor by the World Health Organization (WHO) [6, 7]. It is clinically aggressive and fast-growing, invading nearby brain tissue but rarely spreading to distant organs.
Glioblastomas can be classified as primary, or *de novo*, i.e. as aggressive and highly invasive neoplasms not arising from other diseases. They are usually not accompanied by clinical, radiological or histopathological evidence of previous disease or previous lesions (low-grade gliomas). Less commonly, GBM may present as secondary, i.e. resulting from the progression of low-grade astrocytomas.
In adults, GBM most commonly arises in the cerebral hemispheres, particularly in the frontal and temporal lobes. Since most patients die within a year and virtually none achieve long-term survival, these tumors have attracted significant attention. However, over the past half-century, they have resisted increasingly sophisticated, targeted, and complex therapeutic strategies [8].
GBM presents unique therapeutic challenges due to:

- tumor localization in the brain;
- intrinsic resistance to conventional therapy;
- limited capacity of the brain to repair itself;
- migration of malignant cells into adjacent brain tissue;
- interrupted blood supply to the tumor area, which inhibits effective drug delivery;
- loss of capillaries in the tumor area, resulting in accumulation of fluid around the tumor (peritumoral edema) and intracranial hypertension;
- tumor-induced epileptic seizures;
- additional neurotoxicity due to the treatments directed at gliomas.

GBM is the most common malignant tumor of the brain and other central nervous system structures, accounting for 47.7% of all such cases, with an incidence of 3.19 per 100,000 population. The median age of diagnosis is 58 years and it is more common in men than in women. Survival is scarce, with approximately 40% survival in the first year after diagnosis, 26-33% in the second year and 4-5% in 5-year [9, 10].
The GBM treatment remains a serious challenge due to its inherent biological characteristics, which significantly limit therapeutic efficacy. Firstly, its highly infiltrating nature makes complete surgical resection almost impossible. Furthermore, the blood-brain barrier (BBB) represents a significant obstacle to systemic chemotherapy. The BBB is a specialized functional structure interposed between the bloodstream and the neural parenchyma, composed of tight junctions and transport proteins, which selectively regulate the passage of molecules, protecting the nervous system from toxins and systemic exposure [11, 12].
Not to mention that GMB is often diagnosed at an advanced stage and requires complex, multidisciplinary diagnostic and therapeutic management.
The earliest descriptions of GBM date back to the 19th century, when it was recognized as a distinct pathological entity with a biological behavior similar to that of extracranial malignancies [13, 14].
At the molecular level, GBM is characterized by a heterogeneous genetic and epigenetic panorama, with different mutational subgroups (MSGs) affecting patient survival and response to treatment [14, 15, 16]. However, for many of these mutations, the prognostic or therapeutic relevance remains unclear.
Historically, the term "Multiforme" was introduced to describe the morphological heterogeneity observed within GBM tumor samples. More recently, this concept has been expanded to reflect the genetic diversity of this neoplasm [17, 18].
Clinically, GBM leads to progressive neurocognitive decline [19, 20], loss of functional independence, and substantially reduced quality of life [21, 22].

I.1.3 Standard of treatment

GBM treatment is very challenging due to the risk of damage to surrounding healthy tissue, drug resistance and the presence of the BBB.
Standard treatment consists of surgical resection followed by radiotherapy (RT), which significantly prolongs survival [23]. Chemotherapy in addition to RT is used as concomitant or adjuvant treatment. Although more long-term survival has been reported after the two combined therapies, [24, 25] their success is limited in patients who develop resistance to conventional chemotherapy and radiotherapy [26]. Another strategy is immunotherapy.

I.1.3.1 Radiotherapy

Generally, radiotherapy is one of the treatment options considered for GBM patients, although there are, also in this case, non-negligible limitations. Tumor re-

sponse to radiotherapy depends on the tumor size: larger tumors are less sensitive to radiation than smaller ones.
There are various photon therapy techniques suitable to this end, in particular:

- **Conventional radiotherapy**: involves the fractionated administration of a total dose between 40 and 60 Gy over six weeks, with a dose per fraction of 1.8-2 Gy. Fractionation allows healthy tissue to activate repair mechanisms between one session and the next, thus reducing treatment toxicity. In some cases, hypo-fractionated schedules are used, for example, 40 Gy administered in 15 fractions over three weeks, reducing the overall treatment duration without compromising efficacy. There are two main delivery methods for the radiation dose to the tumor volume: 1) Conventional three-dimensional radiotherapy (3D-CRT), which uses three-dimensional images (CT and/or MRI) to tailor the radiation beams according to the shape of the tumor, allowing more targeted irradiation than conventional two-dimensional techniques. 2) Intensity-modulated radiotherapy (IMRT) which allow greater conformality through several beams modulated with different intensities and angles. This technique enables higher doses to be delivered to the target volume, reducing the exposure of surrounding healthy structures.

- **Brachytherapy**: involves implanting one or more radioactive emitters directly inside the tumor or in the tumor bed during surgery. The most commonly used isotopes are iodine-125 and iridium-192. However, this technique is associated with several side effects, including tissue necrosis, vascular damage, and risk of radiation exposure for persons in close contact with the patient [27, 28].

- **Stereotactic radiosurgery (SRS)**: uses multiple radiation sources that converge on the target with a steep dose gradient at the edges of the treated volume [29]. The technique allows very high precision but is generally limited to small tumors, as the toxicity risk increases with the size of the irradiated volume. The main technologies available for stereotactic radiosurgery include:

  - **Gamma Knife**: a technique that minimizes the exposure of healthy brain tissue and is backed by long clinical experience. Thanks to the high precision of the collimator, in most cases treatment is carried out in a single session in an outpatient setting, with no need for hospitalization; in special situations, however, up to five sessions may be necessary. The treatment protocol first involves the application of a stereotactic helmet or thermoplastic mask to immobilize the patient's head and precisely define the target region. During this phase, the patient receives mild sedation. Next, images (CT and/or MRI) are acquired on which the target to be irradiated is delineated. The treat-

ment duration varies from about 20 minutes to 4 hours, depending on the extent and nature of the pathology.

- **CyberKnife**: system based on a robotic arm on which a linear accelerator is mounted, capable of moving with 6 degrees of freedom and around 1,200 different positions. This technique allows to irradiate the target from multiple directions. During treatment, the patient's movements are monitored by an optical tracking system; any displacement of the tumor is automatically compensated by the robot, guaranteeing precision even on moving lesions.

- **Fractionated stereotactic radiotherapy (FSRT)** is similar to SRS, but the total dose is divided into fractions (usually 3-5) and administered over successive days. This approach allows a better sparing of healthy tissue and enables the treatment of slightly larger lesions or those located near critical structures.

I.1.3.2 Chemotherapy

Temozolomide (TMZ) is the most widely used chemotherapeutic drug for the treatment of GBM [30]. It is an acid pH stable alkylating cytotoxic agent that is generally used in the early stages of lesion development, possibly combined with radiotherapy to maximize the effect. This type of therapy has non-negligible side effects such as neuronal damage, nausea, vomiting, hair loss, infertility and insomnia.
The main causes of chemoresistance can be found in the presence of tumor stem cells derived from embryonic stem cells and in the reduced partial pressure of oxygen that leads to the triggering of an autophagy process in the area around the tumor.

I.1.3.3 Immunotherapy

There are several types of immunotherapy proposed for the treatment of GBM such as the use of immune checkpoint inhibitors, viral therapy and dendritic cell immunotherapy. However, difficulties remain in patient selection, monitoring of results and evaluation of possible side effects. Although remarkable preclinical results have been obtained, the transition to clinical trials is complex due to tumor cell heterogeneity, difficulties in overcoming the blood-brain barrier, poorly standardized clinical endpoints and the difficulty in determining a maximum tolerable dose [23].

It is well established that the high level of heterogeneity between tumors and within the neoplasm itself is a cause of the poor success of trials of any type. Although high-grade gliomas are uncommon, these tumors represent a disproportionate loss of life years due to their poor prognosis.

Standard local treatment includes external beam radiotherapy after a maximal surgical procedure. Attempts to improve outcome by increasing the local radiation dose have generally been unsuccessful due to necrosis in the surrounding brain, which becomes dose limiting before achieving a significant local tumor control. A more effective approach would be to develop agents that selectively sensitize these tumor cells to radiation. In the past, nitroimidazoles have been used in an attempt to sensitize the known fraction of hypoxic cells, and 5-bromodeoxyuridine analogues have been added to standard-dose radiotherapy to sensitize rapidly dividing tumor cells. Neither approach produced clinically evident benefits [31, 32].

Given the resistance to conventional radiotherapy and the infiltrating spread of GBM, it is crucial to explore alternative strategies with a better tumor selectivity and lethality profile.

In this context, Boron Neutron Capture Therapy (BNCT) has emerged as a promising therapeutic approach, being a biologically cell-directed type of radiotherapy. As explained in Chapter I.2, BNCT is the only form of selective radiotherapy, due to the targeting of tumor cells by borated drugs. BNCT has been explored in GBM patients, demonstrating encouraging outcomes, especially in recent years [33, 34].

CHAPTER I.2

BORON NEUTRON CAPTURE THERAPY

Boron Neutron Capture Therapy (BNCT) is an experimental form of hadrontherapy. It is a binary technique that involves:

1. the intravenous administration of a boron compound to the patient,
2. the subsequent irradiation of the target anatomical region with a thermal or epithermal neutron beam.

The isotope boron-10, $^{10}\mathrm{B}$, is a stable, non-radioactive element that constitutes approximately 19.8% of natural boron. Upon capturing a neutron, $^{10}\mathrm{B}$ forms an excited $^{11}\mathrm{B}^{*}$ nucleus, which has an extremely short half-life of approximately ($\tau \approx 10^{12}\ s$). This nucleus then splits into an alpha particle (α) and a residual $^{7}\mathrm{Li}$. In 93.7% of cases, the $^{7}\mathrm{Li}$ emerges in an excited state and subsequently decays to its ground state via the emission of a 0.477 MeV photon. In the remaining 6.3% of cases, the $^{7}\mathrm{Li}$ nucleus is produced directly in its ground state, and no prompt gamma emission occurs (see Figure I.2.1).
The BNCT nuclear reaction branches are [35]

$$\mathrm{n} + {}^{10}\mathrm{B} \longrightarrow {}^{11}\mathrm{B}^{*} \longrightarrow \alpha(1.78\ \mathrm{MeV}) + {}^{7}\mathrm{Li}(1.01\ \mathrm{MeV}) \quad [BR = 93.7\%] \tag{I.2.1}$$

$$\mathrm{n} + {}^{10}\mathrm{B} \longrightarrow {}^{11}\mathrm{B}^{*} \longrightarrow \alpha(1.47\ \mathrm{MeV}) + {}^{7}\mathrm{Li}^{*}(0.84\ \mathrm{MeV}) \tag{I.2.2}$$

$$\longrightarrow {}^{7}\mathrm{Li} + \gamma(0.477\ \mathrm{MeV}) \quad [BR = 6.3\%] \tag{I.2.3}$$

The reaction occurs with a cross-section $\sigma = 3840$ barn for thermal neutrons of $E_n = 0.025$ eV. The capture reaction products are emitted back-to-back.

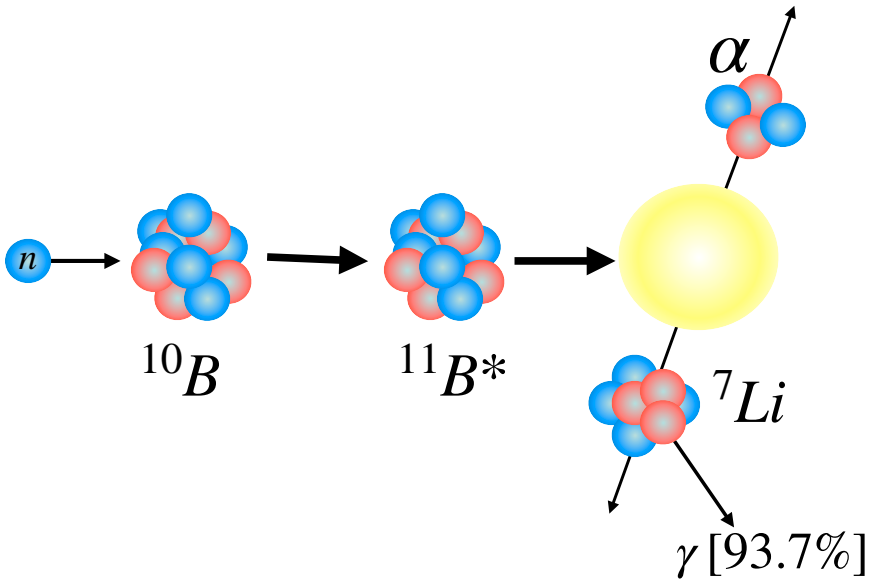

Figure I.2.1: *Schematic representation of the neutron capture reaction in* $^{10}\mathrm{B}$.

I.2.1 Dosimetry of a mixed radiation field

To provide a complete framework that will be useful for the description of the work presented in the following parts of the thesis, the concepts of dose and KERMA are introduced in this section. Following, the dose components of the BNCT radiation field will be listed and described.
In an infinitesimal volume V, of mass m, *absorbed dose* is defined to be the limit of the imparted energy $\bar{\epsilon}$ per unit mass:

$$D = \lim_{m \to 0} \frac{\bar{\epsilon}}{m} = \frac{1}{\rho} \frac{\bar{\epsilon}}{V}. \tag{I.2.4}$$

The unit of measurement of the absorbed dose is the *Gray* (Gy), which in the International System of Units corresponds to

$$1\,\mathrm{Gy} = 1\,\frac{\mathrm{J}}{\mathrm{kg}}.$$

Dose is the physical quantity that describes the distribution of energy imparted to matter per unit mass in terms of its expected value.
The energy imparted ϵ in a volume is defined as:

$$\epsilon = R_{\mathrm{IN}} - R_{\mathrm{OUT}} + \sum Q, \tag{I.2.5}$$

where:

- R_{IN} is the radiant energy (i.e., the sum of the kinetic energy of the ionising particles) entering the volume of interest;

- R_{OUT} is the radiant energy leaving the volume of interest;
- $\sum Q$ is the sum of all energy changes of the rest mass of the nuclei and particles occurring inside the volume.

By definition, *KERMA*, K, (*Kinetic Energy Released per unit MAss*) represents the initial kinetic energy transferred from the *uncharged* particles (photons, neutrons, etc.) to the *secondary charges* particles set in motion, per unit mass [36]. It can be decomposed into two main contributions:

$$K = K_{\mathrm{col}} + K_{\mathrm{rad}}, \tag{I.2.6}$$

where:

- K_{col} is the *collisional* component, i.e., the energy that secondaries dissipate through ionization and excitation processes, which may actually contribute to the absorbed dose;
- K_{rad} is the *radiative* component, which corresponds to the energy lost in the form of electromagnetic radiation (e.g., bremsstrahlung), which may escape from the volume and thus not contribute locally to the dose.

In the case where the condition of *Charged Particle Equilibrium (CPE)* is satisfied, that is, when the energy carried by the charged particles that *enter* into a volume is equal to that which *exits*, and radiative losses are negligible, the absorbed dose D coincides with the collisional part of the KERMA:

$$D = K_{\mathrm{col}} \approx K. \tag{I.2.7}$$

Thus, under these conditions, a direct correspondence is established between the physical quantity *KERMA* and the clinically relevant quantity, namely the *absorbed dose* .

The calculation of absorbed dose in BNCT is complex because neutrons not only interact with $^{10}\mathrm{B}$, but also with other nuclei in biological tissue. This results in a mixed radiation field, where each component has different characteristics and effectiveness in causing biological damage.
The radiation field consists in a combination of components with different Linear Energy Transfer, LET [1]. The simultaneous presence of radiation of different qualities makes dosimetry in BNCT significantly more complex than in conventional photon radiotherapy. In fact, the field of radiation produces four main dose components [37] (see Figure I.2.2):

- **Gamma dose**, D_γ.
  It is due to three contributions: the first is due to the neutron capture reaction $^{1}\mathrm{H}(n,\gamma)^{2}\mathrm{H}$, which emits a photon, γ, of 2.2 MeV. Once emitted, these

[1] The average amount of energy that a charged particle transfers to the material traversed per unit distance. The units of LET are [keV/μm].

photons can traverse significant distances through biological tissues, depositing energy far from their origin. As a result, the radiobiological effects may extend beyond the targeted area, potentially affecting healthy tissue. This dose is not negligible: hydrogen has a cross-section for radiative capture much smaller than boron ($\sigma_H = 0.33$ barn), but its abundance is approximately 10–15% of total body weight. The second contribution originates from the **structural photons** inherent in the neutron beam. This background radiation should be minimized by using appropriate shielding materials in the beam delivery system. The third component is the 0.477 MeV γ-ray emitted by the de-excitation of $^{7}\mathrm{Li}^{*}$.

- **Dose from thermal neutrons**, $\boldsymbol{D_{n_{th}}}$.
  This contribution is due to the neutron capture reaction: $^{14}\mathrm{N}(n,p)^{14}\mathrm{C}$, producing a proton with an energy of approximately 0.58 MeV, with an average LET in soft tissue of about 10-50 keVμm^{-1}. Being a intermediate highly ionizing particle, it is capable of inducing significant biological damage, including lethal double-strand breaks in DNA. The biological damage caused by the proton occurs only a few μm away from the proton emission due to the short range of the proton in tissue ($\sim 10 - 11$ μm). Although the effective cross-section of nitrogen ($\sigma = 1.86$ barn) is much lower than that of boron, nitrogen is present in biological tissues at a relatively high concentration, accounting for approximately 3% of the total body weight. Therefore, the contribution of nitrogen capture reactions to the total dose is not negligible.

- **Proton recoil dose**, $\boldsymbol{D_{n_f}}$.
  Its main origin is in the elastic collision between the epithermal/fast neutrons of the beam with the $^{1}\mathrm{H}$ nuclei in tissue: $^{1}\mathrm{H}(n,n')^{1}\mathrm{H}$. During the process, the neutron decreases its energy, losing on average half of its energy in each collision. The energy deposited by the recoil proton contributes to the overall dose delivered to the tissue. Since hydrogen is abundantly present in biological tissues (about 10% by weight), this component represents a significant part of the total BNCT dose .

- **Boron dose**, $\boldsymbol{D_B}$.
  It originates from the neutron capture reaction $^{10}\mathrm{B}(n,\alpha)^{7}\mathrm{Li}$ (see Eqs. I.2.1 and I.2.3) and it is the dose component that is required to be maximized in tumor since it is the therapeutic dose component. The boron neutron capture cross-section at thermal neutron energies is the highest among the other interactions of neutrons with the other elements in biological tissue ($\sigma = 3840$ barn at 0.025 eV). The α particle and $^{7}\mathrm{Li}$ nuclei possess high LET (150 keV/μm and 200 keV/μm respectively). This means that their ionization pattern along their trajectory is extremely dense, and that the probability of inducing complex biological damage is high. Therefore, they have a strong capability to produce clustered DNA damage, including double-strand breaks (DSB), within a range of only a few micrometers, comparable to the dimensions of a single cell. To maximize this component in tumor

treatment, it is essential to ensure a selective accumulation of ^{10}B atoms in the tumor compared to healthy tissue, combined with an optimized tailoring of the irradiation spectrum to minimize the dose delivered to surrounding healthy tissues.

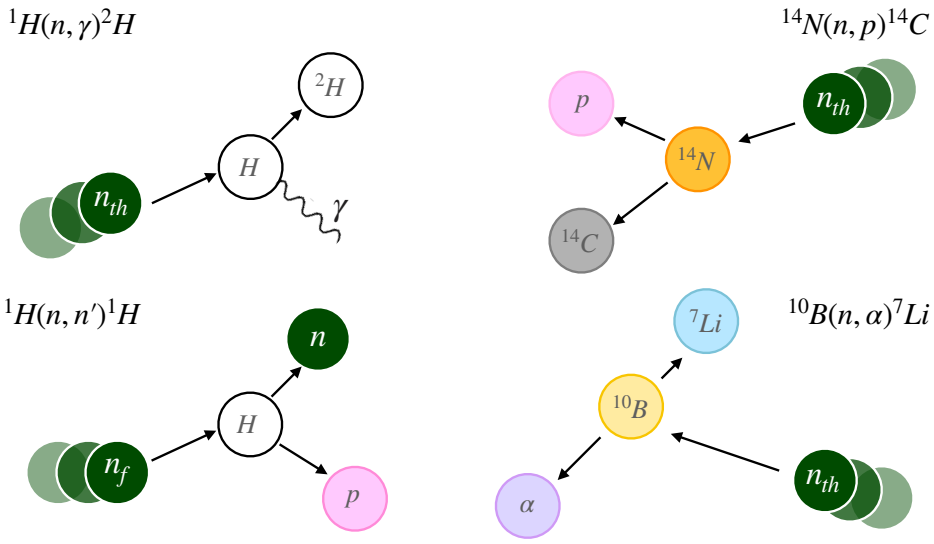

Figure I.2.2: *The four absorbed dose components that contribute to the BNCT dose and the main reactions that cause them.*

The total BNCT absorbed dose is the sum of these four components (Eq. I.2.8).

$$D_{BNCT} = D_B + D_{n_{th}} + D_{n_f} + D_\gamma. \tag{I.2.8}$$

Boron Neutron Capture Therapy differs from conventional radiotherapy and charged-particles hadrontherapies due to its unique ability to selectively target cancer by preferentially accumulate boron within the tumor region. In charged-particle therapy, the beam energy is tuned to maximize the tumor absorbed dose at a specific depth by adjusting the position of the *Bragg peak*[2]. For this reason, a highly focused beam is required to precisely target and destroy cancer cells. In contrast, the BNCT neutron beam energy must be selected to induce the specific nuclear reaction of interest, thus it will be thermal or hyper-thermal for shallow tumors (such as nodular melanoma [38]) and epithermal for deep-seated tumor. The beam aperture is usually as wide as possible to cover the tumor volume and surrounding areas possibly containing isolated cells, cause of metastasis or recurrence.

[2]The energy loss of charged particles in matter is described by the *Bragg Curve*. When passing through a material, charged particles ionize atoms and deposit a dose along their path. In particular, the cross-sectional area increases as the energy of the particles decreases, and consequently, the energy lost is inversely proportional to the square of their velocity. For this reason, the *Bragg curve* has a peak just before the particle stops, called the *Bragg peak*.

In BNCT, the treatment time is determined by prescribing a maximum tolerable dose to the surrounding healthy tissue, rather than by prescribing a target dose to the tumor, as is standard in conventional photon or charged-particle radiotherapy. Two aspects motivate this practice: 1) clinical safety reasons: the priority is to avoid excessive toxicity to healthy organs, which also absorb a certain boron concentration. The distribution of boron in normal tissues is usually more uniform than in tumor, thus the calculated dose is a more reliable reference for the treatment. 2) The dose required to ensure a high Tumor Control Probability (TCP) is not yet established for any tumor in the context of BNCT. This is mainly because clinical results obtained with BNCT, when expressed in photon equivalent units, cannot be directly compared with those of conventional photon radiotherapy. The equivalence to photon dose has not yet been formulated in a clinically reliable manner, and the limited number of treated patients does not allow for the construction of robust dose–effect relationships in terms of BNCT dose. Consequently, in current clinical practice, it is preferable to use the tolerance of surrounding healthy tissues as the reference for the treatment time.For this reason, when calculating the irradiation time in BNCT, the tumor dose is not the target; instead, the treatment time is determined based on the maximum dose that can be tolerated by healthy tissue, while ensuring therapeutic efficacy due to the selective accumulation of boron in tumor cells.
BNCT is typically administered in one or, at most, two sessions due to its selective nature and high biological efficacy. In contrast, both conventional radiotherapy with photons and hadrontherapy with charged particles generally require fractionated regimes, with multiple sessions spread over several weeks, to allow healthy tissue to recover between irradiation sessions.
BNCT is currently being investigated worldwide as a promising alternative for the highly resistant tumors, including rare and orphan diseases, due to its unique ability to selectively target cancer cells while sparing healthy tissues. This characteristic makes BNCT particularly relevant for tumors with complex growth patterns, such as infiltrating and diffuse lesions. The former are characterized by the ability to invade surrounding tissues, crossing their anatomical boundaries and spreading locally, with possible compressive effects on adjacent organs and potential metastatic dissemination. This is a deep invasion of healthy tissue, which can make complete surgical removal complex. Diffuse lesions, on the other hand, extend broadly and are less defined, without forming a clear margin or well-defined mass, with tumor cells spreading among healthy ones.

I.2.2 Boron compounds

Borated compounds are crucial for BNCT success: they act as boron-10 carriers within tumor cells. An ideal borated compound should target exclusively the tumor cells. In reality, this is not the case, at least with formulations currently used in humans, which carry a certain boron quantity also in normal cells. A suitable BNCT carrier should possess these key characteristics:

1. it must carry enough boron nuclei into the tumor to allow sufficient neutron captures to inactivate tumor cells, i.e., approximately $\geq \frac{20\ \mu\text{g}}{\text{g of tumor}}$ (= 20 ppm);
2. good solubility and stability over time to ensure effective distribution and an adequate half-life;
3. should always accumulate much more in tumor cells than in healthy ones with a minimum Tumor-to-Normal ratio of about 2.5, not to excessively limit the irradiation of the tumor;
4. low systemic toxicity: it must be well tolerated by the body.

BSH has been used in brain neoplasms and can reach brain tumor cells. Although the mechanism by which this compound can cross the blood-brain barrier is still unclear [39], it has shown positive results for patients with GBM in the Nineties European trial and in Japan [40, 41]. Boron accumulation via BSH is often insufficient, which is why Boronophenylalanine (BPA) is the one used BNCT drug due to its selectivity of absorption. Borofalan(10B), a variation of BPA has been recently approved in Japan, where BNCT is now included for coverage by the national health insurance system for unresectable locally advanced or locally recurrent head and neck cancer [42]. However, some critical issues persist: BPA accumulation does not always reach optimal levels for therapy application, making some patients untreatable. Recently, nanostructured carriers: dendrimers, liposomes, and polymeric nanospheres have been developed to improve boron transport into tumor cells [43].
Research continues globally to find more effective and, at the same time, safe compounds suitable for future BNCT applications.

I.2.3 BNCT clinical applications

Boron Neutron Capture Therapy has been progressively applied to several diseases over the years, including GBM, head and neck cancers, lung cancer, and malignant melanoma (MM), see Figure I.2.3.
Clinical trials conducted in the United States, Japan, China, Taiwan, Argentina, and Europe have evaluated the safety and efficacy of this therapy, reporting promising results. More than 2,000 patients have received a BNCT treatment, with no documented episodes of acute uncontrollable radiation injury above grade 3 [44]. These data confirm an encouraging safety profile and support the potential of BNCT as an innovative treatment option.
Japan and the United States are the two countries with the highest number of patients treated with BNCT. Figure I.2.4 provides a global overview of BNCT use, highlighting in red those states that have treated patients. The color scale indicates the number of patients treated, from light red, representing less than 100 patients, to dark red, representing more than 200, as shown in the legend [44].

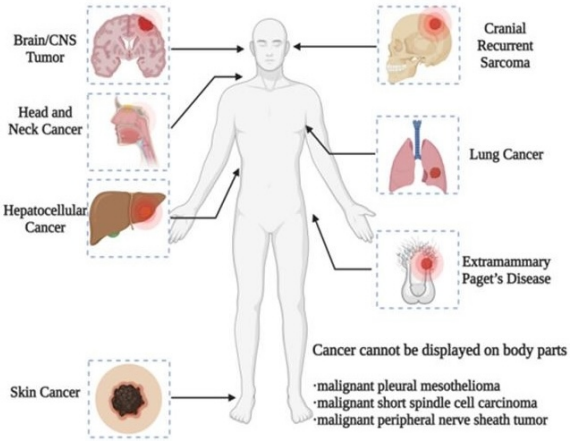

Figure I.2.3: *Body districts that have been involved in BNCT clinical trials for different types of cancer. Image taken from [44].*

However, as of 2020, **Japan** is the only country to have **authorized the clinical use of BNCT** for head and neck tumors, while in other countries, the therapy has so far been limited to clinical trials and clinical studies.

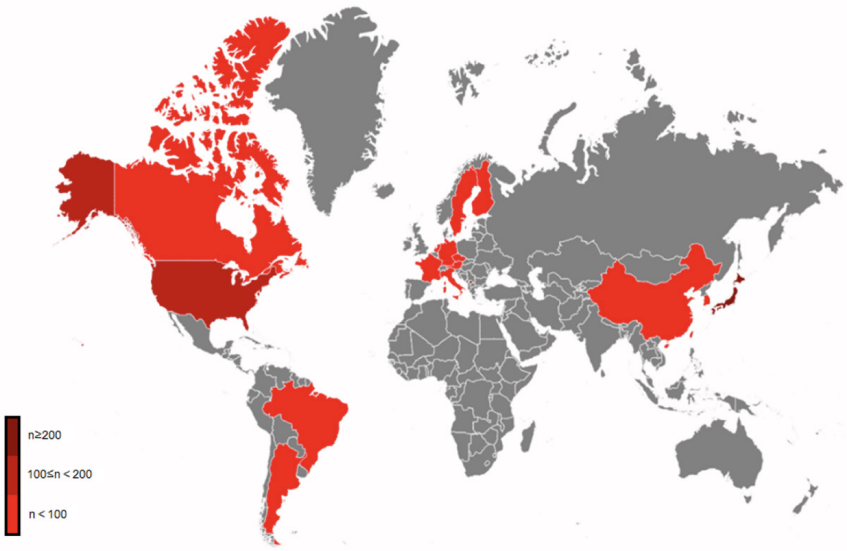

Figure I.2.4: *Boron neutron capture therapy clinical trials. Countries in red are those where BNCT clinical trials have been reported, the color scale is according to the number of reported cases. Image taken from [44].*

The work presented in this thesis is part of the BNCT development scenario, which is advancing in Italy and Argentina.
In Italy, the ANTHEM project, (AdvaNced Technologies for Human-centrEd Medicine) is financed by the Complementary Plan to the National Plan for Recovery and Relislience (PNC-PNRR) in the call for the funding of research initiatives for tech-

nologies and innovative trajectories in the health and care sectors. The project involves 4 Spokes of which the 4th aims at implementing new technologies and methods for the treatment of tumors. ANTHEM has a special focus on the treatment of brain tumors, especially those that are currently orphan, such as glia tumors. The Pilot 4.9 is dedicated to the construction of a BNCT clinical and research centre at the University of Campania "Luigi Vanvitelli". The neutron source will be based on a Radiofrequency Quadrupole accelerator (RFQ): a 5 MeV, 30 mA proton accelerator developed at the Legnaro National Laboratories (INFN), which will hit a Be-Pa-Cu target. The beam will be shaped using a Beam Shaping Assembly (BSA) developed in Pavia, capable of providing a neutron flux of the order of $10^{13}, \mathrm{cm}^{-2}, \mathrm{s}^{-1}$, as required by the guidelines for a short and effective treatment. The technical part of the building will house the neutron production technology and its ancillaries, the irradiation room for patients, an experimental room (Figure I.2.5). The rest of the building will consists of the medical rooms, laboratories and spaces for the staff and the instrumentation.

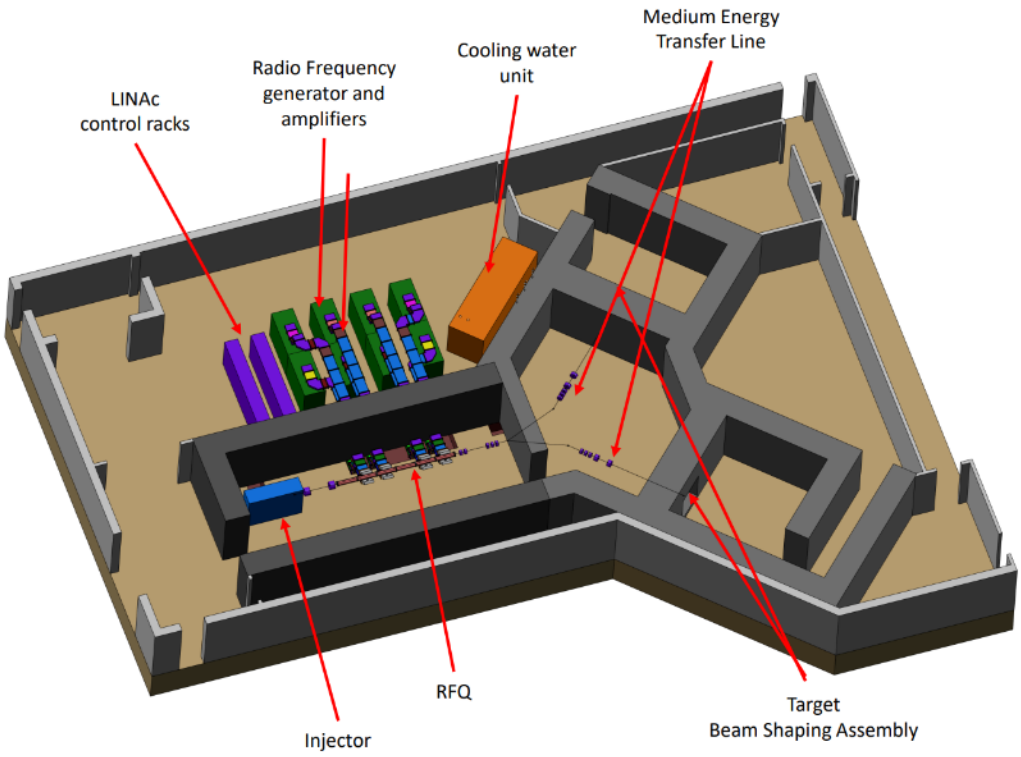

Figure I.2.5: *The structure of the building showing the areas dedicated to the accelerator and its technical ancillaries and the two irradiation rooms.*

In Argentina, a BNCT irradiation facility is already operational at the RA-6 reactor Bariloche, used for research and clinical applications. Several patients affected by nodular melanoma have been treated in the years [45]. At the same time, a new accelerator-based facility is under construction. The machine under development is a Tandem-ElectroStatic- Quadrupole, TESQ with a terminal voltage of up to

1.2 MV, designed to operate in air without the need for pressure vessels or insulating gases. The goal is to generate a proton beam of approximately 2.4 MeV and 30 mA, intended to irradiate a lithium metal target, so as to produce a high-quality therapeutic neutron beam, minimizing contamination from fast neutrons and subsequently modulated by an optimized Beam Shaping Assembly. Feasibility studies have shown that such a system can guarantee treatments comparable to those obtainable with the best reactors currently in operation [46].

I.2.4 BNCT of Glioblastoma Multiforme

Over the years, several clinical trials have evaluated the efficacy of Boron Neutron Capture Therapy in brain neoplasm, particularly in GBM that is refractory to conventional therapies, as anticipated above.
A clinical study was conducted at Brookhaven National Laboratory between 1951 and 1961 using 10B-enriched borax on 28 patients with brain tumors, including GBM and other types of brain carcinoma. According to the results, this method did not provide any advantages over the standard treatment options that were already available [47]. This poor clinical outcome was largely due to the low efficacy of boron targeting, which was insufficient to guarantee a therapeutic advantage.
With the development of BSH, Nakagawa and Hatanaka [48] achieved a remarkable result in studies conducted between 1968 and 1996 on 149 patients with different types of brain tumors. The overall response rate for glioma after BNCT had increased to 64%.
In Germany, starting from 1997, a clinical trial was conducted in the frame of a project funded by the European Commission, in which 29 patients were treated with BSH infusion after irradiation with a reactor neutron beam. The study provided an Median Survival Time (MST) of 10.4-13.2 months [49].
Between May 1999 and December 2001, at Helsinki University Central Hospital in Finland, a cohort of 18 patients diagnosed with supratentorial Glioblastoma underwent surgery without receiving radiotherapy or standard chemotherapy before treatment with BPA-based BNCT. The BPA-fructose complex was administered for 2 hours at doses between 290 and 400 mg/kg before neutron irradiation, which was performed in a single fraction with two treatment fields. The estimated 1-year overall survival (OS) rate was 61% [50]. In 2025 in Finland the clinical BNCT was re-started using a neutron beam generated by a proton accelerator. The first protocol involve patients with head and neck tumors, however brain tumors will likely be comprised in the next future.
At the Faculty Hospital of Charles University in Prague, Czech Republic, between 2000 and 2002, 5 patients with GBM were treated using the compound BSH, for which, however, clinical results are not available [51]. Between 2001 and 2005 at Nykoping Hospital in Nykoping, Sweden, 29 nGBM and 12 rGBM were treated with BPA-BNCT obtaining a mean overall survival of 17.7 months and 8.7 months, respectively [51, 52, 53].
Japan has a long history of clinical BNCT. In 1985, 40 patients with newly diag-

nosed gliomas and 30 with recurrent gliomas (mostly GBM), 5 with non-resectable meningiomas, and 2 with intracranial sarcomas were treated. From March 1985 to December 1992, additional 53 patients were treated. Eighteen patients survived longer than 5 years (20.7%), and nine patients survived longer than 10 years (17%). Among the long-term survivors, only 2 patients eventually died at 17 and 12 years post-treatment. Notably, 6 patients who had no prior history of radiation before BNCT were able to survive and lead a normal life with no evidence of tumor. The other patient were alive at the time of analysis [54]. Clinical trials on BNCT resumed in 1999, with four unregistered and one registered study. Studies conducted between 1998 and 2007 in patients with brain tumors reported an MST varying between 10.8 and 25.7 months, depending on the treatment protocol and radiation dosage [55, 56]. A phase II study conducted by Kawabata et al. in Osaka on 21 patients with malignant glioma combined BNCT (BSH+BPA) with fractionated X-ray irradiation. The median survival time was 15.6 months, longer than the historical controls treated with surgical resection, radiotherapy, and chemotherapy [57]. Between 2002 and 2003, 10 patients with newly diagnosed nGBM were treated at Osaka Medical College in Takatsuki using a combination of BSH and BPA, achieving a mean overall survival (mOS) of 14.5 months [58, 59]. Between 2003-2006, 12 nGBM were treated with an mOS of 23.5 months [59]. 19 patients with recurrent GBM were treated between 2002 and 2013 with a median OS of 10.8 months [56]. Between 2010 and 2013, 32 patients with newly diagnosed GBM were treated with a median OS of 21.1 months [60], and between 2013 and 2018, 10 patients with rGBM had a median OS of 12 months [60].

Japan has been the pioneer Country of BNCT with accelerators. Between February 2016 and June 2018, a total of 27 cases of Malignant Gliomas, including 24 cases of GBM, were treated with a facility based on a proton beam from cyclotron as part of a phase II clinical trial. A 1-year survival rate of 79% and a median overall survival (OS) of 18.9 months was reported. [61].

A multicenter phase II clinical trial (JG002) was conducted in patients with relapsing malignant gliomas, predominantly glioblastoma multiforme. Treatment was performed using the NeuCure™ accelerator system (Sumitomo Heavy Industries) in combination with the boron-based drug Borofalan (SPM-011). A one-year overall survival rate of 79.2% was observed in the 24 enrolled patients, with a median survival of approximately 18.7 months. In contrast, the median progression-free survival was approximately 0.9 months.

Notably, the first clinical BNCT treatment in Japan required the craniotomy to allow direct irradiation of the tumor with a thermal neutron beam. Patients were under general anesthesia during irradiation and the area was covered with a thermoplastic lithium coating to limit neutron exposure of normal tissues [62]. The application of BNCT without resorting to craniotomy has been made possible thanks to several technological and methodological advances, including: the use of epithermal neutron beams, which are characterized by a greater penetration capacity than thermal beams, a better boron accumulation in tumor with higher boron-to-normal tissues concentration ratio, and the more recent introduction of

^{18}F-BPA PET, which allows the distribution and concentration of boron in tissues to be estimated. [58, 59]
At the Taipei Veterans General Hospital (Taiwan), 34 patients, advanced state malignant brain tumors were treated with BNCT. Results showed a 1-year overall survival (OS) rate of 29% and a 1-year recurrence-free survival (RFS) rate of 16%, with a more pronounced therapeutic response in patients with astrocytoma and Glioblastoma [63].
In Xiamen, China, the first BNCT center with an accelerator was completed, with a study approved by the Chinese Register of Clinical Trials. As of January 2023, 15 patients diagnosed with GBM or head and neck cancer have been treated, and three of these patients showed significant tumor reduction (personal information).
Current challenges in BNCT for GBM include

- Optimization of boron transport and accumulation in tumors.
- Dosimetric modeling for accurate comparison with conventional RT.
- The implementation of radiobiological models to predict tumor control.

CHAPTER I.3

BNCT DOSIMETRY

In conventional radiotherapy, treatment is based on photons or electrons, whose interactions with tissue and biological effects are well-known and predictable. The same applies to charged-particle radiotherapy, where charged particles such as protons or carbon ions exhibit the Bragg peak, allowing precise dose deposition within the tumor. In contrast, in BNCT, the patient is exposed to a mixed radiation field, whose different components have distinct biological effects in inactivating or eliminating tumor and healthy cells. As described extensively in section I.2.1, thermal neutrons interact with ^{10}B, generating highly ionizing products capable of causing complex damage, leading to cell inactivation or death. These low-energy neutrons also interact with other elements in biological tissue, producing 2.2 MeV photons through capture in hydrogen, and protons and ^{14}C recoil nuclei through capture in nitrogen. Additionally, it is important to note that a BNCT neutron beam inevitably has a complex spectrum containing unwanted component (such as fast neutrons) as well as gamma rays, coming from the source of neutrons. The elastic interactions of the fast neutrons with hydrogen nuclei (~50 barn) give rise to recoil protons, which also contribute to the total absorbed dose.
The result is a combination of four BNCT dose components:

- **boron dose,** D_B, resulting from the energy deposition of the products of the reaction ^{10}B(n,α)^{7}Li;

- **thermal neutron dose,** $D_{n_{th}}$, resulting from the energy deposition of the products of the capture reaction ^{14}N(n,p)^{14}C;

- **fast neutron dose,** D_{n_f}, resulting from the energy deposition of the products of the elastic collision reaction ^{1}H(n,n')^{1}H;

- **gamma dose,** D_γ, resulting from the energy deposition of electrons generated by (a) photons from the beam (called structural gamma), (b) photons from the capture reaction ^{1}H(n,γ)^{2}H (called induced gamma) and (c)

photons emitted from the neutron capture reaction in boron, resulting from de-excitation of the ^{7}Li nucleus, which occurs in 93.7% of cases.

Each BNCT radiation component produce different effects on cells. High-LET and low-LET radiation have distinct ionization patterns: the former, highly ionizing, deposits energy in dense clusters along its track, leading to complex DNA damage such as double-strand breaks (DSBs), clustered lesions, and DNA-protein crosslinks, which are difficult for the cell to repair. In contrast, low-LET radiation is characterized by sparse ionization events, primarily causing indirect damage through the formation of free radicals generated by the radiolysis of water molecules surrounding DNA, resulting mainly in single-strand breaks and base damage.
Since there is no unique correlation between absorbed dose and induced biological effects, it is necessary to convert BNCT dose into an equivalent reference dose, for which the dose-effect relationship is well defined. Clinical experience with photon radiotherapy is used as a reference for this purpose, given the extensive clinical and radiobiological knowledge produced over years. Therefore, the dose administered in BNCT must be translated into photon equivalent units to predict the therapeutic effect and compare the results with other radiotherapy approaches. Specific model development supported by accurate radiobiological parameters is essential to achieve this conversion. These parameters are obtained from radiobiological experiments conducted on *cell cultures* and *animal models* irradiated with photons, neutrons, and neutrons in presence of boron.

I.3.1 RBE-weighted Dose Model

The model traditionally used in BNCT radiobiology and also in clinical practice is the **RBE-weighted dose model**, which was the first approach to grasp and describe the difference between the dose-response of photon irradiation and the BNCT mixed radiation field (Eq. I.3.2 [64]).
The conversion is performed by weighting each dose component by its Relative Biological Effectiveness (RBE). The RBE is defined as the ratio between the absorbed dose of a reference radiation, D_R, and the absorbed dose of the specific radiation under investigation, D_X, required to achieve the same level of biological effect (for example, 1% of cell survival) [65]

$$RBE_X = \frac{D_R}{D_X}. \tag{I.3.1}$$

The boron dose contribution is corrected with a factor called Compound Biological Effectiveness (CBE), whose value varies depending on the boron compound, the target tissue or cell, and the endpoint of the evaluation. RBE and CBE factors are typically obtained through *in vitro* radiobiological experiments using tumor cell lines. Cell survival is assessed as a function of dose, and a fixed endpoint is chosen to calculate the RBE and CBE [66].

Thus, the BNCT weighted dose is defined as

$$D_{BNCT} = CBE \cdot D_B + RBE_{n_{th}} \cdot D_{n_{th}} + RBE_{n_f} \cdot D_{n_f} + RBE_\gamma \cdot D_\gamma. \tag{I.3.2}$$

This formalism offers the advantage of being highly straightforward; however, it is based on assumptions that represent an oversimplification of the radiobiological reality. For example, it assumes that the biological effectiveness of each component is independent from all the others. This fact, together with the use of dose-independent fixed RBE-CBE factors (see below), often leads to an overestimation of the photon equivalent dose, which is inconsistent with the clinical effects reported in conventional radiotherapy.

To understand the need for a paradigm change, an illustrative example is introduced, as presented in [38], regarding the calculation of the RBE-weighted dose for a given combination of two radiation types that produces a survival level s', applying the RBE values for each radiation calculated for a different effect level, s.

Let consider two radiations, A and B, their combination AB, obtained using equal proportions of each radiation, and a reference radiation R. Assume that 3 Gy of radiation A, 6 Gy of radiation B, and 12 Gy of reference radiation R produce the same level of effect, s (see Fig. I.3.1).

The corresponding RBEs for radiation A and B and level s are $r_A^s = 4$ and $r_B^s = 2$, respectively. Suppose the RBE-weighted dose for the combination of 1 Gy of radiation A and 1 Gy of radiation B is to be computed.

The dose-effect curve for the combination of A and B radiation (denoted as AB, see Fig. I.3.1) corresponds to that obtained by using equal proportions of each radiation then the RBE-weighted dose is that which produces the same level of effect as the 2 Gy combination of A and B radiation, i.e. s'. In this example, it is observed that the photon dose required to reach the level s' indicated as the *True* value or d'_R, is 9 Gy.

Figure I.3.1 illustrates the procedures to calculate the RBE-weighted dose in BNCT for a given dose d_{AB}. A total absorbed dose $d_{AB} = 2$ Gy is assumed, with radiation A and B contributing in equal proportions to the dose. Then, the fixed RBE factors obtained for the effect level s, r_A^s and r_B^s, are used to calculate the RBE-weighted dose for the level s'

$$d'_R = r_A^s \cdot 1 \text{ Gy} + r_B^s \cdot 1 \text{ Gy} \tag{I.3.3}$$

The contribution of radiation A and B to the dose d'_R, represented by the first and second terms in Eq. I.3.3 is illustrated by the two horizontal arrows in Fig. I.3.1. By substituting $r_A^s = 4$ and $r_B^s = 2$ in Eq. I.3.3, the calculated RBE-weighted dose is $d'_R = 6$ Gy(RBE), which is lower than the depicted "True" value shown in the Figure. Conversely, if RBE factors for radiations A and B and survival level s' were used to compute the RBE-weighted dose for a total absorbed dose producing the surviving fraction $s < s'$, the obtained RBE-weighted dose would be overestimated in this case.

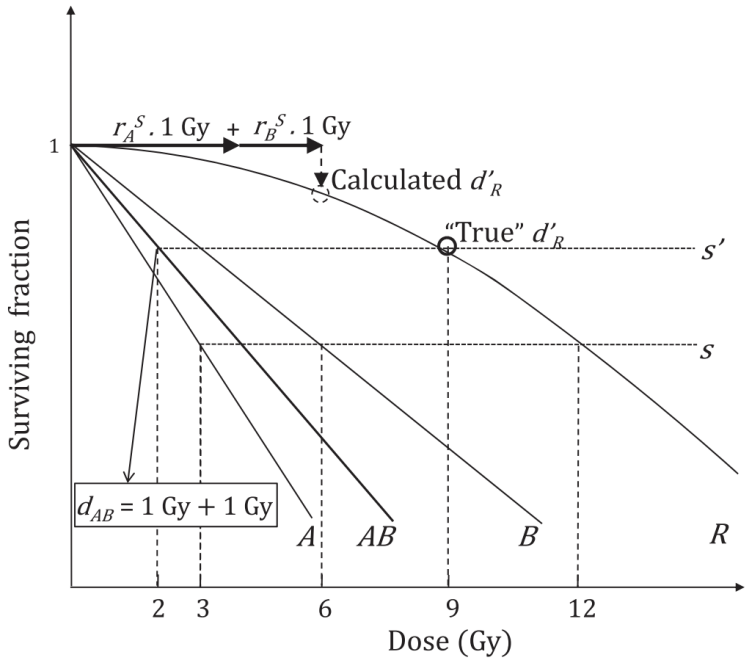

Figure I.3.1: *True vs. Calculated RBE-weighted doses for a mixed irradiation with 1 Gy of radiation A and 1 Gy of radiation B. In this example, RBE factors obtained for each individual radiation at the level s were used Illustration from [38].*

The weighted-dose model has been thus revised to calculate more realistic photon equivalent dose values using more comprehensive approaches. One of the new proposed formalisms is the Photon Isoeffective Dose Model, presented for the first time by González and Santa Cruz in 2012 [38, 67].

I.3.2 Photon Isoeffective Dose Model

The fixed-RBE approach, as illustrated above, has limitations that result in an inaccurate estimate of the photon equivalent dose given a certain level of biological effect.

The paper [38] describes a study on the clinical outcomes of the Argentine BNCT trial for single-fraction photon doses derived from melanoma patients treated with fractioned photon Radiotherapy, comparing the dose calculated with the RBE-weighted dose model and the Photon Isoeffective Dose Model. The figure of merit used for the evaluation is the probability of tumor control. Figure I.3.2 shows the distribution of tumor diameters and minimum lesion doses, assuming a tumor-to-blood concentration ratio of ^{10}B of 3.5, as used in the clinical trial. The corresponding clinical responses are indicated by solid dots (complete response) and open dots (other responses). In the region above the 95% iso- tumor control

probability for the modified linear quadratic model (TCP_{MLQ}) curve almost all lesions should show a complete response. However, this is not the case with the RBE-weighted approach (left panel), where the large number of open circles indicates the presence of different clinical outcomes for high dose values. This shows that the use of fixed-weighted RBE doses is not consistent with the expected tumor control probability from photon RT. In contrast, the photon isoeffective dose model provides a distribution that more accurately reflects expected lesion control, providing dose values that are significantly lower (right panel).

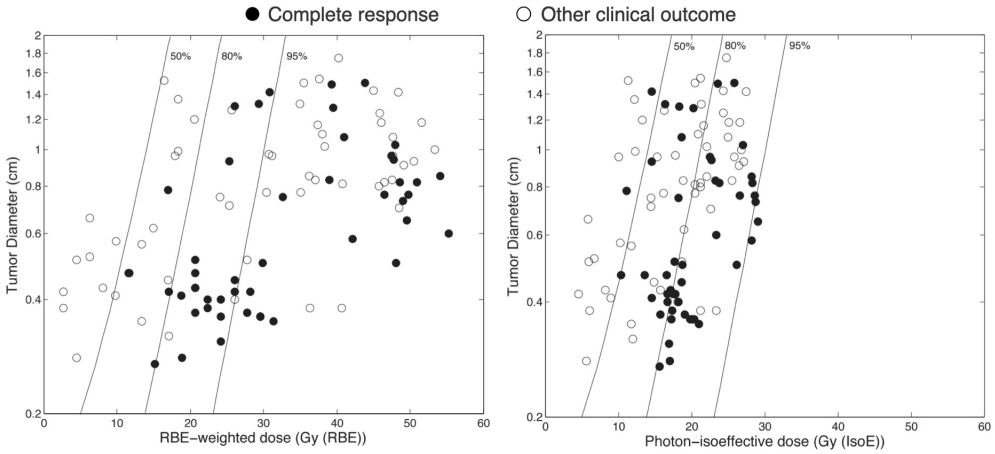

Figure I.3.2: *Scatter plots showing the distribution of tumor diameters and minimum dose administered to lesions with their response for RBE-weighted (left) and photon isoeffective dose (right) models. Filled circles indicate complete response, open circles indicate any other clinical outcome. Continuous lines represent the iso-tumor control probability curves computed with the TCP_{MLQ} for 50%, 80% and 95% of tumor control. Illustration adapted from [38].*

The approaches proposed in [38] leading to the Photon Isoeffective Dose model, include first-order sublethal lesions repair using the generalized Lea-Catcheside factor in the modified linear-quadratic model and considers synergetic interactions between different radiations, exploiting information obtained from cell survival experiments. It is assumed that the linear quadratic model adequately describes cell survival in terms of dose-response relationships, including dose-dependent repair of sublethal damage.
The basic tenet of the Dual Theory of Radiation Action (TDRA) holds that lethal damage can result from two distinct mechanisms

1. the direct action of a single event;
2. the random interaction of two independent events generates damage that, when combined, lead to cell lethality.

In the first case, the average yield of lethal lesions is proportional to the absorbed dose, while in the second case, it follows a trend proportional to the square of the

dose. To correlate the average yield of these lesions with cell survival, it is generally assumed that a single lethal lesion is sufficient to inactivate a cell and that the number of lethal lesions follows a Poisson distribution. These assumptions led to the formulation of the **Linear-Quadratic model** (LQ)

$$S(D) = e^{-(\alpha D+\beta D^2)}. \tag{I.3.4}$$

In TDRA, damage that by itself does not cause cell death is called a sublethal lesion or damage (SLD), which can interact with each other to generate lethal damage, if they coexist in space and time. The repair of first-order lesions was first studied by Lea and Catcheside. In the modified linear-quadratic formalism, $G(\theta)$ given by Eq. I.3.5, is a multiplicative factor that modulates the dose quadratic term. However, while the interaction between sublethal lesions requires strict spatial colocalization , $G(\theta)$ only considers their temporal coexistence without including the spatial distribution of the initial SLD.

$$G(\theta, t_0) = \frac{2t_0}{\theta}\left(1 - \frac{t_0}{\theta}\left(1 - e^{-\frac{\theta}{t_0}}\right)\right), \tag{I.3.5}$$

where t_0 is the fast or the slow characteristic repair times.
Mathematically it is possible to describe the factor $G(\theta)$ with the double kinetics of slow (t_{0s}) and fast (t_{0f}) repair as follows [68]:

$$G_k(\theta, t_{0f}, t_{0s}) = a_{kf}G(\theta, t_{0f}) + a_{ks}G(\theta, t_{0s}), \tag{I.3.6}$$

where a_{kf} and a_{ks} are the proportions of sublesions repaired by the fast and slow kinetics for radiation k (with $a_{kf} + a_{ks} = 1$).
Sublethal lesions generated by different radiations, if they coexist in space and time within the sensitive volume of the cell, can interact synergistically, producing an additional effect that cannot be explained by the simple sum of the two radiations. This phenomenon, known as radiation synergism, introduces mixed terms into the LQ formalism.
In light of the above, the Photon Isoeffective Dose Model is based on the following assumptions:

1. the dose-response relationship for cell survival is adequately described by the modified linear-quadratic (MLQ), which accounts for the repair of SLD as a function of dose rate.

2. Considering the synergism between radiations, the dose-response relationship for survival can be represented by including the additional mixed terms from the Dual Theory of Radiation Action, modulated by the G-factor.

The four dose components in the mixed field of BNCT are denoted as D_1, D_2, D_3, D_4, for *boron, thermal neutrons, fast neutrons and gamma*, respectively. D_R is the dose of a reference radiation R. The idea is to determine

$$D_R = D_R(D_1, D_2, D_3, D_4),$$

i.e. the dose of the reference radiation that induces the same level of survival produced by the combination of the four dose components.

I.3.2.1 Independent Action

The survival probability for the absorbed dose component i, with $i = 1, \ldots, 4$, is given by $S_i = S_i(D_i)$. The survival probability for the combination of the four dose components is $S = S(D_1, D_2, D_3, D_4)$. If no synergistic effects between the different radiations are considered, S can be written as

$$S(D_1, ..., D_4) = \prod_{i=1}^{4} S_i(D_i). \tag{I.3.7}$$

If $S_R(D_R)$ is the survival probability for the reference radiation, then the desired value of $D_R = D_R(D_1, D_2, D_3, D_4)$ must comply

$$S_R(D_R) = S(D_1, ..., D_4). \tag{I.3.8}$$

Assuming that only the dose components due to low-LET radiation can generate sublethal damage, and thus exhibit a quadratic dose dependence, the cell survival of the i component is expressed by

$$S_i(D_i) = \begin{cases} e^{-\alpha_i D_i} & i = 1, 2, 3 \\ e^{-(\alpha_i D_i + G_i(\theta)\beta_i D_i^2)} & i = 4 \end{cases}, \tag{I.3.9}$$

where α_i and β_i are radiobiological parameters, as well as the coefficients of the linear-quadratic model for a single dose fraction D_i, and $G(\theta)$ represents the generalized Lea-Catcheside factor. As explained above, the parameter α describes the contribution of the linear component of the cell response to radiation, proportional to the absorbed dose and typically associated with irreparable damage. The parameter β, represents the quadratic component, reflecting repairable sublethal damage and increasing with the square of the dose.
The equation I.3.8 becomes

$$-ln(S_R(D_R)) = \sum_{i=1}^{4} \alpha_i D_i + G_4(\theta)\beta_4 D_4^2 \tag{I.3.10}$$

$$= \sum_{i=1}^{4} r_i(D_R) \cdot D_i, \tag{I.3.11}$$

where

$$r_i(D_R) = \begin{cases} \alpha_i \dfrac{D_R}{(-ln(S_R(D_R)))} & i = 1, 2, 3 \\ (\alpha_i + G_i(\theta)\beta_i D_i) \dfrac{D_R}{(-ln(S_R(D_R)))} & i = 4, \end{cases} \tag{I.3.12}$$

The factors r_i represent the RBE coefficients as a function of the reference dose D_R. For the gamma component ($i = 4$), the repair of sublethal damage and the time course of dose deposition is taken into account via the factor $G_4(\theta)$. The RBE factors can be expressed as a function of the survival probability S, according to Equation I.3.13, where S^{-1} represents the inverse function of the cell survival probability for the reference radiation.

$$r_i(S) = \begin{cases} \alpha_i \dfrac{S_R^{-1}(S)}{(-ln(S))} & i = 1,2,3 \\ (\alpha_i + G_i(\theta)\beta D_i)\dfrac{S_R^{-1}(S)}{(-ln(S))} & i = 4 \end{cases}. \tag{I.3.13}$$

Let $S_R(D_R)$ be described by the linear-quadratic model for a single dose fraction. Then it can be expressed as

$$-ln(S_R(D_R)) = \alpha_R D_R + G_R(\theta)\beta_R D_R^2, \tag{I.3.14}$$

where α_R and β_R are the coefficients of the linear-quadratic model for the reference radiation R, while $G_R(\theta')$ represents the generalized Lea-Catcheside time factor, which takes into account the repair of sublethal damage as a function of irradiation time θ'. Given Eq. I.3.14, it is possible to obtain the expression of D_R as a function of the D_i

$$D_R(D_1,..,D_4) = \sum_{i=1}^{3}\left(\frac{\alpha_i}{\alpha_R + G_R(\theta)\beta_R D_R}\right) D_i + \left(\frac{\alpha_4 + G_4(\theta)\beta_4 D_4}{\alpha_R + G_R(\theta)\beta_R D_R}\right) D_4. \tag{I.3.15}$$

If the cell survival experiment is performed with a constant irradiation time, then the generalized time factor becomes a constant value, i.e. $G(\theta') = G_R$. In this case, equation I.3.15 is simplified to

$$D_R(D_1,..,D_4) = \frac{1}{2}\frac{\left(\frac{\alpha}{\beta}\right)_R}{G_R} \times \left(\sqrt{1 + \frac{4G_R}{\alpha_R\left(\frac{\alpha}{\beta}\right)_R}\left(\sum_{i=1}^{3}\alpha_i D_i + G_4(\theta)\beta_4 D_4^2\right)} - 1\right). \tag{I.3.16}$$

In this expression, the RBE factors do not appear explicitly; instead, the equation depends directly on the radiobiological parameters α and β of the linear-quadratic model, both for the BNCT field and for the reference radiation R. In the absence of synergism, this formulation corresponds to the Photon Isoeffective Dose Model.

I.3.2.2 Synergistic Action

To include synergism into the model, we consider that the sublesions produced by one radiation may combine with those generated by any other radiation to form

lethal lesions. For each component, the yield of sublesions per unit dose is given by $\sqrt{\beta_i}$. The cell survival for each radiation is then expressed by

$$-ln(S_i(D_i)) = \alpha_i D_i + G_i(\theta)\beta_i D_i^2, \quad i = 1, 2, 3, 4. \tag{I.3.17}$$

From the TDRA model, it is possible to derive the expression describing the synergism between two components i and j,

$$-ln(S_i(D_i, D_j)) = G_{ij}(\theta)\sqrt{\beta_i\beta_j}D_iD_j, \quad i \neq j = 1, 2, 3, 4. \tag{I.3.18}$$

$G_{ij}(\theta)$ denotes the time factor that takes into account the first-order repair of the sublesions produced by the radiation i (j) during irradiation. The cell survival for the combination of the four radiations is given by

$$-ln(S(D_1, D_2, D_3, D_4)) = \sum_{i=1}^{4} \alpha_i D_i + \sum_{i=1}^{4}\sum_{j=1}^{4} G_{ij}(\theta)\sqrt{\beta_i\beta_j}D_iD_j. \tag{I.3.19}$$

When $i = j$, the quadratic term is included.
If the equation I.3.14 represents cell survival for the reference dose R, then it is possible to write

$$\alpha_R D_R + \beta_R G_R(\theta')D_R^2 = \sum_{i=1}^{4} \alpha_i D_i + \sum_{i=1}^{4}\sum_{j=1}^{4} G_{ij}(\theta)\sqrt{\beta_i\beta_j}D_iD_j. \tag{I.3.20}$$

Considering $G_R(\theta') = G_R$, the expression for the Photon Isoeffective Dose is

$$D_R(D_1, ..., D_4) = \frac{1}{2}\frac{\left(\frac{\alpha}{\beta}\right)_R}{G_R} \times \left(\sqrt{1 + \frac{4G_R}{\alpha_R\left(\frac{\alpha}{\beta}\right)_R}\left(\sum_{i=1}^{4} \alpha_i D_i + \sum_{i=1}^{4}\sum_{j=1}^{4} G_{ij}(\theta)\sqrt{\beta_i\beta_j}D_iD_j\right)} - 1 \right). \tag{I.3.21}$$

Both the RBE-weighted and the Photon Isoeffective Dose models, as presented so far, assume a uniform boron concentration throughout the tumor volume, at both tissue and cellular levels.
What happens when the dosimetry is considered at the subcellular scale, separating nucleus and cytoplasm? Is the microdistribution of boron-10 equal in the two cellular compartments?
If the answer is *no*, meaning that the **distribution** is **not uniform**, the macrodosimetric quantities, including dose, would no longer be adequate to describe the stochastic mechanisms of energy deposition. In that case, it would be necessary to introduce new quantities belonging to microdosimetry, capable of representing the interaction of radiation with matter in its stochastic nature.
This thesis aims to answer this question through neutron autoradiography experiments to determine the microdistribution of boron-10 between nucleus and cytoplasm. In parallel, the goal is to develop a mathematical model capable of calculating the dose in BNCT, taking into account the experimental non-uniformity of boron distribution at the sub-cellular level.

CHAPTER I.4

MICRODOSIMETRY AND BORON-10 MICRODISTRIBUTION

In the previous chapter, two models for converting BNCT dose into photon - equivalent units were illustrated, both based on the assumption of a uniform boron distribution within the tumor volume at macroscopic and microscopic levels. However, going at the subcellular scale, of the order of the micrometer, boron distribution may be non-uniform. Therefore, the dose (being an average magnitude) is insufficient to describe the stochastic mechanisms of energy deposition at such small sites, and thus it may not the suitable quantity to correlate with cell damage. Microdosimetry enables the study of the spatial and statistical distribution of the energy deposited by ionizing radiation at microscopic sites, providing a more accurate description of biological effects than conventional dosimetric quantities.

I.4.1 Fundamentals of microdosimetry

The interaction of ionizing radiation with matter is a stochastic process that occurs discretely. This is due to the inherently probabilistic nature of interactions between radiation and matter, which are subject to random fluctuations. Therefore, the energy imparted varies according to the probability distribution in microscopic structures. The smaller the sensitive site considered, the more relevant these statistical variations become. In microscopic sites, fluctuations in the imparted energy can be very high and, as a result, the statistical mean value of this quantity becomes meaningless. Knowledge of the absorbed dose, therefore, does not provide sufficient information on the energy deposited in cellular and subcellular structures. Given the nature of the problem, the quantities involved are represented by random variables, which can be described by their probability distribution, derivatives, and moments.
Since the cell consists of a nucleus and a cytoplasm, with size of the order of

micrometers, and the nucleus contains DNA, whose is the most sensitive target to radiation, it becomes necessary to operate at the microscopic scale to accurately describe the imparted energy.

This is why **microdosimetry** becomes relevant, which, within radiation biophysics, is the discipline that investigates the spatial, temporal, and spectral characteristics of the stochastic process of energy deposition in microscopic structures. This discipline originated from work initially carried out by Harald Rossi and Albrecht Kellerer, who noted that energy concentrations in microscopic regions were more relevant to the biological effects of radiation than the values calculated on the theoretical basis of LET [69].

Microdosimetry was developed to study the distribution of absorbed energy in small spatial and temporal scales, with the aim of better understanding the relative effectiveness of different types of radiation. This approach is especially relevant in radiobiology, where it helps to correlate initial radiation interactions with short- and long-term biological effects. The energy deposited by radiation can trigger molecular reactions within microseconds, while macroscopic effects, such as carcinogenesis, may occur after years or decades. Microdosimetry makes it possible to investigate the initial processes that lead to cell damage.

The development of microdosimetry led to two main approaches: *regional microdosimetry*, developed by Rossi, based on the measurement and study of energy deposition spectra using proportional counters [70]; and *structural microdosimetry*, proposed by Kellerer, which, using integral geometry tools, deals with the study of the superposition of the interaction pattern of radiation and energy deposition in matter within the sensitive structures of the object of interest [71, 72, 73].

Fundamental concepts of microdosimetry are defined below, some of which will be used in this work.

Microdosimetry is based on the concept of **site**: a region of defined dimensions.

Define ϵ as the energy deposited in a given volume of the site, it is equal to the sum of the individual energy transfers, ϵ_i, that occur at the interaction points within that volume, $\epsilon = \epsilon_i$.

Another important concept is the **event**, which denotes the crossing of a region by a particle or its secondaries, resulting in the deposition of energy. An event occurs whenever there is at least one energy transfer associated with the trajectory of a particle within the region of interest. Importantly, an event consists of statistically correlated transfer points, whereas distinct events are statistically independent.

The term *single energy deposition event* refers to the energy deposited by correlated charged particles passing through a volume, and reflects statistical fluctuations in both the number and type of energy deposition processes. Average values are often used to describe these variations; however, as already mentioned, this simplification results in the loss of information regarding the distribution of deposited energy at microscopic sites. For this reason, quantities such as LET and absorbed dose represent statistical average values that do not consider the intrinsic fluctuations of the stochastic process of energy deposition.

Let us define a quantity that characterizes the distance traveled by particles when they pass through a convex body of interest (cell or its nucleus). A particle traverses a volume along a rectilinear trajectory called **chord length**, l, which is a random variable described by a probability distribution function [74].
It is now possible to introduce the concepts of the main microdosimetric quantities: the **linear energy** and the **specific energy** [75]. Linear energy is a random variable that refers to the increments of deposited energy produced by single events. It represents the stochastic analogue of the LET, is typically expressed in [keV μm^{-1}] and is defined as the ratio of the energy deposited by a single event, ϵ_1, to the average length of the chord of the body in question, $\bar{l}$, as shown in the equation I.4.1

$$y = \frac{\epsilon_1}{\bar{l}}. \tag{I.4.1}$$

Although the linear energy quantity provides a more adequate approach to radiation quality, it is necessary to define another magnitude to establish a relation with dosimetry. This quantity is the specific energy, z, which is defined as the ratio between the energy deposited, ϵ, by the ionizing radiation and the mass m of the volume in question, according to the following equation I.4.2

$$z = \frac{\epsilon}{m}. \tag{I.4.2}$$

From its dependence on ϵ, it can bee noted that z is a stochastic quantity and, consequently, it is useful to consider its probability distribution. The value of the distribution function, $F(z)$, represents the probability that the specific energy is less than or equal to z. Its probability density function, $f(z)$, is the derivative of $F(z)$ with respect to z, i.e. $f(z) = \frac{dF(z)}{dz}$. The expected value of z, with distribution $f(z)$, is defined as the mean specific energy

$$\bar{z} = \int_0^\infty z f(z) dz. \tag{I.4.3}$$

The specific energy in a volume can result from one or more deposition events. The distribution function $F_1(z)$ represents the conditional probability that a single event deposits specific energy less than or equal to z, and its density function, $f_1(z)$, describes the distribution of z for single events. Then, it is useful to distinguish between the microdosimetric spectrum of a single event, $f_1(z)$, and the general multi-event distribution, $f(z)$.
The distributions $f(y)$ and $f_1(z)$ represent the frequency distributions of linear energy transfer and specific energy, respectively. The first moment of these distributions given by the following expressions corresponds to the frequency-averaged linear energy y_F and specific energy z_F. The dose-averaged quantities y_D and z_D are defined as the ratio of the second to the first moment of these frequency distributions, and represent the average energy weighted by the dose:

$$y_F = \int_0^\infty y f(y)\, dy, \quad y_D = \frac{1}{y_F} \int_0^\infty y^2 f(y)\, dy, \tag{I.4.4}$$

$$z_F = \int_0^\infty z f_1(z)\, dz, \quad z_D = \frac{1}{z_F} \int_0^\infty z^2 f_1(z)\, dz. \tag{I.4.5}$$

I.4.2 BNCT microdosimetry

In BNCT, microdosimetry plays a crucial role, as the energy distribution in the irradiated tissue is not homogeneous. Especially when considering that boron uptake within a cell is different in the nucleus and in the cytoplasm and can vary within each of these regions. This distribution may in fact differ between cells from the same tissue, tumor or normal, or even in cells from the same cell culture. Therefore, to obtain an accurate estimate of the biological dose, it is essential to know the spatial microdistribution of boron in cells. Without this knowledge, the macroscopic dose calculated assuming a uniform boron concentration between the nucleus and cytoplasm is the only possibility, albeit it might be inaccurate.
The first attempts to describe the microdosimetric aspects of BNCT date back to the pioneering work of Zamenhof and colleagues [76], who introduced the concept of *compound factor* or *geometric factor*, i.e., ratio that describe the relative efficiency of the dose as a function of the intracellular distribution of ^{10}B compared to a uniform distribution. Studies had shown that the positioning of ^{10}B in the nucleus is significantly more effective than in the cytoplasm or cell surface, stimulating the development of molecules with intranuclear targeting. Other key concepts introduced were the cross-fire effect, i.e., the impact of particles emitted in a cell hitting neighboring nuclei, and the analysis of the "quality" of hits with effectiveness functions such as the Hit-Size Effectiveness Function (HSEF).
Subsequently, Wuu et al. [77] expanded this approach by analyzing the impact of boron distribution at the cellular level on radiobiological efficacy, showing that intranuclear localization is significantly more effective than cytoplasmic localization.
More recently, Santa Cruz and Zamenhof in [78] emphasize that dose calculation alone is not sufficient to describe the biological effectiveness of the neutron capture reaction of ^{10}B, for two main reasons: (i) the microdistribution of the boron-containing compound at the cellular level, and (ii) the inherently stochastic nature of the energy deposition process by the high LET particles produced (α and ^{7}Li). Both of these aspects strongly influence the biological response and render inadequate the simple assumption of boron uniformity used in models based on kerma coefficients. To overcome these limitations, a rigorous analytical formalism has been developed, based on microdosimetric theory and integral geometry, that is capable of describing the stochastic distribution of dose in microscopic sites in a generalized manner. The model introduces the Microscopic Dose Correction Factor (MDCF), which corrects the average dose by taking into account the shape and size of the sensitive site, the non-uniform distribution of particle sources inside and outside the volume under consideration. The MDCF will be described in detail in Chapter III.1, as it represents the starting point for the microdosimetric approach developed in this thesis.

More recent studies have explored even more detailed approaches. One work employs the Monte Carlo code TOPAS-nBio [79]. Authors modified the ionization cross-section for lithium through the effective charge cross-section method and the phenomenological modification of the parameter. Furthermore, they verified that the range and stopping power of lithium, alpha particles, and protons align with the specific energy fields in BNCT, ensuring the applicability of the physical models and cross sections used.
Another relevant study analyzes a microdosimetry model based on the Stochastic Microdosimetric Kinetic (SMK) model, providing further insights into the BNCT microdosimetry [80]. This study develops the model to estimate the biological effectiveness of BNCT by taking into account intra- and intercellular heterogeneity in the distribution of ^{10}B, based on the SMK model. The model incorporates the synergistic effects of the mixed radiation field of the BNCT, and it successfully reproduces the measured Survival Fraction of tumor cells and the RBE and CBE factors in different experiments. It highlights the importance of considering the synergistic effects and dose dependence of RBE and CBE when assessing the therapeutic efficacy of BNCT.
The analysis presented in this section highlights the crucial role of accurately knowing the microdistribution of ^{10}B to perform microdosimetry that reflects the biological reality. One of the primary objectives of this thesis is to avoid relying on theoretical assumptions of subcellular distribution and instead to employ experimentally determined distributions for a representative GBM cell line. For this reason, the experimental part of this work focused on imaging and quantifying boron concentration using the U-87 cell line and neutron autoradiography.

I.4.3 Neutron Autoradiography with Nuclear Track Detectors

Only a limited number of techniques allow a precise study of ^{10}B microdistribution at the cellular level. Among these, neutron autoradiography [81, 82] stands out as a particularly suitable method option due to its high resolution and low cost. Neutron autoradiography is a methodology that allows to correlate the ^{10}B microdistribution in a biological matrix of interest and the damage caused by the impact of charged particles on the surface of a detector [83, 84]. This technology is based on using Solid State Nuclear Track Detectors: SSNTD. SSNTDs are thermal or electronic isolating material, whether organic or inorganic. The peculiarity of SSNTD is their ability to permanently preserve the structural damage caused by the impact of charged particles along their trajectory, on their surface.
Based on the track formation mechanisms and etch behaviors, SSNTD are generally classified into several categories, which can be distinguished according to the constituent material of the detector: crystal, glass, or polymer. Figure I.4.1 shows a classification with some examples of commonly used and newly developed materials [85].

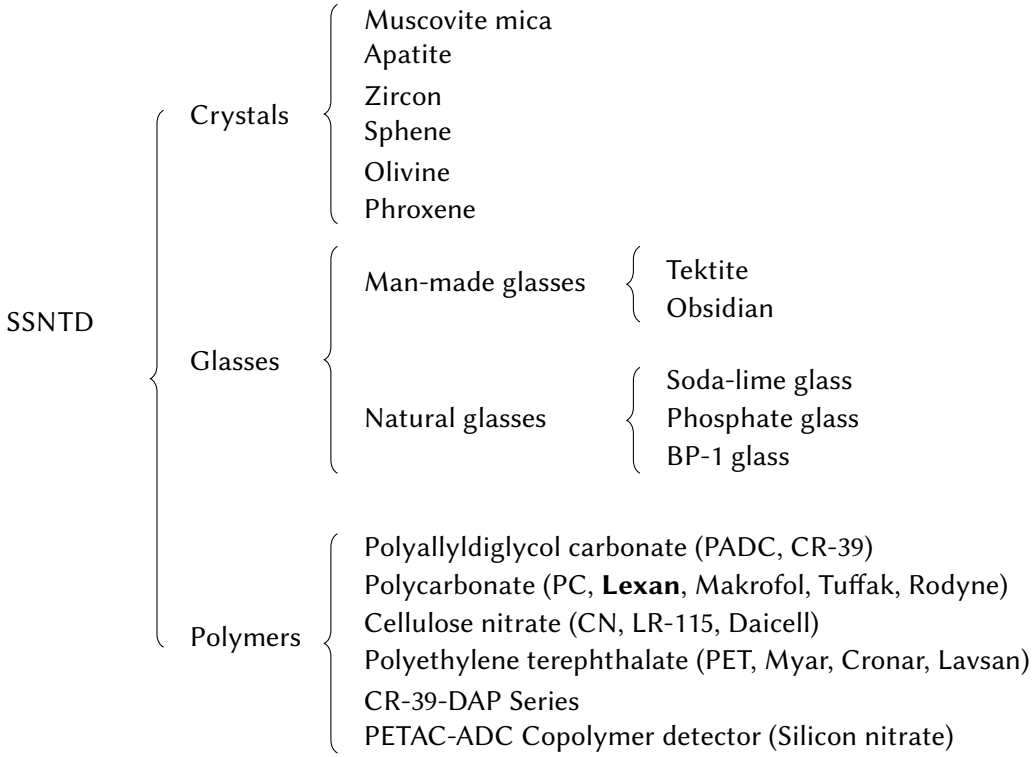

Figure I.4.1: *Classification of the main types of Solid-State Nuclear Track Detectors (SSNTDs) based on the detector material: crystals, glasses, and polymers, with representative examples for each category. Figure adapted from [85].*

In particular, polymers demonstrated to be particularly suitable as SSNTD, due to their sensibility, precision and versatility. Plastic detectors are more sensitive to heavy charged particles, including those with low charges, up to protons with $Z = 1$, compared with inorganic crystalline solids and glasses. Sensitivity varies according to the type of polymer. CR-39 (polyallyldiglycol carbonate, PADC) is the most commonly used sensitive detector, with the ability to record charges as low as $Z \geq 1$. One disadvantage of CR-39 for BNCT purposes is that it is sensitive to protons coming from the nitrogen capture reaction, which leave detectable tracks in CR-39. In polycarbonate, instead, recoil protons do not generate such background tracks, making it preferable to CR-39 in this respect.
Among polycarbonates, the most common and most widely used in its class is Lexan, the trade name for a bisphenol-A-based polycarbonate foil produced by the SABIC Innovative Plastics Company.
Nuclear track detectors have applications in many areas of science and technology [86], including personal neutron dosimetry [87], occupational exposure monitoring, mining studies, nuclear physics, astrophysics, radon detection, and radiopharmaceuticals. One use of particular note is in the autoradiography of objects containing elements capable of emitting charged particles (such as $^{238}\mathrm{U}$) [88], or elements that, as a result of specific nuclear reactions (as in the case of $^{10}\mathrm{B}$), gen-

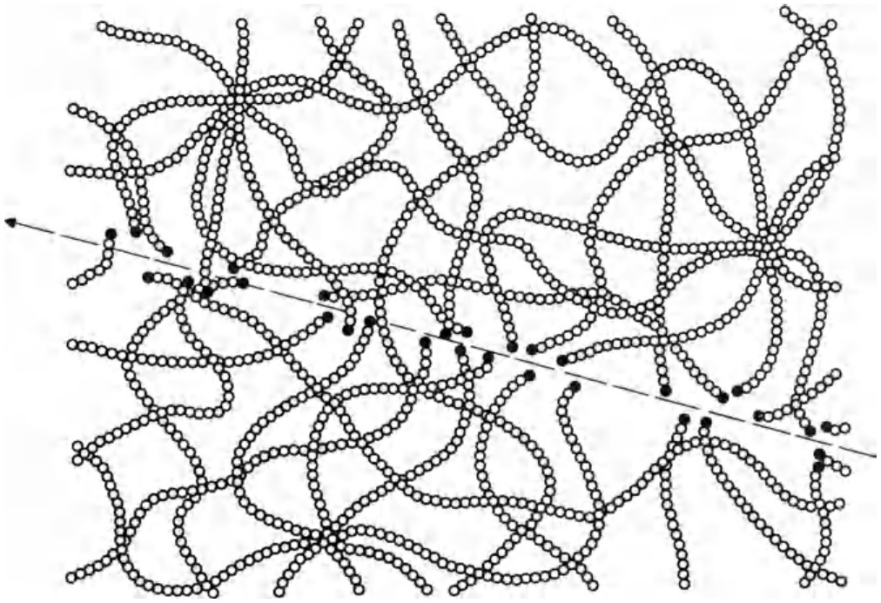

Figure I.4.2: *Chain-breaking mechanism in the formation of etchable tracks in higher polymers. Chain breaks by the passage of a heavy charged particle causes preferential etching at a lower radiation damage density. Illustrtion from [85].*

erate charged particles. In contact with an NTD, such objects can produce an image composed of the tracks left by the emitted particles.

In polymers, the passage of heavy charged particles causes localized breaking of molecular chains, resulting in a reduction in their length. This process requires an energy of the order of only $\sim 2\ \mathrm{eV}$, significantly less than that required to ionize an atom in inorganic solids. The free ends thus formed are highly reactive and are easily attacked by appropriate chemical reagents, facilitating the formation of etchable tracks. This mechanism is illustrated in Fig. I.4.2 [85, 89]. When such detectors are placed in contact with a material containing an emitting element, an autoradiography is obtained, in which the emitted particles interact with the detector, making visible the distribution of the element within the sample.

When the SSNTD is placed in close contact with a biological matrix (e.g., cells incubated with a borated compound and directly cultured on the SSNTD), the detector registers the damage, called nuclear track, produced by the alpha particle or the lithium ion originating from the capture reaction ($^{10}\mathrm{B}(n,\alpha)^{7}Li$) with the $^{10}\mathrm{B}$ nuclei in the biological matrix. The two charged particles are emitted back-to-back, meaning that they are ejected in opposite directions. Only one of these particle per $^{10}\mathrm{B}$ atom produces damage on the surface of the detector and is consequently recorded. Therefore, it is possible to determine the concentration of $^{10}\mathrm{B}$ in biological samples employing quantification and tracks analysis.

The tracks caused by charged particles are called *latent*, because they are initially invisible even under the optical microscope (< 50 Å). However, chemical etching

can selectively remove the detector material surrounding these tracks at a faster rate (track etch velocity, V_t) than in the undamaged bulk (bulk etch velocity, V_b), enlarging the tracks and making them distinguishable [85].
There are several approaches to the neutron autoradiography technique that allow both qualitative and quantitative analysis. The generation and exploitation of tracks depend on neutron fluence and the conditions of the chemical attack.
The high neutron fluence, combined with a prolonged chemical etching time, leads to the formation of overlapping tracks that delineate a map of the boron distribution. This approach can be used as a qualitative imaging technique, but it also allows for quantification through optical density analysis of gray levels [90]. In this way, a qualitative image can be transformed into a quantitative representation in which each concentration corresponds to a specific gray scale. In contrast, a low fluence and short chemical attack avoid overlapping tracks, making it possible to count them directly and quantify them based on the surface density of the number of tracks. However, both approaches require a preliminary calibration step. Variations in optical density on the NTD detector surface reflect the spatial distribution of $^{10}\mathrm{B}$, while quantitative image analysis at high neutron fluence allows the determination of its absolute concentration.
Figure I.4.3 shows the workflow of the quantitative technique used in this work. It can be seen how the biological matrix, on which the $^{10}\mathrm{B}$ distribution is to be calculated, can be derived from both animal experiments and cell cultures. In particular, line a $(1.a, 2.a, 3.a)$ illustrates how tissue is obtained from an animal model after infusion of the boron-containing compound and euthanasia, while line b $(1.b, 2.b, 3.b)$ shows a cell culture directly grown and incubated with the borate compound on the passive detector. In this work, only line b is considered. All other steps in the image represent the standard steps of neutron autoradiography, which will be described in the following sections.

I.4.3.1 Etching

As mentioned before, the latent tracks need to be amplisied by a chemical etching. The etching conditions comprise three aspects [85]:

1. the composition of the chemical reagents used as an etching agent (alkaline solutions are used in the case of many polymeric NTDs);

2. the temperature during the etching process;

3. the duration of the chemical attaque.

The chemical agent is specific to each type of detector material. In general, a higher concentration of the chemical agent and a higher temperature accelerate the etching process, while longer times increase the diameter of the etched tracks. During the chemical attack, the entire detector is exposed to the chemical solution, which selectively removes the material, making the tracks visible under optical microscopy. This process results from a combination of two phenomena:

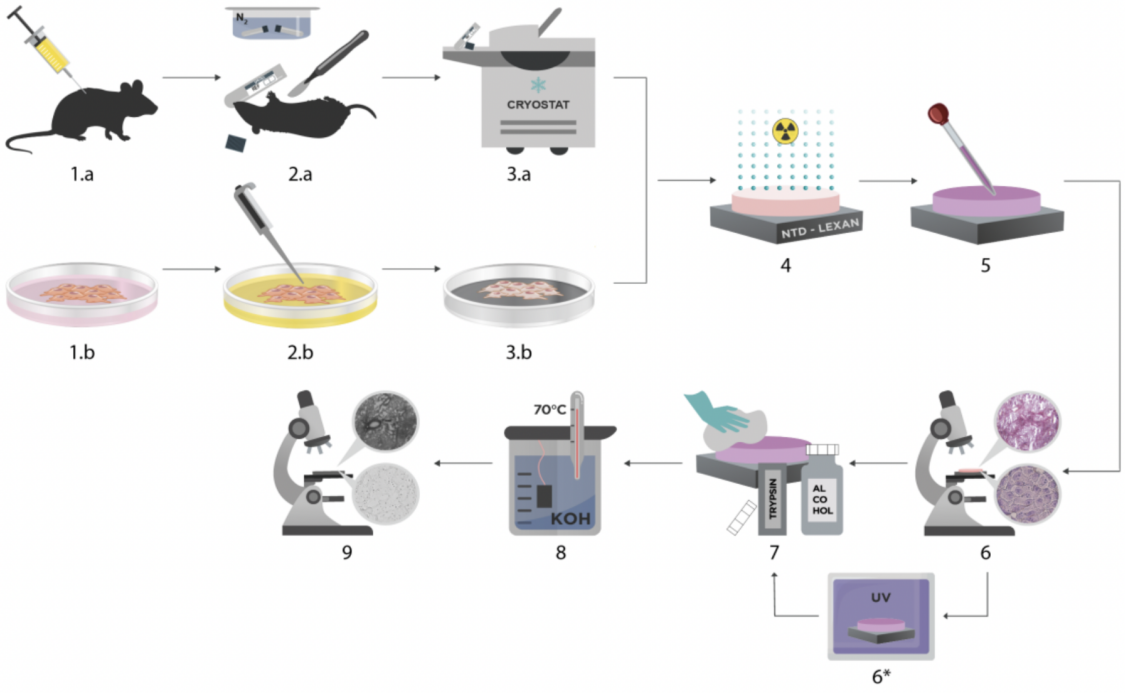

Figure I.4.3: *Workflow for the generation of autoradiography images using nuclear track detectors (NTDs). The initial steps differ depending on whether tissue samples (up) or cell cultures (down). Subsequent steps, including neutron irradiation, staining, region of interest (ROI) identification, optional UV-C sensitization, biological material removal, chemical etching, and microscopic analysis. Illustration from [91].*

the removal of virgin material and the simultaneous removal of damaged material, which occur at different rates. In particular, two etching velocities can be distinguished:

1. **Bulk etching velocity** V_b: the velocity at which undamaged material is uniformly removed from the detector. This phenomenon acts on both surfaces (the surface previously in contact with the sample and the bottom). For the etching condition in this work, see (Chapter III.2) V_b =20 μm/h [92] .

2. **Track etching velocity** V_t: the rate at which the damaged material along the track is removed from the solution.

Track geometry is strongly dependent on the ratio V_t/V_b. In turn, these two velocities are influenced by several factors, including the physical characteristics of the particles (charge, mass, velocity and angle of incidence of the projectile), the etching conditions (type of solution, temperature, and exposure time), and the nature of the detector material [85].
The etching rate along the track, V_t, depends on the amount of damage present in the central region and may vary along the path of the particle. In contrast, the

etching rate of the undamaged material, V_b, is an intrinsic property of the detector and, given equal chemical attack conditions, remains constant and isotropic. The value of V_b is mainly determined by the chemical composition and concentration of the etching solution, as well as the temperature and homogeneity of the solution [93].
To better understand the etching phenomenon, Figure I.4.4 schematically illustrates the formation of a track produced by an incident particle perpendicular to the detector surface. For simplicity and in order to describe the phenomenon in analytical form, it is assumed that V_b and V_t remain constant during the chemical attack process, the track can be modeled three-dimensionally as a cone, the opening angle of which is determined by the rotation of the etching surface around the trajectory of the particle. The formation of the track is the result of the competitive interaction between V_b and V_t. Denoting by L the length of the track and by t the etching time, their relationship is expressed by the following equation

$$L = (V_t - V_b) \cdot t. \tag{I.4.6}$$

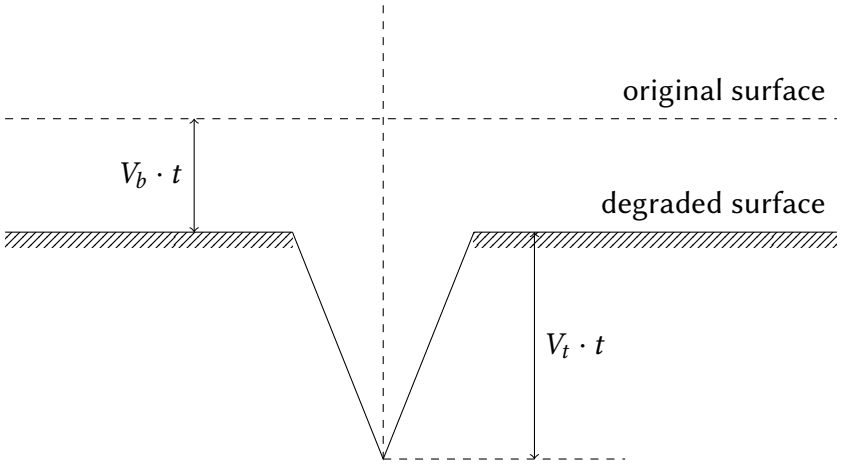

Figure I.4.4: *Schematic view of a particle track with velocities V_b and V_t. Illustration adapted from [85].*

An illustrative microscopic image (100x) of the tracks after the chemical attack is shown in Fig I.4.5. Each black dot is formed by the impact of either an α or ^{7}Li particle and it represents a neutron capture event, indicating the presence of a ^{10}B atom. As can be inferred from the image, the correlation of each track location with the nucleus or cytoplasm of the cell is not straightforward, since the tracks appear as isolated points without visible reference to the underlying cellular structures in the etched Lexan. The cell morphology is not directly preserved in the detector material, and without an independent marker for the nucleus and cytoplasm boundaries, it is difficult to assign each track to a specific subcellular compartment. To record this spatial correlation, it is necessary to delimit the contours of the two subcellular compartments. In [94], it was studied the imprint formation on Lexan by exposing the sample to ultraviolet radiation. In addition to

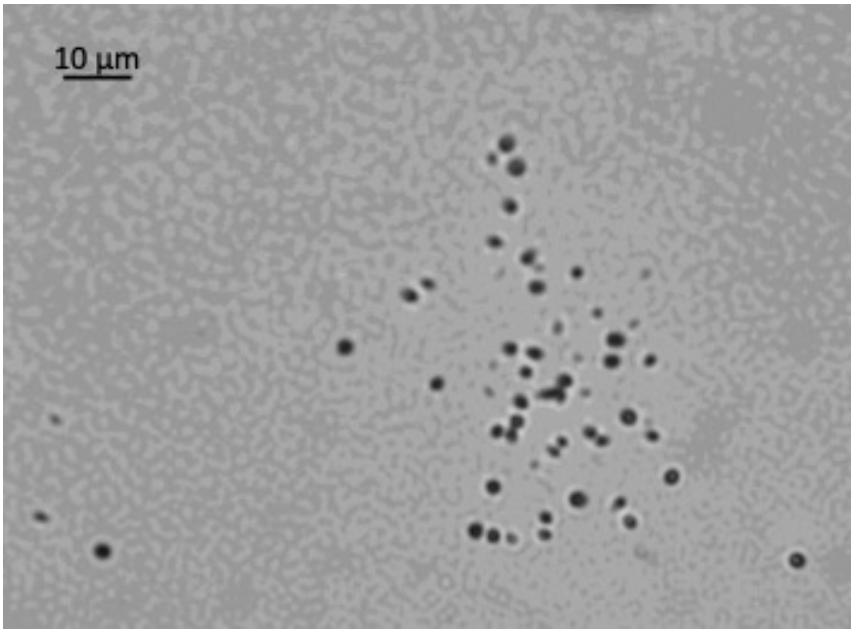

Figure I.4.5: *Example of an image of tracks coming from U-87 cells incubated with BPA (80ppm), 4 h, observed under an optical microscope at 100x magnification. Fluence:* 10^{12} $n \cdot cm^{-2}$*, etching: PEW 70 °C, 4 min.*

detecting tracks, the etching process can also reveal the imprint of the biological sample, representing an alteration of the material induced by exposure to UV-C radiation (see Section I.4.3.2)). In these regions, the material structure is altered, locally affecting the bulk etching rate, which is altered compared to undamaged areas. This change in the rate of chemical attack leads to preferential removal of the degraded material, thus also enabling the visualization of the imprint.

I.4.3.2 UV-C irradiation

The neutron autoradiography technique involves removing the sample from the detector, which undergoes chemical attack to develop the latent tracks produced by the particles emitted from the tissue. Although reference markers are usually applied [95, 96], the procedure allows the correspondence between the emitter site and the location of the track to be established only with limited accuracy.
While high-resolution quantitative autoradiography [97] represents a sophisticated technique that allows simultaneous observation of tissue sections and nuclear tracks, it relies on the use of thin foils of SSNTD and a system to protect the sample during chemical attack.

An alternative approach, proposed in [98], involves creating an *etched replica* of the biological sample directly on the surface of the detector. Such an image, revealed by the same chemical attack used to develop the nuclear tracks, allows simultaneous observation of the sample morphology and the tracks themselves.

Therefore, the position of the $^{10}\mathrm{B}$ atoms in the cellular compartments could be known precisely by simultaneous observation of the nuclear tracks and the cells on the detector. Among the possible techniques for high-resolution autoradiography [99], an alternative is the sensitization of the detector with UV-C radiation to create reliefs in the SSNTD. This work is described in detail in [100].
The ultraviolet spectrum is divided into three regions according to wavelength: **UV-A** for $\lambda = 320 - 400$ nm, **UV-B** for $\lambda = 280 - 320$ nm, and **UV-C** for $\lambda = 200 - 280$ nm. For wavelengths in the range of **UV-C** radiation ($\bar{\lambda} \approx 254$ nm), two simultaneous phenomena are observed in polycarbonate [101, 102, 103]:

1. **Photodegradation**, which causes the polymer chains to split;
2. **Photo-Fries process**, which causes a rearrangement of the polymer chains.

The damage produced by UV-C exposure results in an increase of V_b.
If a biological matrix is interposed between the radiation and the NTD, the etching solution will remove the surface of the detector at different rates, depending on the localized degradation resulting from the sample's topography. This process is responsible for the **imprint** formation.
In [104], is described how it is possible to generate the imprint of a given biological material by exposing the "cells+NTD" assembly to ultraviolet (UV-C) irradiation. In particular, it was shown in [100] that the combination of UV-C irradiation with previous staining of the cell culture enhanced cellular imprint formation. Cellular imprint formation is related to the non-uniform damage on the detector surface due to differences in absorption of UV-C radiation by different cellular structures. This effect can be highlighted with the dyeing that acts as a "solar protector" of ultraviolet radiation. The damage caused by UV-C radiation affects the chemical attack rate (bulk velocity) of the material, and this change is what produces the formation of the cellular imprint. In Figure I.4.3, this step is represented by point 6^*.
A scheme of the UV-C irradiation facility is presented in Fig. I.4.6.
An important aspect to stress is that UV-C radiation does not directly produce nuclear tracks on the detector but does affect its recording properties. This phenomenon is known as the **fading effect**. Although few studies include analysis of the phenomenon in polycarbonate, several groups have investigated this, finding that the number of tracks decreases with time of exposure to UV-C radiation, but obtaining mixed results and without reaching a satisfactory explanation.
In [105] the authors study this phenomenon in Lexan for several particles, including the products of the neutron capture reaction in ^{10}B and other heavier ions. It was observed that the removal of the surface layer exposed to UV-C radiation can far exceed the range of ions in the detector, providing a possible explanation for the loss of the tracks formed in the material. The work concludes that detector sensitization following exposure to UV-C light is due to photodegradation of the polymer. This process could be explained by a variety of competing wavelength-dependent mechanisms. Photodegradation of polycarbonate results in an increase

of the average bulk attack rate (V_b) in polycarbonate foils exposed to UV-C compared with that in foils not exposed to ultraviolet light. This phenomenon must therefore be appropriately considered as a factor of uncertainty in the procedures of track analysis and quantification.

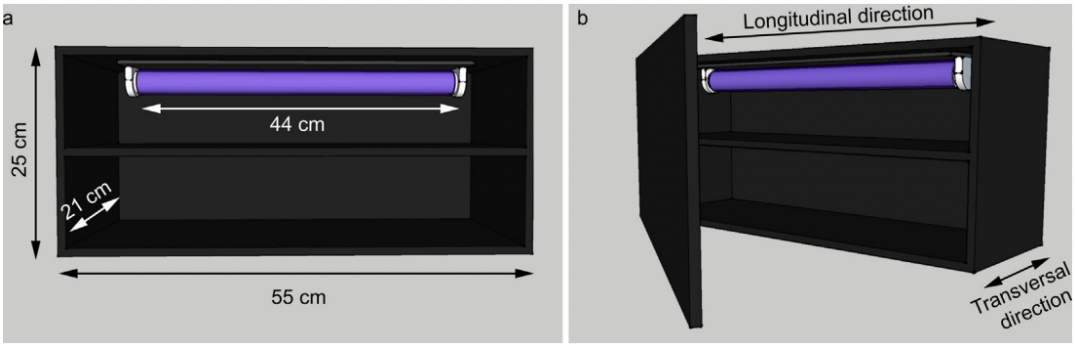

Figure I.4.6: *Ultraviolet lamp configuration UV-C ($\lambda = 240\,nm$). Illustration taken from [104].*

Part II

Towards an adequate description of the dose-response relationship in BNCT of Glioblastoma Multiforme

CHAPTER II.1

RADIOBIOLOGICAL EXPERIMENTS

Introduction

In 2007, the World Health Organisation (WHO) classified primary Gliosarcoma (GSM) as a grade IV neoplasm and a variant of Glioblastoma Multiforme (GBM) [106]. By definition, GSM is a well-circumscribed lesion characterized by the presence of identifiable biphasic metaplastic glial, sarcomatous, and mesenchymal components [107]. The pathogenesis of GSM still remains unknown.

GSM and GBM are treated with the same approaches, although they are different tumors. Some authors [108, 109] reported that GSM shares genetic alterations and chromosomal imbalances with GBM.

The GSM incidence is between 1.8% and 2.8% compared to GBM. Like other glial tumors, it predominantly affects men between 60 and 70 years of age [110, 111]. Despite the similarities between the two neoplasms, there are features of GSM that differ from GBM, including location and radiographic appearance. Furthermore, while GBM rarely gives rise to extracranial metastases, GSM has a known propensity to metastasize [112, 113, 114]. The metastatic capacity of GSM has led to the conclusion that GSM and GBM are two clinically separate entities. In particular, the metastatic potential of GSM has been observed to depend on its sarcomatous component, which is absent in GBM [115, 116, 117].

Treatment options for GSM include surgical resection of the tumor, post-operative radiotherapy, and chemotherapy [111, 115, 118].

The BNCT dosimetry of GBM has traditionally been calculated using the radiobiological parameters of GSM, as it is considered a close sibling of GBM. However, as discussed above, GSM represents a unique and distinct clinico-pathological entity. Therefore, a precise classification of these tumors is essential for effective treatment planning, as their radiobiological responses can differ substantially [119].

In this part of the thesis, a suitable model for the calculation of Photon Isoeffective Dose in GBM is presented for the first time, supported by ad hoc *in vitro* radiobiological data. To this end, human Glioblastoma cell cultures (U-87 cell line) were irradiated, and their specific radiobiological parameters were determined.
The work consists in:

1. the production and the analysis of new radiobiological data using the U-87 cell line;

2. the evaluation of the impact of using different photon sources as the reference radiation;

3. the comparison of photon isoeffective dose obtained with different sets of radiobiological data in a GBM patient who received BNCT in Taiwan.

The line U-87 GM, abbreviation for Uppsala 87 Malignant Glioma (U-87) was chosen because it represents one of the main reference models for the study of human GBM *in vitro*. The cells were initially isolated from a 44-year-old female glioma brain patient at the Uppsala University, Sweden, in 1966 [120]. Cell survival was evaluated under the effect of different types of radiation and for increasing dose. Adherent tumor cells at 60–80% confluence were irradiated with neutrons, and with neutrons after administration of the borated molecule Boronophenylalanine (BPA) at the TRIGA Mark II research reactor, LENA laboratory, Pavia University, Italy. The reference curve is obtained by photon irradiation. In the next Chapter, the methods, the issues connected to the selection of a proper reference radiation source, and the dose-survival curves obtained are described. It will be highlighted the importance of using a relevant preclinical model to obtain significant isoeffective dose values in GBM. Chapther II.3 will describe the calculation of such dose in a real clinical example, to show the impact of the experimental and theoretical work in practical implementation.
The U-87 cell cultures were irradiated using three radiation modalities: photons, neutrons, and neutrons combined with boron. For the photon irradiation experiments, two different sources were employed to assess the potential impact of photon energy: a low-energy X-ray irradiator (with an average energy of 60-80 keV) and a Co-60 source, whose energy spectrum is more similar to that of conventional radiotherapy. The experimental data obtained were subsequently analyzed to extract the radiobiological parameters required for the photon isoeffective dosimetric model.

II.1.1 Neutron irradiation

Dattoli Viegas et. al [121] demonstrated the importance of calculating detailed dosimetry in radiobiological experiments. The authors showed that assuming charged particles equilibrium (CPE) conditions leads to a misinterpretation of survival data, which subsequently propagates to the patient dose calculation. There-

fore, the detailed dosimetry obtained through Monte Carlo calculations reported in the cited article was extended in this work also to the photon component.
Neutron irradiation for measuring cell survival was performed in the thermal column of the TRIGA Mark II reactor (Pavia). The facility provides a thermal neutron field with low epithermal and fast neutron components and low gamma contamination [122]. For irradiation in presence of boron (*BPA-BNCT*), cells were incubated 48 hours before irradiation in T-75 flasks with 10 ml of culture medium enriched by the BPA for 4 hours. Subsequently, they were washed three times with Phosphate Buffered Saline (PBS) and fresh culture medium was supplied, to study the effect of the boron absorbed by the cells.
The dose component due to neutron capture in boron depends on ^{10}B concentration internalized by the cells. For this reason, a flask of cells treated as those exposed to the neutron beam was prepared for boron concentration measurement by neutron autoradiography [123]. Dose was calculated as described in [121].
The dose was escalated by varying the reactor power (7.5 kW, 30 kW, 100 kW and 250 kW), and the irradiation time was fixed to 10 minutes, to minimize the time the cells remain outside the incubator. The cell survival was evaluated via the clonogenic assay [124, 121]. Cultures of U-87 cells administered with BPA at the same conditions as mentioned above were prepared to verify that it does not affect the survival. Results showed that the survival of BPA-supplemented cells is not different that the control one, demonstrating the fact that BPA alone is not toxic at these concentrations.
For survival curves without BPA administration (*beam-only*), cells were prepared as described above and again the clonogenic test was performed to evaluate the percentage of cells that survived the irradiation.

II.1.2 Photon irradiation

For photon irradiation, cells were prepared as for neutron irradiation, using T-25 flasks.

X ray irradiation

The first set of photon irradiation took place at the San Matteo Polyclinic in Pavia, using a Best^{TM} Theratronics irradiator (Raycell® Mk2 X-ray blood irradiator), commonly used to sterilize blood bags for transfusions. This device consists of a lead-shielded chamber containing two opposing 160 kVp X-ray sources (average X-ray energy 60-80 keV). The facility has a removable drawer housing a stand in which samples are placed and irradiated. The drawer contains a PMMA tissue-equivalent phantom with housings for small samples irradiation and for the calibration detector. The calibration of the set-up had been obtained with an ionization chamber positioned in the middle of the PMMA phantom, in CPE conditions. However, the cell cultures had to be positioned on the top of the phantom, as the detector housing was too small to host the flasks. This could impair

the CPE conditions and the nominal dose [125], as the position of the flask was closer to one of the two X-ray beams and without phantom on the top. To evaluate the impact of this, a simplified Monte Carlo model was built with the code MCNP6.1 [126], representing the drawer with lead walls, the PMMA phantom, the housing for the detector, the flask and the two opposite X-ray beams. The cells were modeled as a 10 μm thick layer of soft tissue (Figure II.1.1). Two simulations were carried out: one calculating KERMA (F6-type tally) and dose (+F8-type tally for electrons divided by mass) in the detector position, and the other calculating KERMA and dose in the cell monolayer. The ratio of the values obtained at the detector position and in the cells allowed a proper correction of the nominal dose values. The statistical error associated to the Monte Carlo results was below 1%.

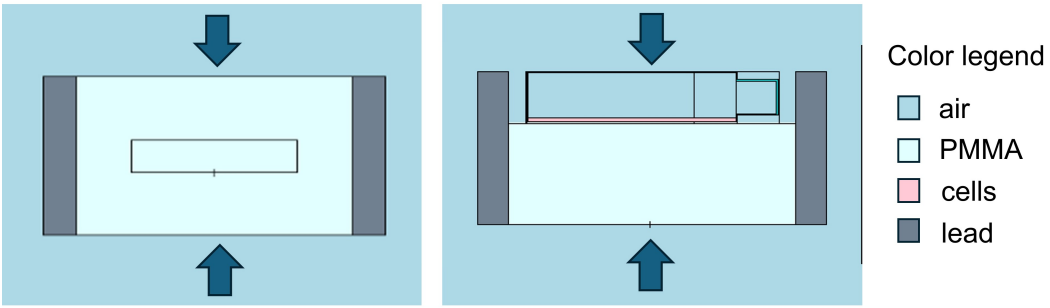

Figure II.1.1: *Model of the 160 kVp X-ray irradiator set-up. The sample into the tissue-equivalent material (polymethylmethacrylate - PMMA) is irradiated from the top and the bottom by two X-ray beams of average energy 60-80 keV (arrows). Left: the central rectangle represents the calibration position, where the detector is irradiated in CPE conditions. Right: The upper part of the phantom is removed, and the flask is irradiated in the upper part of the drawer.*

The results showed that: 1. KERMA and dose have the same value in the detector position, as expected; 2. in the cell layer, KERMA and dose differ by 9%; 3. the total correction taking into account the lack of CPE and the distance from the calibration position is 16%. This correction was thus applied to the nominal dose when building the dose-survival curve.

Cobalt-60 photon irradiation

The second set of photon irradiation was carried out at the LENA laboratory, at the Co-60 facility. Five flasks containing the U-87 cell line in adhesion were irradiated simultaneously within a dedicated well surrounded by 13 cobalt rods. The ^{60}Co decays into ^{60}Ni with a half-life of 5.3 years, emitting two photons of energy 1.1732 MeV and 1.3325 MeV. The dose rate was about 1 Gy/min, determined by previous calibration with an ionization chamber and alanine dosimeters.
T-25 flasks were inserted vertically into the photon field and extracted after different time intervals to deliver five different dose values, assuming CPE conditions in

the cells. To guarantee the equilibrium, flasks were completely filled with culture medium and a dummy water-filled flask was used to occupy the empty space into the holder. The assumption of CPE was studied in detail with a dedicated Monte Carlo simulation using the radiation transport code MCNP6.1 reproducing the irradiation set-up with the flask inserted, and the photon source distribution [127]. Figure II.1.2 shows a vertical section of the set-up, where the flasks are represented in orange, and a horizontal view where the rods emitting photons are represented in yellow.

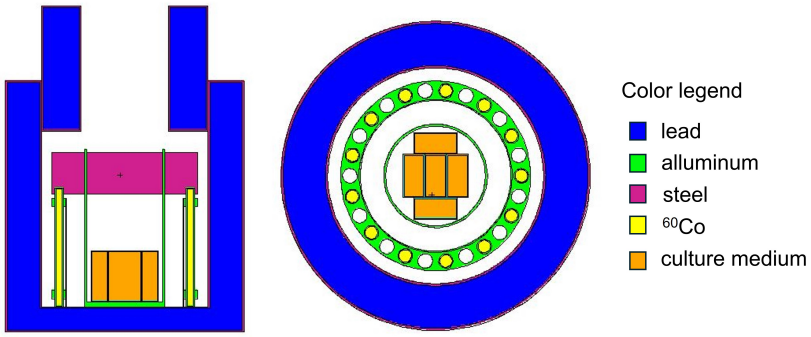

Figure II.1.2: *Left: vertical section of the facility for Co-60 irradiation. Right: horizontal section of the facility.*

As before, dose was calculated in the 10 μm cell layer, both assuming CPE (F6-type tally) and with detailed transport of the secondary electrons (F8*-type tally divided by cell mass). The statistical error associated to the Monte Carlo results was below 1%. In this case, the two values obtained were compatible, confirming the CPE condition and allowing for the use of nominal dose absorbed by cells.

II.1.3 Radiobiological survival curves

The probability of cell survival were fitted using the linear–quadratic (LQ) model. This choice is supported by previous studies showing that the LQ formalism provides an adequate description of the survival response of U-87 cells irradiated with photons [128, 129]. Therefore, the cell survival as a function of the dose was fitted using the model proposed by González & Santa Cruz in [38] and described in Subsection I.3.2.1. According to Eq. I.3.14, the cell survival probability for the reference radiation can be expressed as

$$S_R = \exp\left[-(\alpha_R D_R + \beta_R G_R(\theta) D_R^2)\right]. \tag{II.1.1}$$

It is important to note that fast neutrons present in BNCT beams have energies predominantly below 1 MeV. At these energies, elastic scattering with hydrogen atoms is the main contributor to the charged particle slowing-down spectrum, producing recoil protons with energies comparable to those produced by the capture of thermal neutrons in nitrogen nuclei. As a result, biological systems are

expected to exhibit similar responses when exposed to radiation with comparable lineal energy spectra. Therefore, the α and β parameters for fast neutrons can be assumed to be equal to those of thermal neutrons

$$\alpha_{n_{nt}} = \alpha_{n_f} = \alpha_n,$$
$$\beta_{n_{nt}} = \beta_{n_f} = \beta_n.$$

Under this assumption, the BNCT survival probability from Eq. I.3.19 can be rewritten by Eq. II.1.2.

$$\begin{aligned} S_{BNCT} = exp[-(&\alpha_B D_B + \alpha_n D_n + \alpha_\gamma D_\gamma + G_B\beta_B D_B^2 + G_n\beta_n D_n^2 + G_\gamma\beta_\gamma D_\gamma^2 \\ &+ 2G_{Bn}\sqrt{\beta_B\beta_n}D_B D_n + 2G_{B\gamma}\sqrt{\beta_B\beta_\gamma}D_B D_\gamma + 2G_{\gamma n}\sqrt{\beta_\gamma\beta_n}D_\gamma D_n)], \end{aligned} \tag{II.1.2}$$

where α_i and β_i with B=boron, n=neutrons and γ=photons, are the radiobiological parameters of the different radiation components of BNCT. The model takes into account the first-order repair of sub-lethal damage (SLD) employing the Lea-Catcheside temporal G-factors (from Eq I.3.5) and the synergism between the different radiation components through the quadratic mixed dose terms.
The Equation II.1.1 was used to fit the experimental data obtained from photon irradiation, thus deriving the radiobiological coefficients α_R and β_R specific to the U-87 cell line. The alpha and beta parameters of the gamma component of the BNCT dose can be assumed to be equal to those of the reference radiation (as anticipated before, this is especially true when the reference radiation source is Co-60). In this case, the following equivalences hold:

$$\begin{aligned} \alpha_R &= \alpha_\gamma, \\ \beta_R &= \beta_\gamma. \end{aligned} \tag{II.1.3}$$

Once the radiobiological coefficients for the gamma component had been obtained, the cell survival model described in Equation II.1.2 was used to calculate the remaining radiobiological parameters. For the boron component, which corresponds to high-LET radiation, the contribution of the quadratic term was found to be negligible for the U-87 cell line. Therefore, in this case, the β_B parameter was considered virtually zero, and the quadratic term was omitted by setting $\beta_B = 0$.
The G factors for each dose point remain the same when the dose increases because irradiation is performed at a fixed time. The kinetic repair time was obtained using experimental data published in [128], consisting in the normalized number of foci/nuclei at different time intervals after 2 Gy/min photon irradiation for U-87 cell line. For a quantitative description of the progress of DNA damage reduction, the authors of the cited paper proposed a mono-exponential fit. However, a bi-exponential equation (Eq. II.1.4) with a fast (t_{0f}) and a slow (t_{0s}) component better fits the data, c being the proportion that repairs with the fast kinetics. Thus, this fit is used instead, which allows separating two populations with different repair kinetics. Figure II.1.3 shows the fitted curve.

$$I(t) = ce^{-(1/t_{0f}))t} + (1-c)e^{-(1/t_{0s})t}. \tag{II.1.4}$$

As a result of the fit, the two characteristic repair times and the percentage of SLD repair for low LET radiation are obtained. The values of the percentage of SLD repair for high LET radiation were taken from [130]. Based on what is described in [130], the repair times for high LET radiation are assumed to be the same as for the low LET radiation.
Table II.1.1 summarizes the results that are obtained for the U-87 cell line along with the relative percentage of cells repaired by fast and slow kinetics for both photon and high-LET radiation. Uncertainties correspond to a 68% confidence level.

		SLD repair [%]	
	Characteristic repair times	Low LET	High LET*
t_{0f}	91±45 min	0.77±0.54†	0.2
t_{0s}	1238±1237 min	0.23±0.54	0.8

Table II.1.1: *Values of the characteristic repair times and the corresponding percentage of SLD repair. Uncertainties correspond to a 68% confidence level. †Constant c in Eq. II.1.4. *Data taken from [130].*

As extensively presented in Chapter I.3, the Isoeffective Dose, i.e. the photon dose that produces the same level of effect (cell survival) as the four dose components of the BNCT, $S_R(D) = S_{BNCT}(D_i)$ with $i = 1, 2, 3, 4$, is given by equation I.3.21. In particular, under the above considerations, the four dose components are reduced to three so the D_i now refers to $i = B, n, \gamma$. The final expression for the photon isoeffective dose is thus

$$D_R = \frac{-\alpha_R + \sqrt{\alpha_R^2 + 4\beta_R(\alpha_B D_B + \alpha_n D_n + \alpha_\gamma D_\gamma + G_B\beta_B D_B^2 + G_n\beta_n D_n^2 + MQ)}}{2\beta_R G_R} \tag{II.1.5}$$

with

$$MQ = G_\gamma\beta_\gamma D_\gamma^2 + 2G_{Bn}\sqrt{\beta_B\beta_n}D_B D_n + 2G_{B\gamma}\sqrt{\beta_B\beta_\gamma}D_B D_\gamma + 2G_{\gamma n}\sqrt{\beta_\gamma\beta_n}D_\gamma D_n. \tag{II.1.6}$$

This chapter presented the radiobiological experiments, along with the methodology adopted to analyze the survival data of U-87 cells subjected to three irradiation conditions: photons, neutrons, and neutrons in combination with boron. The characteristic repair times necessary for the description of the factor G were also determined, and the assumptions required to perform the fit were discussed. In the next chapter, a comparison of the two photon sources (X-rays and Co-60) will be made, followed by the application of the survival model to derive the radiobiological parameters needed for the dosimetry model described in Section I.3.2.

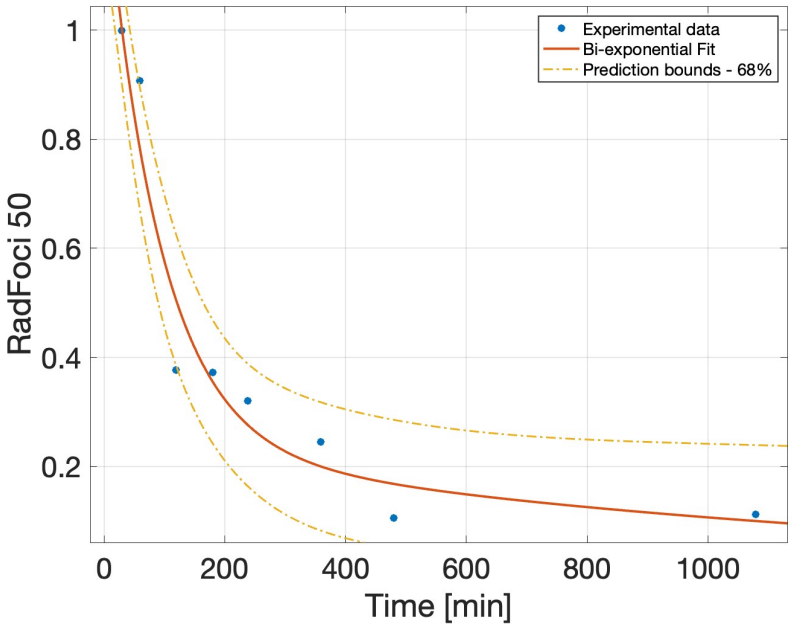

Figure II.1.3: *Kinetic repair time data (dots) from [128] and bi-exponential fit (solid line). The dash-dotted lines represent the upper and lower bounds of the 68% confidence interval. The dash-dotted orange lines represent the upper and lower bounds of the 68% confidence interval. The fit has a Mean Squared Error (MSE) of 0.86.*

CHAPTER II.2

PHOTON ISOEFFECTIVE DOSE MODEL FOR GLIOBLASTOMA MULTIFORME

II.2.0.1 The photon reference radiation

To assess the impact of using different types of reference radiation, radiobiological parameters were obtained by considering the photons emitted by cobalt-60 and orthovoltage X-rays (e.g., 160 kVp). Figure II.2.1 shows the two curves. The error bars of the experimental data represent the uncertainty in the counting of the colonies. Table II.2.1 reports the parameters obtained from the fitting using the Modified Linear Quadratic (MLQ) model (Equation (II.1.1)).

	^{60}Co	**160 kVp X-Ray**
α_γ $[Gy^{-1}]$	0.21 ± 0.08	0.46 ± 0.09
β_γ $[Gy^{-2}]$	0.02 ± 0.01	0.03 ± 0.04

Table II.2.1: *Radiobiological parameters α and β obtained by fitting the cell survival curves for the two reference radiations. Errors correspond to 68% confidence intervals..*

Figure II.2.1 shows that the two curves differ significantly. A measure to quantify this difference is the RBE for a given endpoint, taking X- rays as the test radiation and gamma rays as the reference. The RBE for a survival fraction of 0.01 is 1.5. The fact that the biological effectiveness of X-rays is higher than that of gamma rays has been observed before, see for example [131]. The choice of a reference radiation impacts on the RBE and CBE factors for BNCT for a specific endpoint, and consequently also affects the photon isoeffective dose. Therefore, it is important to select a reference radiation as similar as possible to the clinical conventional photon beam. This ensures that the Photon Isoeffective Dose accurately represents

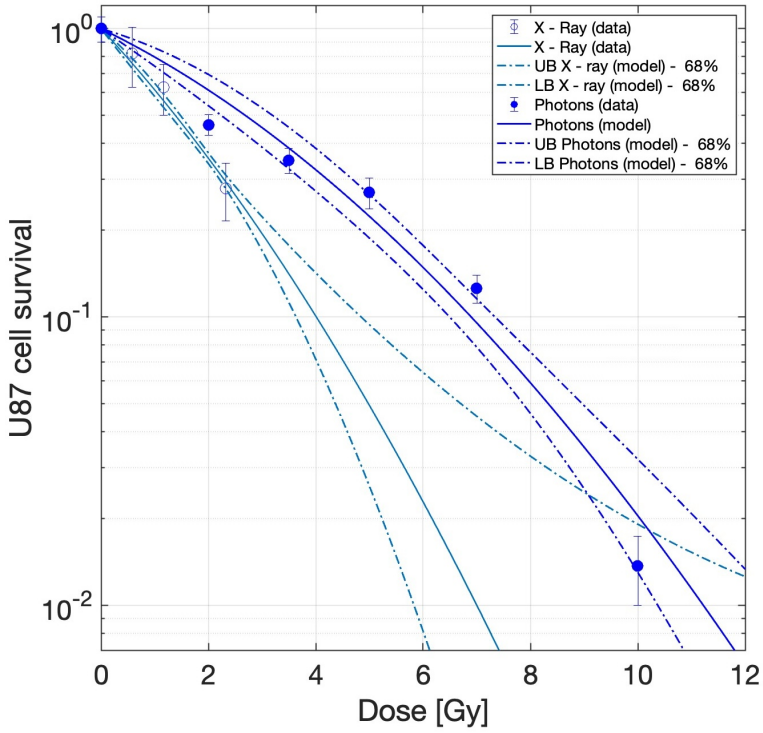

Figure II.2.1: *Experimental data and fit of U-87 cell survival as a function of the dose of photons emitted by ^{60}Co (solid line) and 160 kVp X-Rays (dashed line). The dashed-dotted lines indicate the upper (UB) and lower (LB) bounds, represent the confidence intervals of the parameters obtained from the fit of the two curves.*

the biological effect of photon radiotherapy and remains meaningful for BNCT treatment planning. Moreover, one of the underlying assumptions of the Photon Isoeffective Dose model is that the radiobiological parameters of the reference radiation can be used to describe the photon component of the BNCT mixed field, primarily the 2.2 MeV gamma rays resulting from neutron capture in hydrogen. Consequently, a reference radiation closely matching this photon component is preferable.

II.2.0.2 Beam-only and BPA-BNCT radiobiological parameters

The beam-only and BPA-BNCT curves were simultaneously fitted with the modified LQ model (Equation II.1.2) considering the X-rays or the ^{60}Co gamma radiation as the reference. The fitted curves are reported in Figure II.2.2. The horizontal error bars for the doses are dominated by the uncertainty in boron concentration measurements. The fit procedure was error-weighted.
Table II.2.2 reports the radiobiological parameters resulting from the fit for beam-only and BPA-BNCT in the U-87 cell line, for both ^{60}Co and 160 kVp X-ray refe-

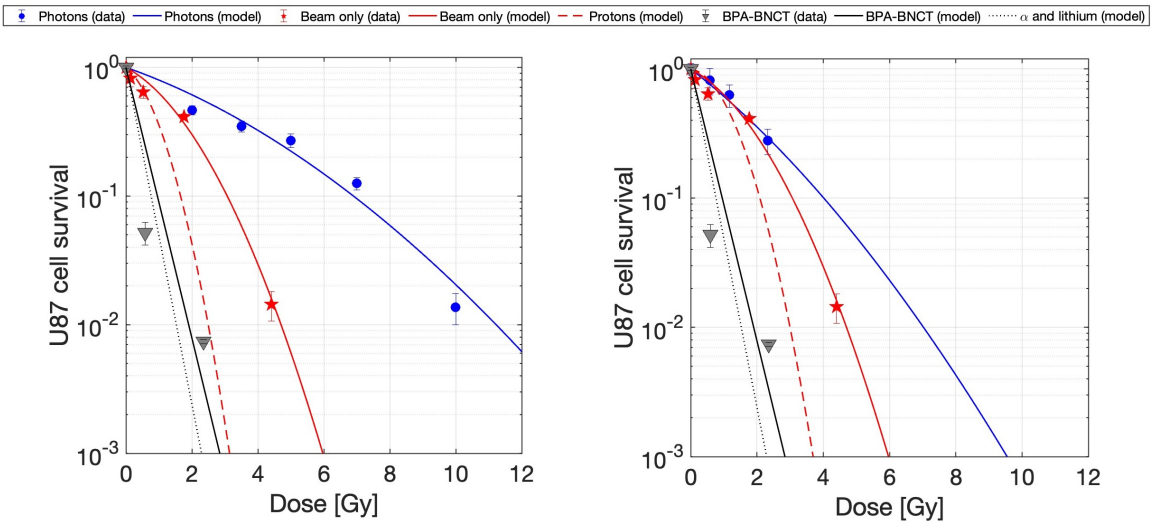

Figure II.2.2: *Survival curves of U-87 cells vs. absorbed dose. Left: ^{60}Co reference radiation. Right: X-rays. Blue: reference radiation (dots: data, line: fit). Red: beam-only irradiation (stars: data, solid line: fit; dashed line: isolated proton contribution). Black: BPA-BNCT (triangles: data, solid line: fit; dotted line: boron-only contribution).*

rence irradiation.

Radiobiological parameters for GBM				
	Photons from ^{60}Co		***Photons from 160 kVp X-Ray***	
	Neutrons	*Boron*	*Neutrons*	*Boron*
$\alpha\ [Gy^{-1}]$	0.5±0.9	3.0±0.6	0.1±0.9	3.0±0.6
$\beta\ [Gy^{-2}]$	0.5±0.6	0	0.5±0.6	0

Table II.2.2: *Radiobiological parameters for GBM, obtained from the fit of the cell survival curves as a function of dose for beam-only and BPA-BNCT irradiation, using ^{60}Co and X-Ray as the radiation reference. Uncertainties correspond to a 68% confidence level.*

Given the different radiobiological parameters derived from the curves, the RBE and CBE factors vary accordingly. Table II.2.3 lists the values of RBE and CBE factors calculated for 1% of survival with the curves that have the isolated p+ ^{14}C and α+^{7}Li contributions (dashed red line and dotted black lines in Fig. II.2.2 respectively). Moreover, it reports the values taken from [132], typically used in BNCT clinical applications.

The results clearly show that the reference radiation used has an appreciable impact on the RBE/CBE factors, which relate the biological effectiveness of other radiation types to photons (Table II.2.4). Furthermore, compared with those used in BNCT clinic, obtained for gliosarcoma with 250 kVp X-ray photons (effective energy ≈ 90 keV), the results obtained in this work are significantly different. The

	^{60}Co	X-Ray	Clinic
RBE	4.8 ± 0.7	2.5 ± 1.4	3.2
CBE	7.5 ± 0.9	4.7 ± 1.5	3.8

Table II.2.3: *$RBE_{1\%}$ and $CBE_{1\%}$ values, calculated for each reference radiation, and those used in the clinic. The errors associated is the propagation of the uncertainties of the fit parameters.*

Relative differences [%]			
	^{60}Co vs. X-Ray	*^{60}Co vs. Clinic*	*X-Ray vs. Clinic*
RBE	44	29	29
CBE	37	49	19

Table II.2.4: *Relative percentage differences in RBE and CBE values, comparing the two reference radiations (^{60}Co and 160 kVp X-Ray) and each photon sources with the values used in clinic practice.*

choice of the reference radiation thus plays a significant role in the translation of BNCT dose into photon equivalent units. Considering that the photon isoeffective dose is calculated to predict a clinical outcome based on the experience gained in conventional radiotherapy, we used ^{60}Co as the reference radiation for the in-patient dosimetry.
The overall set of radiobiological parameters for the photon isoeffective dose model optimized for GBM is summarized in Table II.2.5. These are the parameters to be inserted into Equation II.1.5. A brief summary table of the obtained radiobiological parameters (α, β, repair terms, synergy terms, CBE values, and corrected CBE values) is reported in Appendix B.

Radiobiological parameters for GBM			
	Photon	**Neutron**	**Boron**
$\alpha\ [Gy^{-1}]$	0.21±0.08	0.5±0.9	3.0±0.6
$\beta\ [Gy^{-2}]$	0.02±0.01	0.5±0.6	0

Table II.2.5: *Radiobiological parameters for GBM. Uncertainties correspond to a 68% confidence level.*

It is important to clarify that the presence of data points outside the prediction bounds for each interpolated model does not imply a systematic deviation (see Fig. II.2.3). The prediction limits of the interpolated model represent the uncertainty in the predicted values of the function, not the uncertainty of new observations. Therefore, the magnitude of these limits reflects our confidence in the interpolation itself, rather than the dispersion of individual data points. For example, if we calculate the prediction limits for a new observation (see the green lines in Fig. II.2.3) at the photon dose $D = 2$ Gy (where one data point is outside the prediction limits of the interpolated model) the confidence interval for a new

observation of cell survival at this dose (i.e., $S = 0.46$ with $\mathrm{CI}_{68\%} : [0.36, 1.1]$) contains the value predicted by the interpolated function and its range (i.e., $S = 0.61$ with $\mathrm{CI}_{68\%} : [0.54, 0.69]$). Thus, this demonstrates that although the data point is outside the prediction limits for the interpolated function, the fact that the confidence interval for a new observation contains that of the interpolated function confirms that the model remains consistent. The same is true for beam-only data and its interpolated model.

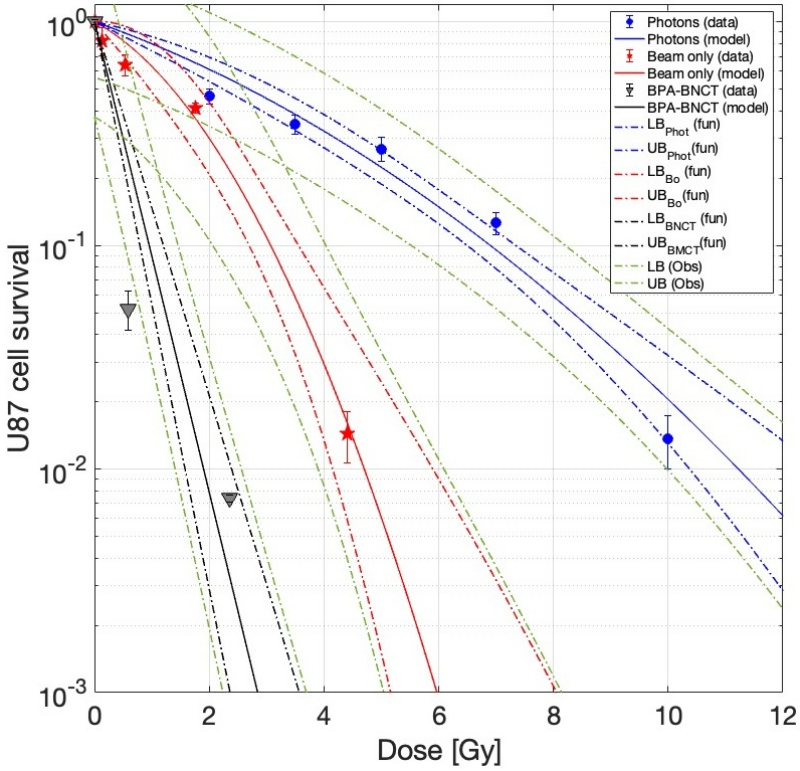

Figure II.2.3: *Survival curves of U-87 cells vs. absorbed dose. Blue: ^{60}Co reference radiation (dots: data, line: fit). Red: beam-only irradiation (stars: data, line: fit). Black: BPA-BNCT (triangles: data, line: fit). Dotted lines: 68% confidence level prediction bounds for each model (color-coded as above). Green dotted lines: upper/lower 68% confidence bounds for a new observation.*

CHAPTER II.3

IN-PATIENT DOSIMETRY

The simulation of the treatment planning was carried out using the IT_STARTS treatment planning system (TPS) [133]. This software was created in Pavia in the frame of the Istituto Nazionale Fisica Nucleare (INFN-Italy) homonymous project, in collaboration with the Computational Physics and Radiation Biophysics Division group at the Comisión Nacional de Energía Atómica (CNEA-Buenos Aires, Argentina). This tool is a system that takes the medical images of a patient and the Regions of Interest (ROIs), producing an input file for the Monte Carlo calculation of the dosimetry, including the neutron source and patient positioning. IT_STARTS then allows the computation of photon-equivalent dose by integrating the radiobiological data, the fit, the radiobiological parameters and the models. As the output, it delivers different Figures of Merit such as Dose Volume Histograms (DVH), isodose curves, Tumor Control Probability (TCP), Normal Tissue Complication Probability (NTCP) and others. IT_STARTS is written in Python [134], and the TPS code itself, will be soon made public through appropriate software-sharing methods to extend its use to different BNCT users [135].

As a relevant GBM patient example, the dosimetry calculation was obtained in a clinical case treated with BNCT with the epithermal neutron source of the Tsing-Hua Open-Pool Reactor (THOR) at National Tsing-Hua University [136], Taiwan. The use of a real patient instead of a general phantom allows working within a clinically relevant scenario, where the ROIs, the patient positioning, the boron concentration measured, the criteria for dose prescription are those applied in the real application. The Gross tumor Volume (GTV) ROI is shown in Figure II.3.1 overlaid on the CT scan of the GBM patient.

The patient received a continuous infusion of L-BPA for a total infused dose of 450 mg/kg body weight, divided into 180 mg/kg per hour for 2 h before BNCT, and 90 mg/kg per hour for drug concentration maintenance during the neutron irradiation process. Blood boron concentration was evaluated through inductively coupled plasma with atomic emission spectroscopy (ICP-AES) during the first and second hour of L-BPA infusion, and after the neutron irradiation. The boron con-

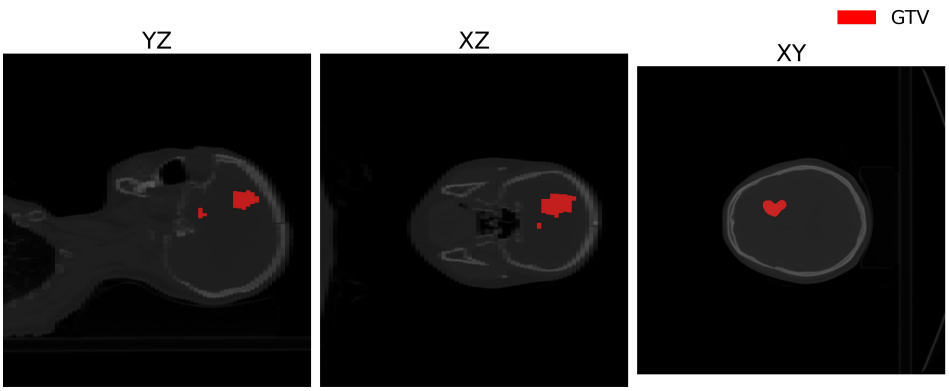

Figure II.3.1: *CT medical images of the patient (axial, coronal, sagittal) with the GTV ROI marked by the red area.*

centration during the second hour is also the boron concentration when the neutron irradiation begins [137]. The tumor-to-normal tissue boron concentration was calculated from the measured values in blood and using the results of a previous positron emission tomography (PET) scan.
Before the treatment, the patient underwent PET with 4-borono-2-18F-fluorophenylalanine (FBPA) at the Department of Nuclear Medicine of the Taiwan Veteran General Hospital, to evaluate the distribution of L-(4-10-borophenyl) alanine (L-BPA). The tumor-to-normal tissue ratio (T/N ratio) and the tumor-to-blood ratio (T/B ratio) were calculated employing the maximum standardized uptake value (SUV) of the brain and tumor. In this case the T/B ratio was 3.05 and the boron concentration was 40 ppm in tumor. Normal-brain to-blood ratio was 1.05 (13.6 ppm in brain).
The beam configuration was set to maximize the dose to the tumor, with the dose to the normal brain prescribed so that 50% of the volume received no more than 2.5 Gy (RBE), according to the RBE model described in Section I.3.1. For the calculations, RBE values of 1 for photons and 3.2 for neutrons were adopted, together with CBE factors of 3.8.
In Taiwan, dosimetry was calculated using fixed RBE values obtained by Coderre et al. [132] derived *in vivo - in vitro* using a rat model of gliosarcoma and for normal brain values taken from [132]. IT_STARTS software was used to reproduce the same treatment planning using the epithermal neutron beam of the INFN RFQ accelerator described in [138] as the neutron source. Once the geometry of the patient was obtained, the treatment room was simulated with the patient in the same position as the real treatment in Taiwan, considering that CPE conditions are satisfied [139] in the healthy brain and tumor. KERMA rates were calculated with MCNP F4-tally type using brain KERMA factors from ICRU 44 [140]. Four

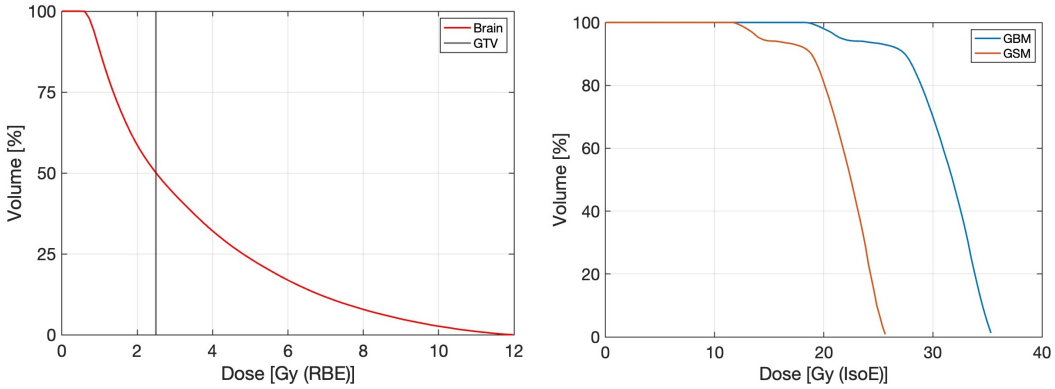

(a) **(b)**

Figure II.3.2: *a) Dose-Volume Histogram (DVH) of the healthy brain; the black vertical line highlights the prescription limit of* $2.5\ \mathrm{Gy(RBE)}$ *or less to 50% of the brain volume. b) DVH for the tumor (GTV) calculated using the photon isoeffective dose model with parameters derived from glioblastoma (Blue) and from gliosarcoma (Red).*

absorbed dose rate matrices are the output of the simulation, one for each BNCT dose component.
The dose prescription to healthy brain led to an irradiation time of 33.3 min using the RFQ neutron beam. The dose in normal brain was obtained using the radiobiological data from [132], to maintain the same dose prescription as in the original treatment. With this irradiation time, the photon isoeffective dose in the tumor was calculated with the radiobiological parameters derived from U-87 experiments (Table II.3.1) and the one from GSM. This comparison is meant to highlight the impact of using parameters coming from different tumor models in the calculation of photon-equivalent dose in patients.

Radiobiological parameters for GSM			
	Neutrons	*Boron*	*Photons*
$\alpha\ [Gy^{-1}]$	0.4972	0.9091	0.2008
$\beta\ [Gy^{-2}]$	0.088	0.0019	0.0078

Table II.3.1: *Radiobiological parameters for GSM.*

Figure II.3.2 shows the DVH of the healthy brain in the left panel. The black vertical line represents the limiting RBE-weighted dose for the organ at risk, as defined by the Taiwan protocol. The right panel depicts the DVH of the Gross Tumor Volume (GTV), calculated using the Photon Isoeffective Dose Model (Eq.II.1.5). The red curve corresponds to the radiobiological parameters from the rat gliosarcoma experiments, while the blue curve corresponds to those from the U-87 experiments described above (parameters for GBM in Table II.2.5).
Table II.3.2 reports the maximum, mean and minimum doses calculated using: (i) the RBE-weighted dose (with RBE values listed in Table II.2.3, i.e. the ^{60}Co-

derived RBE for GBM, the clinically adopted RBE for GSM), and (ii) the photon isoeffective dose model with radiobiological parameters derived from GBM II.2.2 and GSM (Table II.3.1) experiments.

	Gross Tumor Volume			
	Photon Isoeffective Model [Gy (IsoE)]		RBE-weighted Model [Gy (RBE)]	
	GSM	GBM	GSM	GBM
D_{max}	25.5	35.2	41.1	76.2
D_{mean}	22.5	31.8	34.6	63.4
D_{min}	13.0	20.0	16.4	29.5

Table II.3.2: *Maximum, mean and minimum dose values for the two dosimetric models considered (Photon Isoeffective and RBE-weighted), each fed with parameters from two different biological systems (GSM and GBM).*

Table II.3.3 shows the percentage relative differences in dose values for the RBE-weighted and isoeffective dose models, as listed in Table II.3.2, for GBM and GSM parameters.

	Photon Isoeffective Model	RBE - weighted Model
	GBM - GSM	GBM - GSM
Max	28 %	46 %
Mean	29 %	45 %
Min	35 %	44 %

Table II.3.3: *Percentage relative difference due to the set of radiobiological data used (GSM vs. GBM) in maximum, average and minimum dose values for the RBE-weighted model (second column) and for the isoeffective model (third column).*

The difference between the dose values obtained is significant, as reported in Table II.3.3. This shows that consistent radiobiological data should be available for each tumor. A similar trend was observed in the fixed-RBE model when using RBE and CBE values calculated with the two radiobiological datasets, see Table II.3.3. Regarding the difference between the RBE-weighted and the photon isoeffective dose model, it is confirmed what has been extensively shown in other works, i.e., tumor doses are overestimated when calculated with RBE-weighted model [38, 67, 141, 142]. The RBE-weighted tumor doses are significantly higher than the photon isoeffective dose values, especially as the total absorbed tumor dose increases. The overestimation of tumor dose has implications for clinical BNCT, as it influences the capacity to assess a proper dose-effect relationship, preventing the prediction of clinical outcomes based on the dose distribution calculated by treatment planning. If tumor dose was indeed that high, the prescription strategy could shift toward prescribing directly to the tumor rather than to normal tissues, even if

this involves the challenge of working with less uniform tumor dose distributions than in conventional radiotherapy. Moreover, when dose is artificially high, TCP models cannot be reliably used to predict the clinical results of a simulated irradiation, as the probability value would always saturate to 1. This has become evident in retrospective studies, since BNCT clinical outcomes do not match such high doses when compared with the experience of photon therapy. This suggests that the dose calculation models typically used to convert mixed-field radiation dose into photon equivalent units are not correct. In contrast, the photon isoeffective dose values calculated in this work are much more consistent with those delivered by single-fraction photon RT for the treatment of brain tumors [143], and analyzed GBM patients treated with stereotactic radiosurgery [144]. They showed that with a maximum single-fraction dose of 30±7 Gy and a margin dose of 15±3 Gy, the local control (complete response, partial response and stable disease) was 68%. On the other hand, BNCT GBM patients treated in Finland [145] showed a local control of 60% at the same follow-up time, with doses in the range 16-59 Gy-Eq, using the RBE-weighted dose model. The fact that RBE-weighted dose values are significantly higher than those in [144] for a similar clinical outcome reinforces the idea that the traditional model overestimates the tumor dose. In the patient analyzed, RBE-weighted doses are similar to what was calculated by Kankaanranta et al [145]. On the other hand, the photon isoeffective dose is consistent with photon therapy data in [144]. These findings strongly suggest that the isoeffective dose model is an adequate tool to calculate photon-equivalent doses.

Therefore, in principle, the availability of radiobiological parameters opens the possibility of exploring Tumor Control Probability (TCP) models, as commonly done in photon-based treatments, to prospectively assess the therapeutic potential of BNCT in GBM. However, as will be discussed in Chapter IV.1, the applicability of TCP modeling to GBM is highly questionable, and alternative clinical endpoints such as Progression-Free survival at 1 year may provide a more reliable basis for treatment evaluation.

Until now, the dose calculations in patients are performed assuming uniform boron distribution at the tissue and cell levels. However, tumors are composed of heterogeneous cell populations that may absorb different boron concentrations.

In [146], the Chinese BNCT group working at the clinical applications in Xiamen, describe how they incorporate a heterogeneous macroscopic distribution of boron-10 within the tumor for dose calculations. The term *macroscopic* refers to the spatial scale accessible to medical imaging (i.e., millimeter-to-centimeter resolution), as opposed to the microscopic or cellular level, which can only assessed *in vitro* or *ex-vivo*. Boron macroscopic distribution is achieved by using PET-derived standardized uptake values (SUVs) to map the spatial distribution of the boron-containing compound. The resulting distribution is then used as input for the treatment planning, allowing for a more accurate estimation of the boron dose across different tumor regions.

Photon isoeffective dose model could easily incorporate different boron concen-

trations at the tissue level, when the experimental information is available. The fact that boron may be non-uniform at the sub-cellular level (i.e. nucleus vs. cytoplasm), however, requires an extension of the model with a proper formalism which differentiate the dose deposition in the cells according to the microdistribution of boron.
In the next Part of this thesis, the impact of the microdistribution of boron-10 within tumor cells will be assessed, and this information will be incorporated into the formalism of the Photon Isoeffective Dose Model.

Part III

Unraveling the role of boron microdistribution in BNCT dosimetry of Glioblastoma Multiforme: a combined theoretical and experimental insights

CHAPTER III.1

MICRODOSIMETRY MATHEMATICAL MODEL

As anticipated in Chapter I.3, BNCT absorbed dose in tumors is conventionally estimated by computing the Kinetic Energy Released per unit MAss (KERMA). This approach assumes charged particle equilibrium and a homogeneous boron distribution across the tumor volume, both at the macroscopic and microscopic levels. However, this assumption is known to be inaccurate. At the macroscopic level, tumors are composed of heterogeneous cell populations with variable metabolic activity. Additionally, vascularization in solid tumors is often more pronounced at the periphery, leading to spatial variations in boron uptake [146]. At the subcellular level, different borated compounds exhibit varying capabilities to penetrate the cell membrane and the nucleus [147]. As a result, the biological effect of the same neutron fluence, and thus of the same average absorbed dose, can differ significantly depending on the proximity of boron to the DNA.

Building on the discussion in Chapter I.4, conventional dosimetry encounters great difficulties when attempting to understand the mechanisms of radiation action at the cellular or subcellular level. Radiation fields that may appear uniform at the tissue level may be completely heterogeneous at the cellular or subcellular level, bearing in mind that the diameter of a cell is approximately 10 μm. The fundamental difference between macroscopic absorbed dose and energy deposition in microscopic structures leads to microdosimetry.

Understanding the stochastic aspects of the energy deposition process by high-LET particles in microscopic volumes is essential for a comprehensive interpretation of biological effects. Average quantities such as dose alone cannot fully account for these effects, highlighting the need for microdosimetric approaches.

In this part, the present work addresses one of the limitations of standard KERMA-based calculations: the assumption of uniform boron distribution. If the actual boron microdistribution differs, this can result in substantial over- or underestimation of the absorbed dose delivered to sensitive targets, where the biological

effect is generated.

To improve the accuracy of dose–effect predictions, an enhanced model is proposed that integrates microdosimetry into the Photon Isoeffective Dose framework for GBM.

Building upon the macroscopic formulation described in the previous Part II, this approach incorporates the stochastic nature of energy deposition resulting from heterogeneous boron distribution at the cellular level. Specifically, the model describes the tumor as a densely packed ensemble of cells and considers two main subcellular compartments: the nucleus and cytoplasm. The boron concentration ratio between these compartments is treated as a stochastic variable, based on experimental distributions measured (see Section III.2).

In [78], Santa Cruz et al. proposed a method to calculate the dose assuming different boron concentrations inside and outside the site of interest. Considering the nucleus as the site of interest, it is possible to calculate a correction factor to the uniform-based boron dose as a function of the nucleus-cytoplasm boron ratio, a.

The KERMA factor of the i^{th} particle produced during the boron neutron capture can be expressed according to Eq. III.1.1

$$K_{\phi}^{i} = N\bar{\epsilon_i}\frac{\sigma_i^{prod}}{M_A}, \tag{III.1.1}$$

where σ_i^{prod} [cm^2] is the production cross section of the ejectile i, $\bar{\epsilon_i}$ [MeV] is the average energy of the ejectile, M_A [g·mol^{-1}] is the target atomic mass and N is a constant factor. These factors depend on the neutron energy, so they are integrated with the neutron fluence for all particles released during the reaction, multiplied by the isotropic mass fraction of the target nuclei in the material, and then summed to obtain the KERMA.

Integrating Eq. III.1.1 with the neutron flux, results in an equivalent expression (Eq. III.1.2), for calculating the dose rate for a given reaction,

$$\dot{D} = \frac{\bar{\epsilon}\dot{r}}{\rho}, \tag{III.1.2}$$

where $\dot{r}$ [s^{-1}·cm^{-3}] is the reaction rate per unit of volume, $\bar{\epsilon}$ [MeV] is the total average energy released by charged particles per reaction, and ρ [g·cm^{-3}] is the material density.

Under charged particle equilibrium conditions (CPE)[1], for thermal neutron capture reaction in boron, the reaction rate can be calculated according to Eq III.1.3,

$$\dot{r} = \frac{\rho\, C_{^{10}B} N_A \Phi_{th} \sigma_{th}}{M_{^{10}B}}, \tag{III.1.3}$$

[1] In a given volume, the energy transported by the incoming charged particles is equal to that transported by the outgoing particles.

where Φ_{th} [$cm^{-2}{\cdot}s^{-1}$] is the thermal neutron flux, σ_{th} [cm^2] is the ^{10}B thermal neutron capture cross section, $C_{^{10}B}$ [ppm] is the boron concentration, N_A [mol^{-1}] is Avogadro's number and $M_{^{10}B}$ [$g{\cdot}mol^{-1}$] is the atomic mass of ^{10}B.
Considering the case where the source of charged particles is located exclusively inside a microscopic site, the average dose rate can be calculated as

$$\dot{D}_I(\dot{r}) = \dot{r} V_S z_F^I, \tag{III.1.4}$$

with V_S [cm^3] the site volume and z_F^I [Gy] the frequency mean specific energy per intrasite reactions, that can be expressed as Eq. III.1.5 from z_F in Eq. I.4.5.

$$z_F^I = \int_0^\infty z f_1^I(z) dz. \tag{III.1.5}$$

The quantity $\rho V_S z_F^I$ represents the average energy deposited in the volume per reaction occurring inside the site. Therefore, its value is lower than the total average energy of the reaction $\bar{\epsilon}$.
The average dose rate in a site can be expressed, by means of the principle of superposition of sources, as the contribution of external reactions that deposit energy in the site plus the contribution of the internal sources. If the reaction rate is the same outside and inside the site, then it is possible to express the average dose rate for an extrasite distribution as the difference between the dose rate produced by a uniform distribution and that of an internal distribution: $\dot{D}_O = \dot{D}_U - \dot{D}_I$.
Let be the case where the rates of reaction are different inside $\dot{r}_I$ and outside $\dot{r}_O$ the site of interest. When applying the principle of superposition of sources, the problem can be viewed as a contribution of a uniform source plus a component due to the inside source if $\dot{r}_I > \dot{r}_O$ or outside when $\dot{r}_I < \dot{r}_O$.
Considering the nucleus as the site of interest, it is possible to calculate a correction factor to the macroscopic uniform-based boron dose as a function of the nucleus-cytoplasm boron reaction rate ratio, a. If the densities of the nucleus and the cytoplasm are the same ($\rho_n = \rho_c$), a coincides with the quotient of ^{10}B concentrations.
Finally, the average dose rate for a non-equilibrium situation can be written as

$$\dot{D}(\dot{r}_O, \dot{r}_I) = \dot{D}_U(\dot{r}_O)[1 + (a-1)\rho V_S \frac{z_F^I}{\bar{\epsilon}}] \tag{III.1.6}$$

$$= \eta(a) \dot{D}_U(\dot{r}_O). \tag{III.1.7}$$

The Microscopic Dose Correction Factor, MDCF, that corrects the macroscopic boron dose, is expressed as [78]

$$\eta(a) = 1 + (a-1)\rho V_S \frac{z_F^I}{\bar{\epsilon}}. \tag{III.1.8}$$

The boron KERMA is calculated assuming the boron-10 uniform and equal to the minimum reaction rate. By defining $c = \rho V_S \frac{z_F^I}{\bar{\epsilon}}$ it is now possible to simplify the expression of MDCF, $\eta(a)$ (Eq. III.1.8), as follows

$$\eta(a) = 1 + (a-1) \cdot c. \tag{III.1.9}$$

The correction factor can be used to correct the boron absorbed dose in BNCT, assuming that the cells are distributed as an orderly, closely packed collection of cells. The total BNCT absorbed dose administered consists of a boron-dependent (D_B), and a non-boron-dependent component ($D_{B_{ind}}$), as in Eq. III.1.10.

$$D_{BNCT-absorbed} = D_B + D_{B_{ind}}. \tag{III.1.10}$$

The MDFC, $\eta(a)$, is only applied to the boron-dependent component, while the other remains unchanged.
Assuming that the above-mentioned nucleus-cytoplasm boron reaction rate ratio a is a random variable with a probability density $f_A(a)$, the MDCF is also a random variable, as is the boron dose. Consequently, the expected value of the total BNCT absorbed dose is given by

$$\mathbb{E}[D_{BNCT-absorbed}] = \int_0^{+\infty} (\eta(a) \cdot D_B + D_{B_{ind}}) \cdot f_A(a) \cdot da \tag{III.1.11}$$

$$= D_{B_{ind}} + \int_0^{+\infty} \eta(a) \cdot D_B \cdot f_A(a) \cdot da. \tag{III.1.12}$$

The boron dose is directly dependent on ^{10}B concentration. In particular, to obtain an accurate estimation that considers microdosimetric aspects, it is necessary to apply the MDCF. The dose is calculated assuming a uniform boron distribution, with a concentration equal to that in the cytoplasm. Consequently, the boron dose can be expressed as a function of the cytoplasm concentration:

$$D_B = D_B(B_{cyto}) = K_{B-cyto} \cdot B_{cyto}, \tag{III.1.13}$$

where K_{B-cyto} is the KERMA of the boron component per unit concentration $\left[\frac{\text{Gy}}{\text{ppm}}\right]$.
The average boron concentration in the cell (B_{cell}) can be expressed as a weighted combination of the concentrations in the nucleus (B_{nuc}) and in the cytoplasm (B_{cyto}), with weights corresponding to the volume fractions occupied by these two regions within the cell

$$B_{cell} = B_{nuc} \cdot v + B_{cyto} \cdot (1 - v), \tag{III.1.14}$$

where v is the ratio of the volume of the nucleus (V_{nuc}) to the total volume of the cell ($V_{nuc} + V_{cito}$), defined as

$$v = \frac{V_{nuc}}{V_{nuc} + V_{cito}}. \tag{III.1.15}$$

This equation reflects that the average boron concentration in a cell results from the weighted average of the concentrations in the nucleus and cytoplasm, where the weights are given by their respective volume fractions. In other words, if v is small (so the nucleus occupies a small fraction of the cell), the average concentration will be closer to that of the cytoplasm. Conversely, if v is large (i.e., the nucleus occupies a significant portion of the cell), the nuclear concentration will influence the average boron concentration.

Starting from the equation of the average boron concentration in the cell, Eq. III.1.14 and using the relation $B_{nuc} = a \cdot B_{cyto}$, it is possible to replace B_{nuc} in the equation and obtain

$$B_{cell} = B_{cyto} \cdot (1 + v \cdot (a - 1)). \tag{III.1.16}$$

From Eq III.1.16, it is possible to isolate B_{cyto} and obtain

$$B_{cyto} = \frac{B_{cell}}{1 + v \cdot (a - 1)}. \tag{III.1.17}$$

This expression shows that the boron concentration in the cytoplasm depends only on the average boron concentration in cell, B_{cell}, the nucleus-to-cell volume fraction, v, and the random variable a.
Given the above considerations, the boron concentration, which depends on the random variable a, is also a random variable. As a result, the dose component related to boron exhibits random behavior as well. Therefore, equation III.1.12 can be rewritten as

$$\mathbb{E}[D_{BNCT-absorbed}] = D_{B_{ind}} + \int_0^{+\infty} \eta(a) \cdot K_{B-cyto} \cdot B_{cyto}(a) \cdot f_A(a) \cdot da. \tag{III.1.18}$$

By utilizing equations III.1.17 and III.1.13, Eq III.1.18 can be further expressed as

$$\mathbb{E}[D_{BNCT-absorbed}] = D_{B_{ind}} + K_{B-cyto} \cdot B_{cell} \int_0^{+\infty} \frac{1 + (a - 1) \cdot c}{1 + (a - 1) \cdot v} \cdot f_A(a) \cdot da. \tag{III.1.19}$$

The fraction within the integral represents a microdosimetric correction factor reflecting the stochastic effects of heterogeneous boron distribution between the nucleus and cytoplasm at the subcellular level. This fraction is defined as the new correction factor

$$\eta'(a) = \frac{1 + (a - 1) \cdot c}{1 + (a - 1) \cdot v} \tag{III.1.20}$$

which, within the integral in (III.1.19), incorporates both the effects of boron microdistribution and the variability in the nucleus-to-cytoplasm boron concentration ratio. Consequently, the expected value of the total BNCT absorbed dose in equation III.1.19 that explicitly accounts for these effects can be rewritten in a more compact form

$$\mathbb{E}[D_{BNCT-absorbed}] = D_{B_{ind}} + K_{B-cyto} \cdot B_{cell} \int_0^{+\infty} \eta'(a) \cdot f_A(a) \cdot da. \tag{III.1.21}$$

Section I.3.2 describes the Photon Isoeffective Dose Model that allows to calculate the dose for patients in photon equivalent units. Here, the expression in Eq. II.1.5 will be considered, where α_i and β_i (with $i = n, \gamma, B$) are the radiobiological parameters obtained from cell survival experiments. Therefore, if in the radiological experiment the absorbed dose used for cell survival analysis is calculated according to Eq. III.1.21, the resulting radiological parameters will correctly account for the effects mentioned and can be used consistently in the isoeffective dose model

for GBM. Specifically, D_B in Eq. II.1.5 represents the boron dose calculated by assuming a boron concentration in tumor equal to the macroscopic value. This is usually estimated as the boron concentration measured in blood during treatment, multiplied by a factor of 3.5 [148]. Following the same reasoning as for the total BNCT absorbed dose, D_B becomes a function of a as in the equation III.1.21. Consenquently, the Photon Isoeffective Dose Model that integrates the stochastic aspects of energy deposition related to the non-uniformity of boron concentration at the subcellular level and considers the nucleus-cytoplasm boron ratio as a stochastic variable, is

$$\mathbb{E}[D_R] = \int_0^{+\infty} \left[\frac{-\alpha_R + MQ}{2\beta_R \cdot G_R} \right] \cdot f_A(a) \cdot da, \tag{III.1.22}$$

with

$$MQ = \sqrt{\alpha_R^2 + 4\beta_R(\alpha_B \cdot \eta'(a) \cdot K_{B-cito} + \alpha_n D_n + \alpha_\gamma D_\gamma + G_B\beta_B \cdot \eta'^2(a) \cdot K_{B-cito}^2 + MQ')} \tag{III.1.23}$$

and

$$\begin{aligned} MQ' \quad = \quad & G_n\beta_n D_n^2 + 2G_{Bn}G_\gamma\beta_\gamma D_\gamma^2 + \sqrt{\beta_B\beta_n}\eta'(a)K_{B-cito}D_n + 2G_{B\gamma}\sqrt{\beta_B\beta_\gamma}\eta'(a)K_{B-cito}D_\gamma \\ & + 2G_{\gamma n}\sqrt{\beta_\gamma\beta_n}D_\gamma D_n. \end{aligned} \tag{III.1.24}$$

To correct the dose in survival experiments (evaluation of Equation III.1.19) and to calculate the photon isoeffective dose in patients (evaluation of Equation III.1.22), it is essential to determine both the radiobiological parameters and the probability density function of the random variable a, $f_A(a)$.
In particular, the distribution of the random variable a will be determined experimentally using neutron autoradiography, which enables the separate assessment of the microdistribution of ^{10}B in the nucleus and cytoplasm. Meanwhile the *intra-site mean specific energy* will be estimated computationally through Monte Carlo simulations performed with the PHITS code, as this information is essential for the calculation of the factor $\eta'(a)$.
These aspects will be addressed in the following chapters, along with a sensitivity analysis in which perturbations to the model parameters are introduced and the resulting changes in dosimetric outcomes are assessed.

CHAPTER III.2

MEASUREMENT OF BORON-10 MICRODISRIBUTION IN CELLS

Accurate knowledge of the location $^{10}\mathrm{B}$ nuclei in the tumor and surrounding healthy tissue is crucial for optimizing a BNCT treatment. Due to the complexity of tissue structures, $^{10}\mathrm{B}$ can accumulate in different amounts in the various layers, affecting the dose distribution. Moreover, some studies show the dosimetric effect of tissue heterogeneity in terms of radiosensitivity for other types of radiotherapy [75, 149].
In the previous Chapters, the importance of an accurate dosimetric model was emphasized, as it enables a better understanding of the dose-response relationship. Chapter III.1 describes how to correct the $^{10}\mathrm{B}$ uniform-based dose component by including a factor (η' factor) of Eq. III.1.20 to account for $^{10}\mathrm{B}$ heterogeneity at cellular level. To calculate η', it is essential to know a, which represents the ratio of $^{10}\mathrm{B}$ concentration in the nucleus and cytoplasm. Therefore, determining the $^{10}\mathrm{B}$ concentration in both cellular compartments becomes essential to properly feed the microdosimetry model.

As described in Section III.2, one of the possible techniques is neutron autoradiography.

III.2.1 Biological experiment

The neutron autoradiography experiments on the GBM U-87 cell line were carried out at the "Laboratorio de Trazas Nucleares y Autorradiografía Neutrónica, LATAN", in the Commisión Nacional de Energía Átomica, CNEA in Buenos Aires Argentina [91]. Polycarbonate was used as a nuclear track detector: Lexan$^{\mathrm{TM}}$. Lexan is an easy material to manipulate, does not require a long etching time, and is not sensitive to protons emitted in the reaction $^{14}\mathrm{N}(n,p)^{14}\mathrm{C}$, considering that

^{14}N is a fundamental constituent of cellular macromolecules such as DNA, RNA, and proteins [150].

For the experiment involving cells, it is necessary to cut the detectors in a circular shape to fit into the base of the Petri-60 plates (surface area 21.5 cm^2 - height 16 mm). U-87 cells were seeded on 250 micrometer-thick polycarbonate (Lexan^{TM}) sheets with 5mL of culture medium DMEM (Dulbecco's Modified Eagle Medium) low glucose 5% (v/v) FBS (fetal bovine serum) and 100 units/ml penicillin and 100 mg/ml streptomycin.

The Lexan was pre-treated with 70% alcohol for sterilization, washed with Phosphate-Buffered Saline (PBS), and left to dry in laminar flow. After 24 h from seeding, the cells were incubated with Boronophenylalanine (BPA, 80 ppm) for 4 hours. The concentration of ^{10}B administered to cells and the contact time were selected based on prior experiments conducted by the group [151]. The medium enriched with ^{10}B was then removed, and the sample was rinsed with PBS three times. Three washes were performed to ensure the removal of the remaining ^{10}B not internalized by the cells. The detector with the cells was left for 10 minutes with 2% glutaraldehyde fixation agent in 1x filtered PBS at low temperature to prevent intracellular ^{10}B from migrating. Finally, the Lexan sheet was removed from the Petri dish and allowed to dry.

III.2.2 Generation of autoradiographic images

The cells+NTD assembly was irradiated in the thermal column of the biomedical facility at the RA-3 reactor (Centro Atómico Ezeiza, Argentina). This is an open-pool reactor with an isotropic and uniform neutron flux of (9 ± 1) x 10^9 n · cm^{-2}s^{-1} [152, 153].

Throughout the entire experiment, the neutron flux was monitored [154]. The adopted configuration ensured a uniform distribution of the neutron flux across the 9 cm × 13 cm area at the front face of the irradiation box, which corresponds to the section entering the irradiation chamber (see Fig. III.2.1).

Two neutron fluence values were evaluated: 10^{12} n · cm^{-2} and 10^{13} n · cm^{-2}, to select the proper conditions for a clear observation of the tracks within the cellular compartments without events overlap. The test showed that the appropriate fluence for this type of analysis and this cell line was 10^{12} n · cm^{-2}, confirming what had been previously reported in [100].

Figure III.2.1 shows how the samples were fixed on 9 cm × 13 cm Lexan films. The Lexan sheet was then placed in a holder (Fig. III.2.2a) and subsequently exposed to the neutron field in the thermal column of the RA-3 reactor (Fig. III.2.2b).

Following neutron irradiation, the samples were processed. After testing the imprint formation with different staining agents, the optimal images were obtain by coloruring the cells with eosin (15 s) and then the assemblies were exposed to UV-C (254 nm) for 5 minutes. Once the cells were removed from the detector's surface with trypsin+EDTA, the NTDs were treated chemically with PEW solution

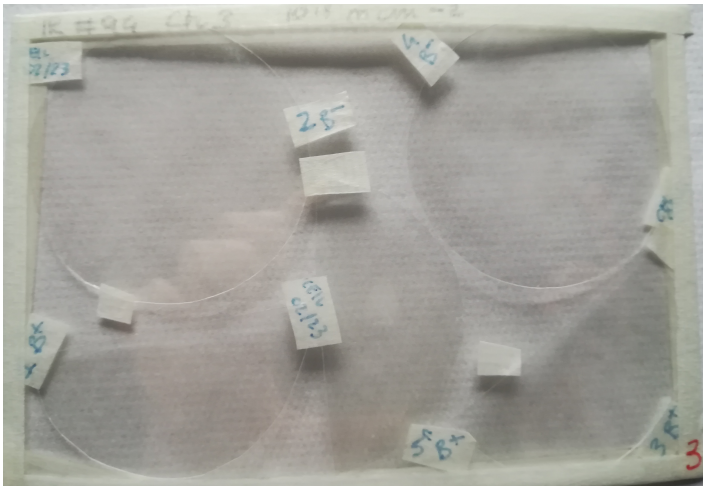

Figure III.2.1: *Irradiation assembly: 9 cm × 13 cm Lexan film used as support for Lexan detectors with cultured cells incubated with BPA and fixed, subsequently exposed to the neutron beam.*

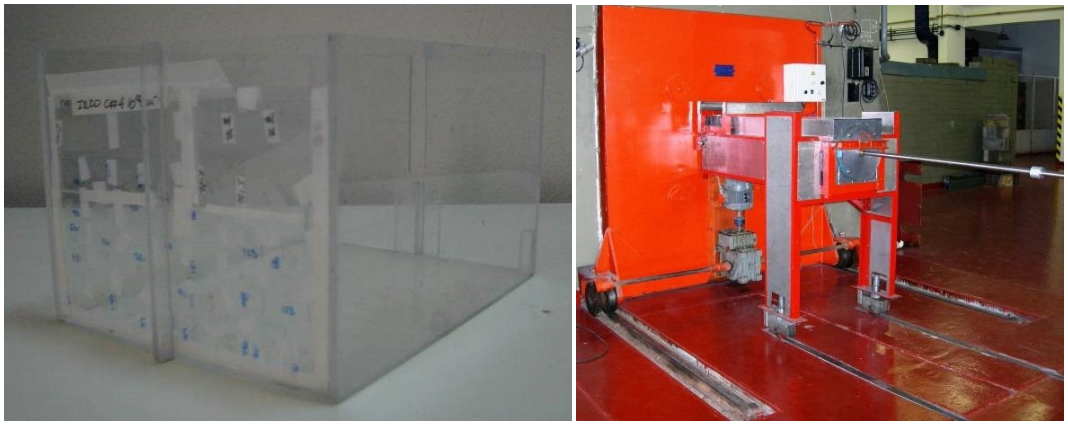

(a) **(b)**

Figure III.2.2: *a) Irradiation envelope in which samples to be irradiated are placed in the thermal column. b) RA-3 reactor thermal column, Ezeiza Atomic Centre, Buenos Aires, Argentina. Kindness of the RA-3 team.*

(30 g KOH[1] + 80 g ethyl alcohol + 90 g distilled water) at 70 °C for 4 min.

III.2.3 Image analysis

Imprints of cells and nuclear track images were observed using a Charge-Coupled Device (CCD) camera (Olympus DP70) with a microscope magnification of 100x. The tracks density quantification was achieved using Image Pro Premier^{TM} 9.11 software, which enabled the recognition and counting of tracks in each image as

[1]Potassium hydroxide

described in [100]. It also allowed the creation of a mask of the tracks. From the imprint images through a homemade program written in MATLAB [155, 156], it was possible to obtain masks of the nucleus and cytoplasm of the cells. From the masks, the number of tracks were derived in the nucleus and cytoplasm and the area of the two subcellular compartments in pixels, then converted into μm^2 through proper calibration.
Figure III.2.3 illustrates an example from the U-87 cell line: at the top-left and top-right, the tracks and the imprint of a cell are shown, while at the bottom, the corresponding masks of the cytoplasm, nucleus, and tracks are displayed. The nucleus and cytoplasm masks are derived from the cell imprint, and the track mask is generated from the track image.

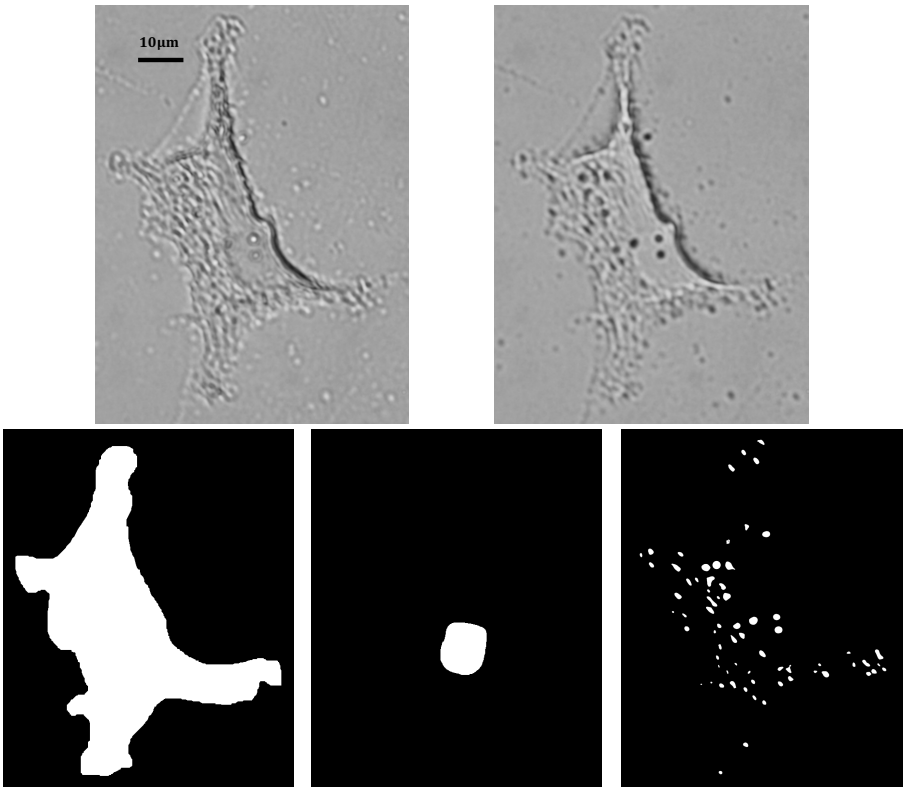

Figure III.2.3: *Example of U-87 cell tracks (top-left image) and imprints (top-right image) obtained with 15 s of eosin staining, 5 min UV-C exposure and 4 min etching. The tracks are recognizable in the image on the left with the black dots, while the darker ellipsoid-shaped nucleus and cytoplasm can be recognized in the imprint. Below, the cytoplasm mask, nucleus mask, and track mask are displayed, respectively.*

A total of 310 cells were analyzed, and the nucleus and cytoplasm track density was obtained for each cell according to Eq. III.2.1.

$$\text{Track density} = \frac{\text{number of tracks}}{\text{area } [\mu m^2]}. \tag{III.2.1}$$

The ^{10}B concentration in parts per million (ppm) was determined using a calibration curve. Liquid samples with known ^{10}B concentrations ranging from 0 to 100 ppm were irradiated and processed as described in [92], and the resulting tracks densities were measured to construct a tracks density curve as a function of ^{10}B concentration in ppm. For further details see Appendix A. Additionally, fading effect was compensated using a correction factor calculated by analyzing images with and without UV-C radiation exposure [157]. The fading coefficient, also referred to as Relative Track Density (RTD), is defined as

$$RTD = \frac{\text{Track density (t h UV)}}{\text{Track density (0 h UV)}}, \tag{III.2.2}$$

as introduced by Saint Martin et al. [105]. This factor was found to be 34%, indicating that the measured track density represents only 66% of the original value. Thus, the measured track density was multiplied by a correction factor of 1.51 to compensate for the loss of track due to fading.

III.2.4 Quantification of ^{10}B distribution

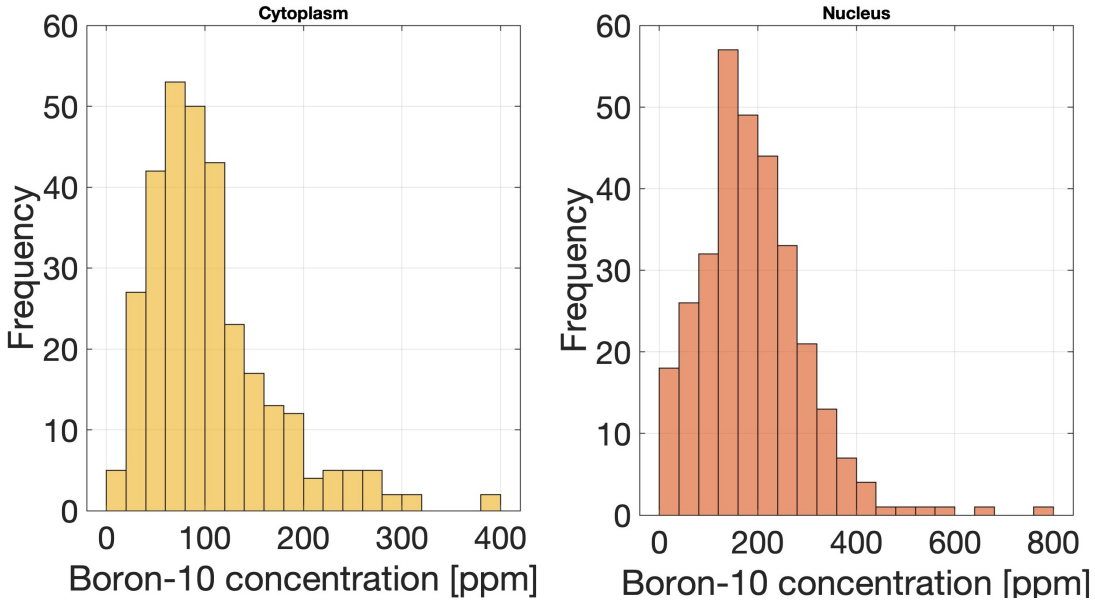

Figure III.2.4: *U-87 cell line ^{10}B distribution at the subcellular level: cytoplasm (left) and nucleus (right).*

Figure III.2.4 shows the ^{10}B distributions for the two cellular compartments, the cytoplasm in yellow and the nucleus in orange, obtained from neutron autoradiography.
The distribution of ^{10}B concentration in the nucleus covers a wide range, from 0 ppm to 800 ppm. The mean value is 188 (see Table III.2.1), with a standard deviation of 108 ppm, indicating that, although the average concentration of ^{10}B in the

	Cytoplasm	*Nucleus*
^{10}B [ppm]	105±63	188±108

Table III.2.1: *The mean value of U-87 cell line ^{10}B concentration in the nucleus and cytoplasm, with the associated error corresponding to 1σ (standard deviation).*

nucleus is high, there is a considerable variability among individual nuclei. The high standard deviation indicates a wide range of ^{10}B concentrations within the nucleus.
The distribution of ^{10}B concentration in the cytoplasm shows a range from 0 ppm to 400 ppm. It has an average of 105 ppm (see Table III.2.1), with a standard deviation of 63 ppm.

Although BPA is not nucleus-specific, ^{10}B concentrates more than twice in the nucleus than in the cytoplasm in this cell line. This finding is interesting as it suggests a tendency for ^{10}B to localize more in the nucleus, which could have significant implications for the efficacy of BNCT for GBM. The higher concentration of ^{10}B in the nucleus could potentially increase direct DNA damage in cancer cells, improving therapeutic efficacy.
Another study [158] reported nuclear track localization in the GBM U-251 cell line. Although the authors did not report boron concentration in the two cell compartments, heterogeneity in the distribution of tracks between the nucleus and cytoplasm is clearly evident in their images, with an evident preferential accumulation of BPA in the nucleus. Of the 310 cells analyzed analyzed in Buenos Aires, 68 show a nucleus-cytoplasm boron ratio $a < 1$ and 241 a value of $a > 1$. Only one cell has $a = 1$, corresponding to a uniform boron distribution between the nucleus and cytoplasm ($B_{nuc} = B_{cyto}$). In probabilistic terms, 22% of the cells show a ratio $a \leq 1$, while the remaining 78% have $a > 1$, indicating a predominant tendency for boron accumulation in the nucleus.

The next step was to fit the empirical cumulative distribution of the ^{10}B ratio a with a known probability distribution, to enable the translation of empirical observations into a mathematical model. Among tested distributions, the lognormal probability distribution was found to best approximate the data. This approach provides an analytical expression for the probability density associated with the parameter, producing a more accurate representation and facilitating the calculation of related quantities, such as the expected value of the dose.
Figure III.2.5 shows the empirical cumulative distribution of the ^{10}B ratio a and its fit with the lognormal probability distributions.
For calculating the cumulative probability distribution of the ^{10}B nucleus-cytoplasm concentration ratio, experimental data in which the number of capture events in the nucleus was zero were excluded. These discarded cases (about 10 out of 310 analyzed cells) represent only a small fraction of the total sample. The choice of

removing them from the distribution is justified because we are using discrete data (i.e., number of tracks) to represent a continuous variable (i.e., boron concentration). Thus, zero detected capture events correspond to all non-zero boron concentrations below a certain threshold, determined by the detection limit of the experimental method.

To assess the goodness-of-fit between the nucleus-cytoplasm ratio data and the lognormal model, a Kolmogorov-Smirnov (K-S) test was performed. The results showed a p-value of 0.27: there is no statistically significant evidence to reject the H_0 hypothesis that the data follow a lognormal distribution (at a 1% significance level).

As mentioned before, having the analytical expression of the distribution allows to translate empirical observations into a mathematical model. In particular, for the case under study, it is possible to describe $f_A(a)$ in equations (III.1.21) and (III.1.22) using the Lognormal form and to calculate the expected value of the dose. This function has the form

$$f_A(a) = \frac{1}{a\,\sigma\sqrt{2\pi}} \exp\left(-\frac{(\ln a - \mu)^2}{2\sigma^2}\right), \tag{III.2.3}$$

with $\mu_{U-87} = 0.59$ and $\sigma_{U-87} = 0.78$, as obtained from the fit to the experimental data. Based on this distribution, the expected value of the nucleus-cytoplasm ^{10}B ratio is $\mathbb{E}[a] = 2.444 \pm 0.009$.

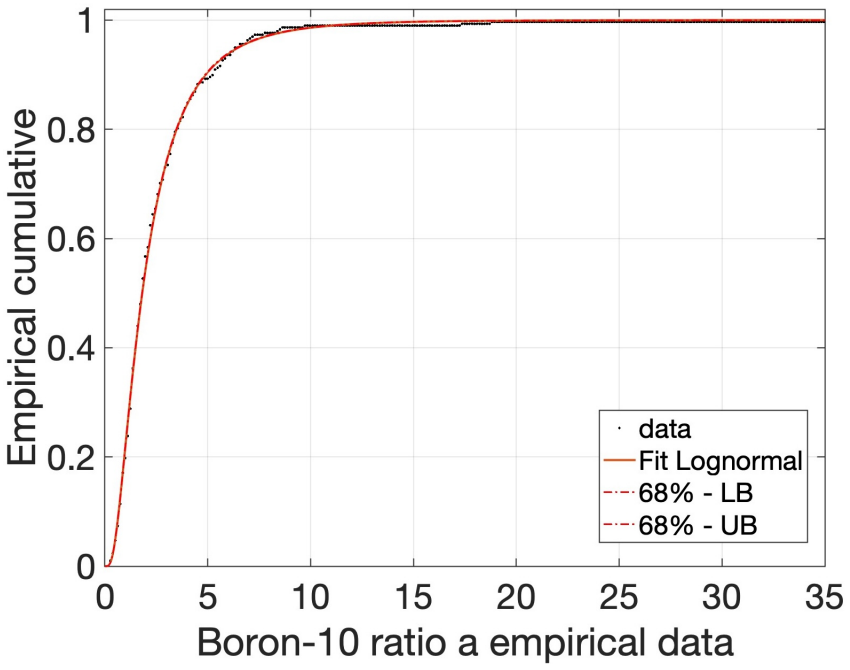

Figure III.2.5: *Empirical cumulative distribution of a and fit with lognormal probability distributions. Lognormal model parameters obtained from the fitting are:* $\mu_{U-87} = 0.593[0.590, 0.596]$ *and* $\sigma_{U-87} = 0.775[0.772, 0.779]$.

The use of a lognormal distribution to describe concentration ratios is not unique to the present study: this behavior was also reported in various biological systems. For example, studies on the distribution of PET SUV, defined as the ratio of the activity concentration of the radiolabeled substance in a region of interest to the average administered activity concentration, normalized for patient weight, have shown that the variability of FluoroDeoxyglucose (FDG) accumulation in tumors can be modeled by a lognormal distribution. This phenomenon arises from multiplicative biological processes, such as glucose metabolism and tissue perfusion, in which a multiplicity of physiological and metabolic factors influence the uptake of the radiolabeled substance [159, 160]. In addition, this behavior is consistent with that observed in [161], where the tumor-to-blood $^{10}\mathrm{B}$ concentration ratio was also shown to follow a lognormal distribution. These analogies reinforce the notion that the observed lognormal distribution of the boron concentration ratio is not only statistically sound but also biologically meaningful, making it a robust choice for modeling heterogeneity in BNCT dosimetry.

Quantification of uncertainties in neutron autoradiography and its impact on dose

The value of the boron concentration estimated using the neutron autoradiography technique is influenced by several sources of uncertainty, including the error associated with the neutron flux, the variability of the etching process, the track recognition threshold, the calibration curve fitting, and the tracks' depth location. Firstly, the neutron flux has an uncertainty which, based on the reference literature [162], is estimated to be approximately 8%. This contribution represents a source of systematic error that directly affects the determination of track density. To minimise variations due to etching, specific acceptability limits have been established in the preparation of solutions and laboratory processes. In particular, during the preparation of the chemical etching solution, it is ensured that the weighing of each component (water, alcohol, and KOH) does not deviate by more than 5%. This measure limits the impact of chemical variations on the etching rate and the morphology of the tracks. The temperature of the bath, which can affect the etching velocity, is always monitored before each experiment. In addition, the duration of the chemical etching is strictly controlled using a chronometer to ensure the reproducibility of the process. The etching is finally interrupted by cooling the samples with ice, further reducing the possibility of variations in the depth of the tracks. Regarding observability, a strict protocol is followed for setting up the microscope. Lighting conditions, magnification, acquisition parameters, and the focusing procedure are kept constant for all observations in order to ensure consistent acquisition conditions between different measurements. Although these contributions have not been explicitly quantified, they are considered essential to ensure the reproducibility of the results.
The use of ultraviolet radiation to generate cell imprints introduces the phenomenon of fading, i.e., a loss of tracks. To correct this effect, the number of tracks observed

is multiplied by a correction factor. The uncertainty associated with this parameter is approximately 10% and was determined by error propagation. Specifically, the estimate was obtained by comparing the track density measured in reference samples with homogeneous concentrations, analysed under identical conditions, except for the presence or absence of UV-C irradiation. A further source of uncertainty is associated with the calibration curve used to convert track density into boron concentration (ppm). The uncertainty associated with interpolation on the calibration curve was estimated with reference to [163], resulting in 4%. A significant contribution to the overall uncertainty also derives from the natural biological variability in the intracellular distribution of boron. This variability, estimated from the distribution of concentrations reconstructed cell by cell, is often greater than the intrinsic error of the experimental technique. The relative biological error was calculated as the standard deviation divided by the mean value and expressed as a percentage, resulting in 60% for the cytoplasm and 57% for the nucleus. These values are higher than the sum of the technique uncertainties (about 13%).
Finally, in the 2D analysis, the tracks are considered as observed on a single plane. Although there may be variations in the depth of the tracks, the analysis is conducted on a uniform section of the sample. The effect of the depth of the tracks on visibility has not been quantified in this work, but it is an aspect that could be explored in future studies.
It is important to remark that, within the proposed Micro Isoeffective Model, the dose calculation does not rely on a single point estimate of the nuclear and cytoplasmic boron concentrations. Instead, the full probability distribution of the nucleus-to-cytoplasm boron concentration ratio a, experimentally obtained by neutron autoradiography, is used. As a consequence, both the microdosimetric correction factors and the absorbed dose are treated as random variables, and their associated uncertainty naturally propagates through the model. The variance of the absorbed dose thus provides a quantitative measure of the uncertainty associated with the microdosimetric correction. This uncertainty originates from both the experimental limitations of neutron autoradiography and the intrinsic biological variability of boron microdistribution among cells.
Given the random variable a with probability density $f_A(a)$ and considering the relationship between a and $\eta'(a)$, it follows that $\eta'(a)$ is also an random variable with its probability density, denoted as $f_{N'}(\eta')$. The latter can be determined as a function of $f_A(a)$ according to the following procedure.

Applying the definition of cumulative probability $F_{N'}(\eta')$ result to be

$$F_{N'}(\eta') = P\left(N' \leq \eta'\right) \tag{III.2.4}$$

$$= P\left(\frac{1+(a-1)\cdot c}{1+(a-1)\cdot v} \leq \eta'\right) \tag{III.2.5}$$

$$= P\left(a \leq \frac{1-\eta'}{\eta'\cdot v - c} + 1\right) \tag{III.2.6}$$

$$= F_A\left(\frac{1-\eta'}{\eta'\cdot v - c} + 1\right) \tag{III.2.7}$$

Differentiating the cumulative distribution function $F_{N'}(\eta')$, it is possible to obtain the probability density $f_{N'}(\eta')$.

$$f_{N'}(\eta') = f_A\left(\frac{1-\eta'}{\eta'\cdot v - c} + 1\right) \cdot \left|\frac{d}{d\eta}\left(\frac{1-\eta'}{\eta'\cdot v - c} + 1\right)\right|, \tag{III.2.8}$$

where

$$\frac{d}{d\eta}\left(\frac{1-\eta'}{\eta'\cdot v - c} + 1\right) = \frac{c-v}{(\eta'\cdot v - c)^2}. \tag{III.2.9}$$

Then the probability density of $\eta'(a)$ turns out to be

$$f_{N'}(\eta') = \frac{c-v}{(\eta'\cdot v - c)^2} \cdot f_A\left(\frac{1-\eta'}{\eta'\cdot v - c} + 1\right). \tag{III.2.10}$$

The uncertainty associated with the BNCT absorbed dose (from Eq. III.1.21) can be quantified through its variance. Since the boron-independent component is deterministic, the variance of the absorbed dose reads

$$\mathrm{Var}(D_{BNCT}) = \mathrm{Var}\left(K_{B\text{-}cyto}\, B_{cell}\, \eta'\right). \tag{III.2.11}$$

By exploiting the properties of variance under scalar multiplication, one obtains

$$\mathrm{Var}(D_{BNCT}) = \left(K_{B\text{-}cyto}\, B_{cell}\right)^2 \mathrm{Var}(\eta'). \tag{III.2.12}$$

The variance of the microdosimetric correction factor η' is defined as

$$\mathrm{Var}(\eta') = \mathbb{E}[\eta'^2] - \left(\mathbb{E}[\eta']\right)^2, \tag{III.2.13}$$

where the second-order moment is given by

$$\mathbb{E}[\eta'^2] = \int_0^{+\infty} \eta'^2\, f_{N'}(\eta')\, d\eta'. \tag{III.2.14}$$

In this probabilistic framework, the propagation of microdosimetric uncertainty into the absorbed dose is naturally accounted for through the variance of D_{BNCT}. Therefore, the uncertainty in the absorbed dose directly depends on the width of the probability density function $f_{N'}(\eta')$, which incorporates both the experimental

uncertainties associated with neutron autoradiography measurements and the intrinsic biological variability of boron microdistribution at the subcellular level. A full analytical derivation of the probability density function of the Photon Isoeffective Dose, $f_{D_R}(d)$, as a function of the nucleus-to-cytoplasm boron ratio distribution $f_A(a)$ could be addressed in future work.

This Chapter provided the experimental data necessary to characterize the distribution of boron concentrations in the cell compartments. These results form the basis for the implementation of the dosimetric model, which will be developed in Chapter III.3.

CHAPTER III.3

COMPUTATIONAL MICRODOSIMETRIC ANALYSIS AND RADIOBIOLOGICAL EXPERIMENT CORRECTIONS

III.3.1 Computational calculation of intrasite frequency mean specific energy

In Chapter III.1, it was shown that, when boron concentration values inside and outside the target site are different, the microscopic boron dose can be expressed as the product of the KERMA/dose (calculated from the reaction rates outside the site of interest) and a factor that accounts for the cell size and shape, and for boron concentration ratio.
The term z_F^I of Eq. III.1.8 was calculated by simulations with the Monte Carlo code PHITS [164], considering the cell nucleus as the site of interest. Reliable simulations were obtained since the geometry of the nucleus was determined from the cell images experimentally acquired. The geometry of the nucleus was modeled as a prolate spheroid with equatorial radii $a = 5.2$ μm and a polar radius $b = 7.3$ μm, based on measurements of approximately 300 cells obtained from neutron autoradiography images. The cytoplasm was modeled as a surrounding spheroid with semi-axes of 20 μm, 15 μm, and 15 μm, enclosing the nucleus. The two structures were assumed to be *concentric*, in a simplified but realistic model for a cell. The entire cell was placed within a medium representing the culture environment. Because the site of interest is the cell nucleus, the specific energy spectrum was calculated solely within the nuclear volume. Accordingly, the simulation tally was also limited to the cell representing the nucleus. The geometry of the cytoplasm and the environment outside the cell was included for structural completeness, but

it plays a secondary role in the analysis because the score (tally) and the source are in the cell nucleus.

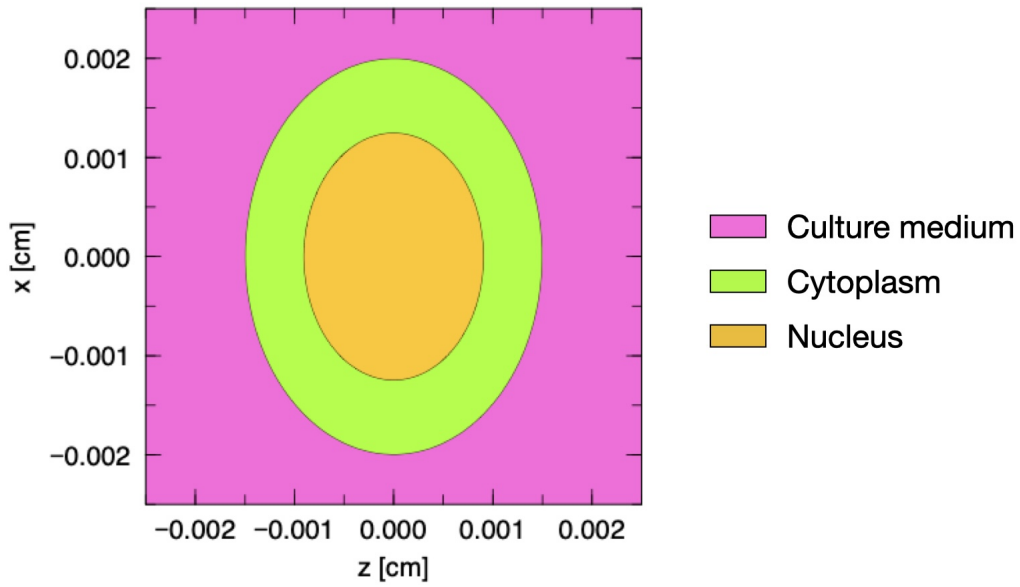

Figure III.3.1: *Cell geometry used in the PHITS similation.*

A back-to-back particle source was generated within the nucleus, emitting alpha particles and lithium ions with the characteristic energies resulting from the two boron neutron capture reaction channels (Section I.2). To accurately estimate the spectrum of the specific energy deposited in the cell nucleus as a result of the neutron capture reaction in $^{10}\mathrm{B}$, two separate simulations were conducted, with the energy of the particles α and $^{7}\mathrm{Li}$ emitted according to the two decay channels, each with its own *branching ratio*. In both simulations, the *T-Deposit tally* was used, which provides the spectrum in terms of the number of particles emitted for each energy interval (*bin*), thus allowing reconstruction of the specific energy distribution in the volume of interest.
The intrasite mean specific energy z_F^I was then calculated for each simulated case. Finally, the results obtained were combined employing a weighted *average* according to the relative *branching ratio*, to obtain the average value to use in the dosimetry model.
The Figure III.3.2 shows a projection in the x-z plane, where the core is represented by a prolate spheroid section. The yellow traces indicate the trajectories of heavy charged particles emitted from a single neutron capture event occurring inside the nucleus (BR = 6.3%). The thin black lines highlight the contours of the nucleus and the cytoplasm modeled as a concentrically larger ellipsoid. The side color map represents the normalized particle flux [1/cm^2/particle source per unit time] in the simulated domain.
The PHITS output was processed using a MATLAB [155] script to obtain the single-event specific energy spectrum for the two branches.

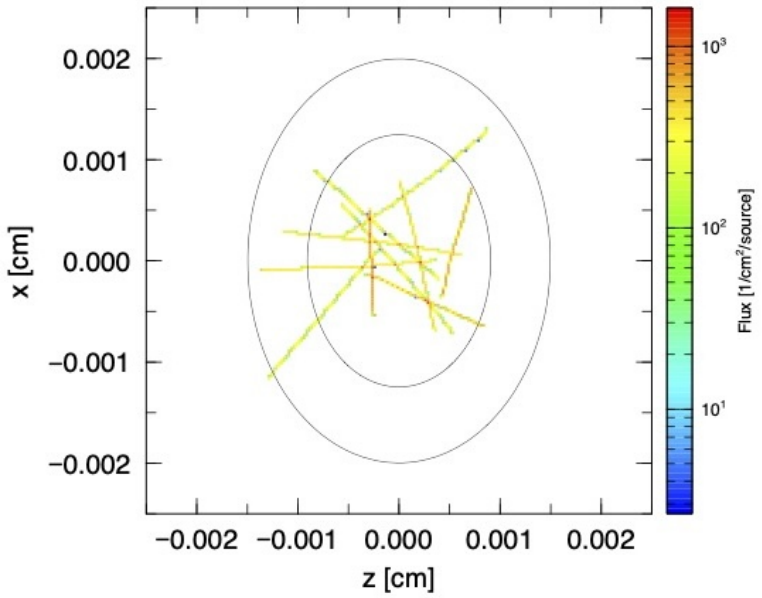

Figure III.3.2: *Tracks of the α and ^{7}Li particles simultaneously emitted within the cell nucleus following the neutron capture reaction in ^{10}B. The simulation reported is for the branching ratio of 6.3%.*

Figure III.3.3 shows the result of the weighted sum of the two spectra, from which the value of z_F^I was derived.

Special emphasis is placed on the fact that z_F^I depends only on the properties of the target volume itself, namely its shape and size (volume), and not on its position within the surrounding cytoplasm.
In the Monte Carlo simulations, for simplicity, the nucleus is modelled as concentric with the cytoplasm and the cytoplasm is described using an idealised geometry. However, this geometrical assumption does not affect the final value of z_F^I, since the sensitive site is the nucleus and the energy deposition is tallied locally within that volume. The relative position of the nucleus with respect to the cytoplasm, as well as the detailed cytoplasmic geometry, therefore do not influence the calculated z_F^I.

III.3.2 Dose-survival curves correction

In Part II of this thesis, the dose-dependent cell survival experiment for the U-87 cell line, representative of GBM, was described. Cells were irradiated with photons from ^{60}Co, neutrons, and neutrons in the presence of BPA. The experimental data were analyzed and fitted using the modified linear-quadratic model, which considers the repair capacity of cell damage through the Lea-Catcheside factor and synergism (SetionI.3).
As mentioned in section III.1, the considerations made on microdosimetry can

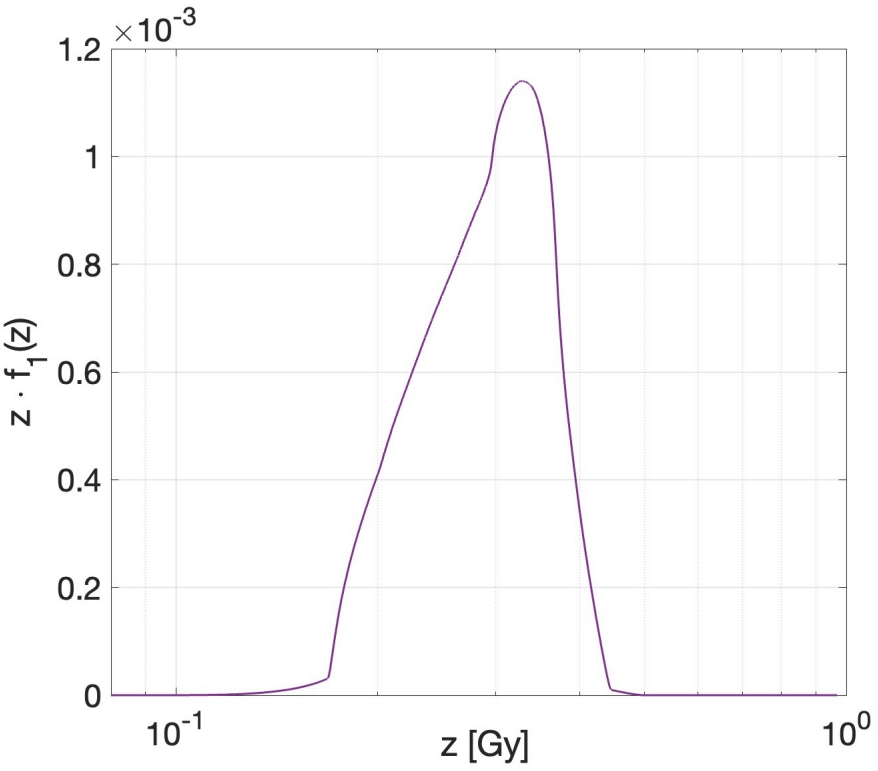

Figure III.3.3: *Single event specific energy spectrum for internal sources obtained by PHITS as result of the two branches of the neutron capture reaction in ^{10}B.*

be applied to the U-87 cell survival curves. The η' factor (Eq. III.1.20) and the probability density function $f_A(a)$ (Eq. III.2.3) jointly correct the BNCT boron dose component to account for the microdosimetry aspects and the variability of the random variable cytoplasm-to-nucleus boron concentration ratio a, as previously described. Accordingly, the expected value of the absorbed dose can therefore be calculated using equation III.1.21.

From the neutron autoradiography experiment, the areas of the nucleus and cytoplasm in μm^2 are known for all analyzed cells, allowing the determination of their volumes using Eq. III.3.1.

$$Vol_i = [Area_i]^{3/2} \qquad i = nucleus,\ cytoplasm. \tag{III.3.1}$$

The relationship in Eq. III.3.1 is based on isometric geometric scaling, where area scales as L^2 and volume as L^3. Under the assumption of a proportional cell shape, this yields the exponent $3/2$, an approximation when estimating volumes from 2D projections in cellular and microanatomical studies [165]. Given the nucleus and cytoplasm volumes, the nucleus-to-cell volume fraction v in expression η' can be determined ($v_{U-87} = 0.024 \pm 0.001$).

To calculate the corrected boron dose for the experiment, three inputs were required: (i) the nucleus-to-cell volume fraction v, derived from the measured cell

geometries; (ii) the probability distribution $f_A(a)$, obtained in Section III.2.3; and (iii) the macroscopic boron concentration B_{cell}, which was measured experimentally in a twin flask during each irradiation, yielding approximately 20 ppm. With these values, the expected absorbed dose was computed.
The fit of the cell survival as a function of the dose, corrected as described, is shown in Figure III.3.4.

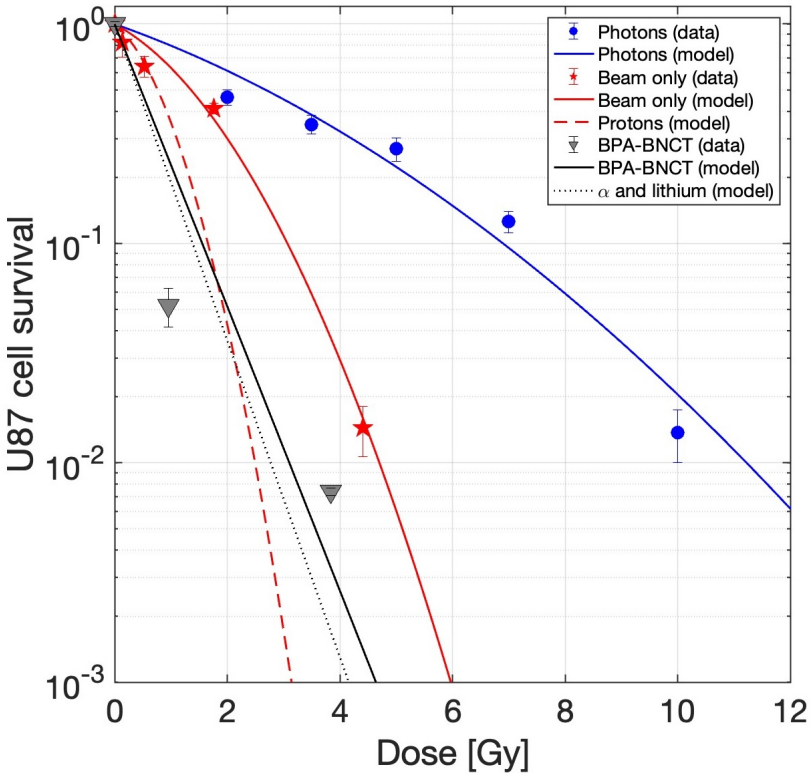

Figure III.3.4: *Survival curves of U-87 cells as a function of the absorbed dose. The dots and blue line represent the reference radiation data (^{60}Co) and the fit, respectively. The red curve and red stars represent the fit and experimental data for beam-only irradiation, respectively. The dashed red curve represents the isolated proton contribution (i.e., subtracting the effect of photons). The solid black curve is the fit of the BNCT experimental points (black triangles). The dashed black line is the model considering only the boron component (i.e., subtracting the contributions of photons, protons, and ^{14}C). The boron dose was corrected with the η' factor.*

Table III.3.1 lists the parameters of the modified LQ model for the GBM cell line when the correction to the boron dose is applied.
The impact of the dose correction on the cell survival experiment was studied through the determination of the CBE values at 1% of survival, calculated for the uncorrected (*Macro*) and corrected (*Micro*) dosimetry models. The results are presented in Table III.3.2, which also includes the percentage difference between

Radiobiological parameters for GBM			
	Photon	**Neutron**	**Boron**
α_i $[Gy^{-1}]$	0.21 [0.13, 0.30]	0.488 [0.003, 1.81]	1.66 [1.30, 2.02]
β_i $[Gy^{-2}]$	0.019 [0.009, 0.032]	0.55 [0.17, 1.35]	0
with $i = B, n, \gamma$ from Eq. II.1.5			.

Table III.3.1: *Radiobiological parameters for GBM, obtained from fitting the cell survival data versus dose for beam-only and BPA-BNCT irradiation (boron component corrected with the microdosimetric correction factor), using ^{60}Co as radiation reference. The confidence intervals associated with the parameters correspond to a 68% confidence level.*

the two factors.
Notably, the $CBE_{1\%}$ value obtained after the correction for the actual boron distribution is substantially lower than the uncorrected value, indicating that neglecting subcellular distribution leads to a significant overestimation of the biological effectiveness of the boron dose. Because the boron dose is usually the highest contribution in the tumor, this results in a significant overestimation of the total tumor dose. The difference of 47% between the corrected and uncorrected CBE highlights the necessity of incorporating microdosimetric aspects into BNCT dose calculations to better compare the effectiveness of BNCT to the standard photon therapy, thus improving the capacity to describe the treatment and, ultimately, enabling the prescription of a more accurate dose.

$CBE_{1\%}$		
Macro	*Micro*	*Percentage difference*
7.5 ± 0.9	4.0 ± 0.5	47%

Table III.3.2: *CBE values at 1% of survival, calculated with respect to the reference radiation ^{60}Co. The calculations were performed with correction for the microdosimetric factor η' and $f_A(a)$ (Micro approach) and without correction (Macro approach).*

For a clearer interpretation of the results shown in Table III.3.2, Equation III.1.21 can be reformulated as follows

$$\mathbb{E}[D_{cell}] = D_{B_{ind}} + K_{B-cyto} \cdot B_{cell} \cdot \mathbb{E}[\eta'(a)]. \tag{III.3.2}$$

Figure III.3.5 shows the expected value of $\eta', \mathbb{E}[\eta']$, as a function of the volume fraction of the nucleus, v.
In the case of the U-87 cell line, for which $v = 0.024 \pm 0.001$, the corresponding value of $\mathbb{E}[\eta']$ turns out to be about 1.8, as can be observed in Fig. III.3.5. Since $\mathbb{E}[\eta']$ acts as a multiplicative factor for boron KERMA per ppm (Eq. III.3.2), this leads to an increase of boron dose component compared to the uncorrected cal-

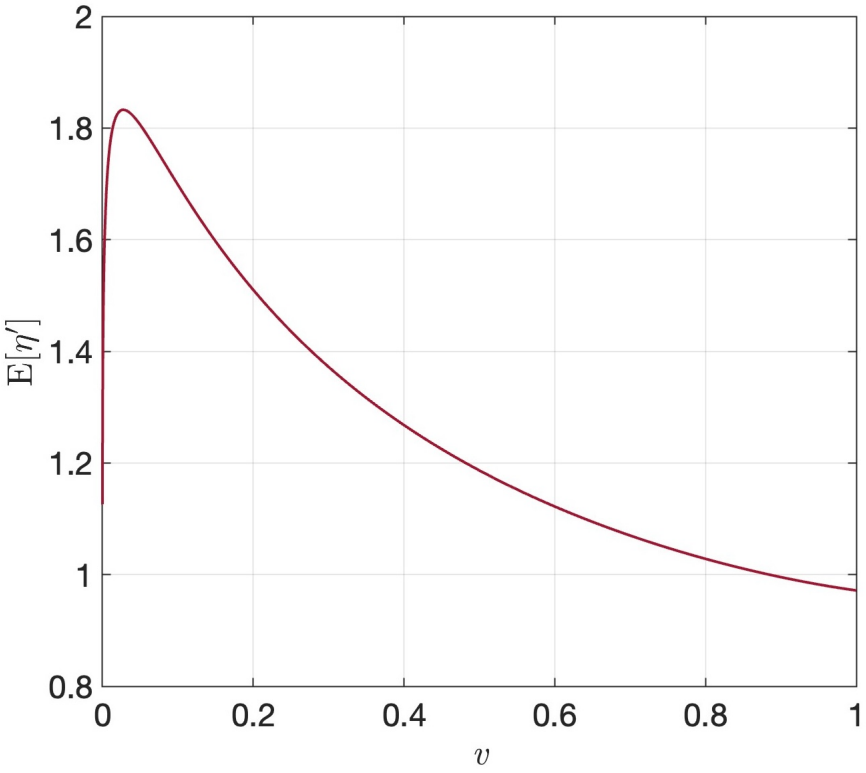

Figure III.3.5: *Trend of the expected value of η', with respect to the volume fraction of the nucleus v.*

culation. Consequently, the dose-effect curve shifts to the left, resulting in a dramatic reduction in the radiobiological parameter α_B. This increase in boron dose ultimately results in the lower CBE value at 1% of survival.

III.3.2.1 Analysis of variability factor η' and radiobiological parameter α_B as a function of the volume fraction v

Figure III.3.5 shows the trend of the expected value of η' with respect to the nucleus-to-cell volume fraction v.
To further interpret this behavior, Figure III.3.6 presents η' for different values of a. The left panel corresponds to $a > 1$ ($B_{nuc} > B_{cyto}$), with curves for a between 1 and 50, while the right panel corresponds to $a < 1$ ($B_{nuc} < B_{cyto}$), with curves for a between 0 and 1.
It can be seen that for v=0.9 (i.e., when the nucleus occupies 90% of the cell volume), η' equals 1 in both cases. More specifically: for $a > 1$ (left panel), $\eta' > 1$ when $v < 0.9$ and $\eta' < 1$ when $v > 0.9$. Conversely, for $a < 1$ (right panel), $\eta' < 1$ when $v < 0.9$ and $\eta' > 1$ when $v > 0.9$.
In the case where $a < 1$, for almost all values of v, the correction factor η' is greater than one and thus it always increases the boron dose contribution. In contrast, when $a > 1$, $\eta' < 1$ and thus it reduces the boron dose contribution.

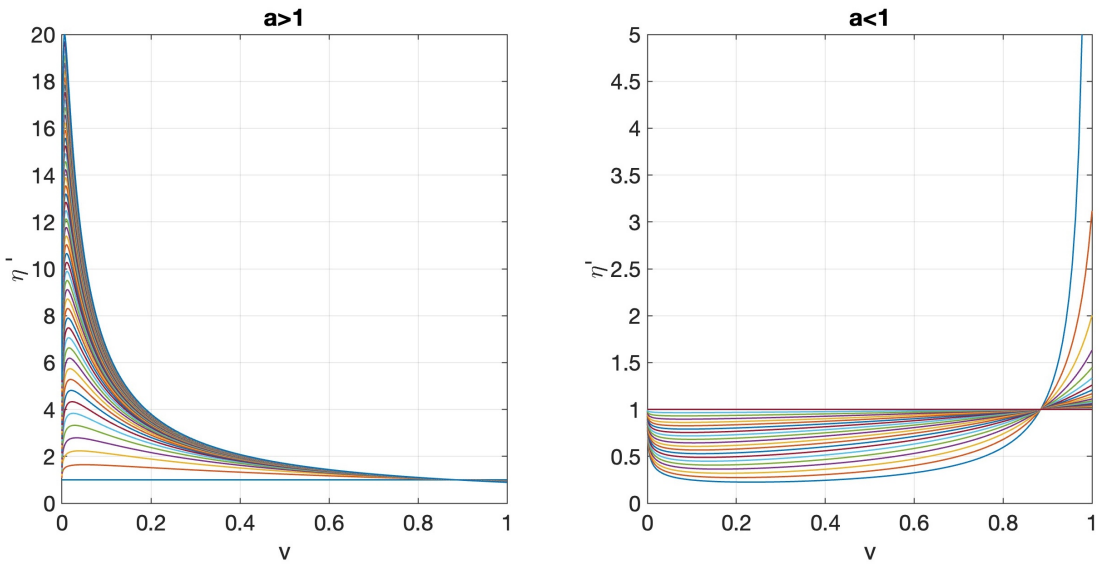

Figure III.3.6: *η' as a function of v for different values of a. Left: $a > 1$. Right: $a < 1$.*

By integrating the curves shown in Figure III.3.6 over all possible values of a, the expected value of η' is obtained and shown in Figure III.3.5.
Given the variability of the expected value of η' with v, we next analyzed how the radiobiological parameter α_B of the boron dose component for the Photon Isoeffective Dose Model changes as a function of v. The volume of the cell was kept constant while varying the volume of the nucleus. To this end, η' was calculated for different values of v (specifically: 0.005, 0.010, 0.020, 0.030, 0.040, 0.050, 0.060, 0.070, 0.080, 0.090, 0.100, 0.200, 0.300, 0.400, 0.500, 0.600, 0.700, 0.800, 0.900, 0.927, 0.940, 0.970). For each value of v, the radiobiological cell survival experiment was corrected and then fitted to determine the corresponding value of α_B.
Figure III.3.7 shows the obtained values of the radiobiological parameter α_B as a function of v. The error bars shown in the Figure correspond to a confidence interval of 68%.
It is evident that the trend of α_B is different for values of $v < 0.1$ and values of $v \geq 0.1$. Therefore, two distinct functions have been identified to describe the different behavior of α_B in the two regions:

- for $v \geq 0.1$ a power function:

$$\alpha_B(v) = a \cdot v^b + c,$$

  as shown in Figure III.3.8;

- for $v < 0.1$ a more linear power function:

$$\alpha_B(v) = a \cdot v^b + c \cdot v + d,$$

  as shown in Figure III.3.9.

A chi-square test was applied to both fits, demonstrating the compatibility of the models with the experimental data, with a significance level of 5% in both cases.

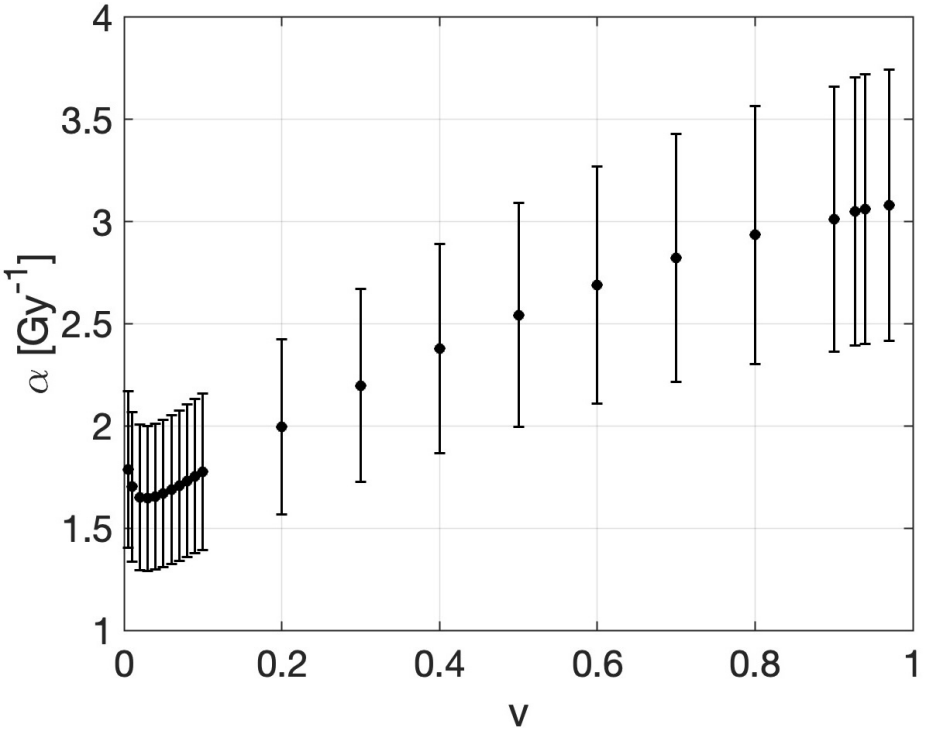

Figure III.3.7: *Radiobiological parameter of the boron dose component α_B as a function of the nucleus volume fraction v.*

It can be observed that the trend of the curve of α_B is specular to that of $\mathbb{E}[\eta']$ concerning the *x-axis*: in practice, where $E[\eta']$ decreases, α_B increases, and vice versa. This behavior reflects the fact that both are multiplicative factors applied to the same boron dose, which remains unchanged; therefore, an increase in $E[\eta']$ leads to a decrease in the value of α_B and vice versa.
In the next Chapter, the impact of this microdosimetric study will be analyzed in a clinical scenario, i.e., a patient affected by GBM. Building on the formulation of the macroscopic dose calculation, extensively discussed in Part II and referred to as the *Macro Model*, the stochastic component of energy deposition, related to a boron bi-valued boron distribution across the two cellular compartments, will be integrated. This approach will be referred to as the *Micro Model*.

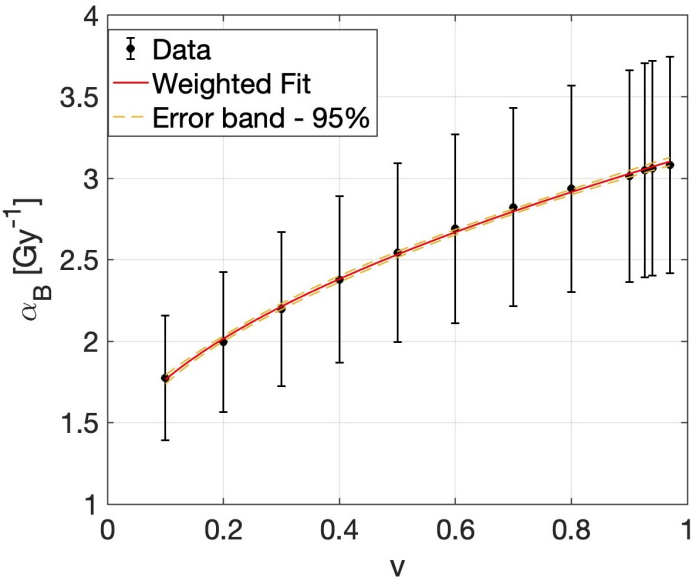

Figure III.3.8: *Radiobiological parameter of the boron dose component α_B, as a function of the nucleus volume fraction v (for $v > 1$). Fit parameters (with 95% confidence interval): $a = 1.92\ [1.76, 2.08]$ Gy^{-1}, $b = 0.54\ [0.46, 0.63]$, $c = 1.22\ [1.04, 1.39]$ Gy^{-1}. The chi-square test confirmed good agreement between the model and the data (p-value > 0.05).*

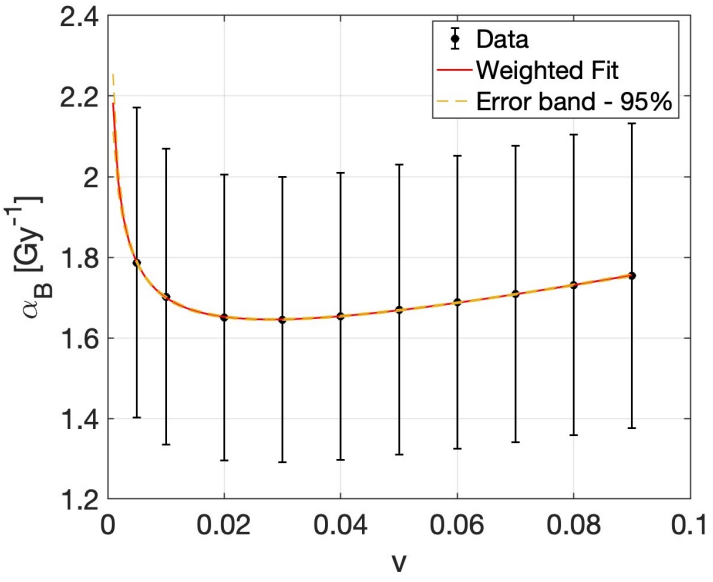

Figure III.3.9: *As in Figure III.3.8, for $v < 1$.*

CHAPTER III.4

APPLICATION TO A GLIOBLASTOMA MULTIFORME PATIENT

When introducing the stochastic aspects of energy deposition related to the non-uniformity of boron concentration at the subcellular level and considering the nucleus-cytoplasm boron ratio as a stochastic variable, the dose also becomes a stochastic variable. The Section III.1 explained the method for calculating the expected value of the isoeffective dose.
This Chapter applies the presented concepts to a clinical case, to evaluate their impact in a realistic treatment scenario.
The example chosen is a patient affected by GBM whose medical images were downloaded from a free public archive, *The Cancer Imaging Archive*, *TCIA* (https://www.cancerimagingarchive.net/). A voxelized model of the patient was generated using the IT_START treatment planning system (see Chapter II.3), which produced the input file for the irradiation simulation via the transport code MCNP6.3 [126, 135].
The criterion for positioning was to minimize the distance of the center of mass of the GTV from the beam port; this corresponds to maximizing the irradiation of the GTV. At this stage, the optimization of the treatment was not a goal, the situation simulated is only representative for relative evaluations. The simulation was performed using the RFQ neutron beam as before.
Simulations return the dose rate matrices in the tumor and the other regions of interest. Specifically, these are the dose values calculated assuming CPE (KERMA) and a uniform boron-10 concentration. These matrices represent the BNCT dose components D_i (with $i = B, n, \gamma$) that appear in Equations II.1.5 and III.1.24.
The irradiation time was fixed prescribing a maximum dose in the healthy brain of 13 Gy (RBE), applying the standard dose calculation widely used in clinical BNCT so far, that assumes fixed RBE and CBE fixed factors, i.e., $CBE = 1.35$,

$RBE_{th} = RBE_f = 3.2$, $RBE_\gamma = 1$.
Figure III.4.1 shows the Dose Volume Histogram (DVH) in which the dose delivered to the tumor was calculated using the Photon Isoeffective Dose model, given by Eq. II.1.5 and II.1.6, applying three different approaches. In all cases, a typical average boron concentration value of 50 ppm was assumed for the tumor. The blue curve represents the case where the boron concentration was considered uniform in the tumor and in all the cell compartments (*Macro Model*). The dashed red curve (*Macro [RB-Corrected]*), shows the photon isoeffective dose calculated using corrected radiobiological parameters derived from cell survival experiments also corrected for microdosimetric effects, as described in Section III.3.2 and summarized in Table III.3.1. However, the boron distribution within the tumor is still assumed to be uniform, with a constant 50 ppm across all cells and compartments. Finally, the solid red curve (*Micro Model*), represents the scenario where both the corrected radiobiological parameters from Table III.3.1 and a heterogeneous boron distribution in tumor cells and compartments are considered. In this case, the expected value of the photon isoeffective dose was calculated using Equation III.1.22, where the probability density function $f_A(a)$ corresponds to the experimental distribution obtained from U-87 neutron autoradiography as shown in Section III.2.4.

	Macro [Gy (IsoE)]	**Macro [RB-Corrected] [Gy (IsoE)]**	**Micro [Gy (IsoE)]**
D_{max}	37.6	27.0	36.1
D_{min}	28.5	20.3	27.3
D_{mean}	34.2	24.6	32.8

Table III.4.1: *Maximum, minimum and mean photon isoeffective dose values in the tumor (GTV), calculated with the Micro Model, Macro [RB-Corrected]and Micro Model respectively.*

	Percentage difference [%]		
	Macro VS Micro	**Macro VS Macro [RB-Corrected]**	**Micro VS Macro [RB-Corrected]**
Max	4	28	25
Min	4	29	26
Mean	4	28	25

Table III.4.2: *Percentage difference of maximum, minimum and mean photon isoeffective dose values in the tumor, calculated with the Micro Model, Macro [RB-Corrected] and Micro Model respectively.*

The photon isoeffective dose values calculated for the GTV using the three approaches are summarized in Table III.4.1, with relative differences shown in Table III.4.2. The *Macro Model*, which assumes a uniform boron distribution and uncorrected radiobiological parameters, yields the highest dose estimates (mean:

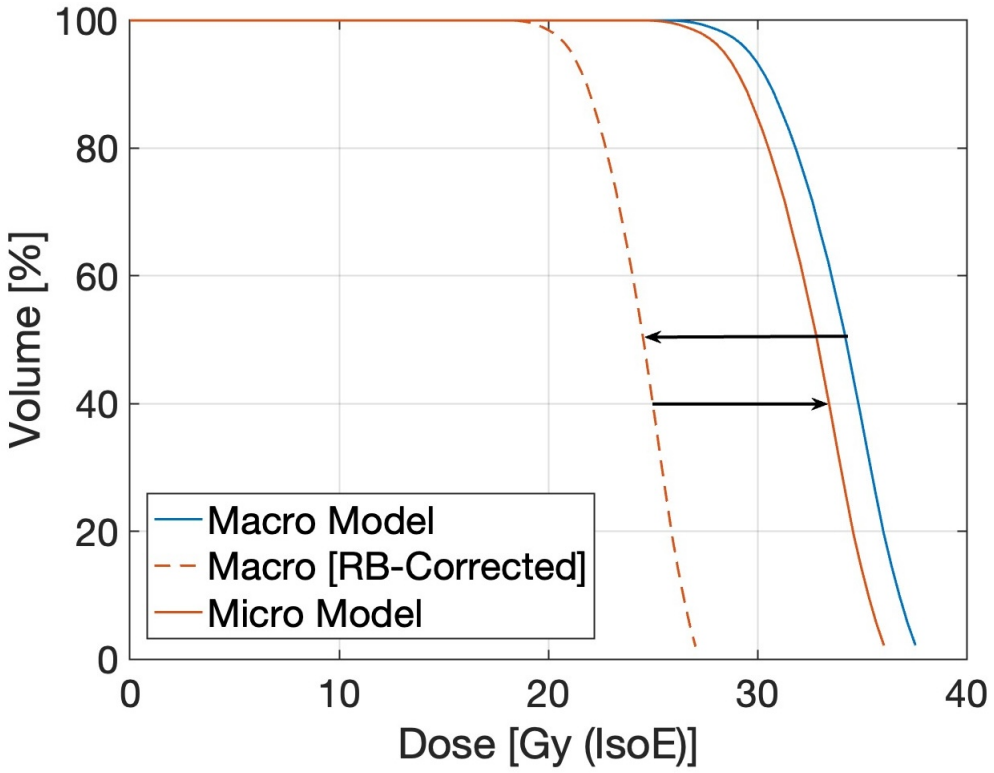

Figure III.4.1: *Dose Volume Histograms in which the dose in the GTV was calculated using three different approaches: in blue, the curve calculated with the macroscopic model; in red, the curve calculated with the microscopic model; in dashed red, the curve obtained using the radiobiological parameters corrected for microdosimetric effects but applied assuming a uniform boron distribution in the tumor of the patient.*

34.2 Gy (IsoE)). The *Macro [RB-Corrected]* approach, which uses parameters corrected for microdosimetric effects while still assuming homogeneous boron uptake in the tumor, leads to the lowest dose values (mean: 24.6 Gy (IsoE)). This decrease is consistent with the effects described above: correcting the radiobiological experiment for incorporating subcellular-scale effects reduces the α_B, thereby lowering the predicted dose. The *Micro Model*, which incorporates both corrected parameters and heterogeneous boron distribution in the tumor cells derived from neutron autoradiography in U-87 cells, produces intermediate results (mean: 32.8 Gy (IsoE)). In this case, the application of the η' factor to the calculation in the boron dose in the tumor compensate for the reduction in α_B, Resulting in doses closer to those of the Macro Model.

To further investigate how dosimetric outcomes are affected by key assumptions, a sensitivity analysis was carried out. Specifically, considering that in U-87 cells the nucleus volume accounts for approximately 2% of the total cell volume, the influence of variations in the nucleus-to-cell volume fraction v on the dose was investigated, while keeping the total cell volume and macroscopic boron concen-

tration constant. The values tested for v were 0.02 (U-87 case), 0.2, 0.6 and 0.94. The corresponding DVHs are shown in Figure III.4.2. The results show that, as the nuclear volume increases, the dose distribution gradually tends to approach the one obtained with the *Macro Model*. This trend is expected because, as the nucleus becomes larger, while the total cell volume remains fixed, boron concentration within the nucleus tends to approach the macroscopic value. In the limiting case where the entire cell is composed of nucleus, the scenario becomes equivalent to a tumor consisting of a continuous distribution of cells with 50 ppm, which corresponds exactly to the assumption made in the *Macro Model*.

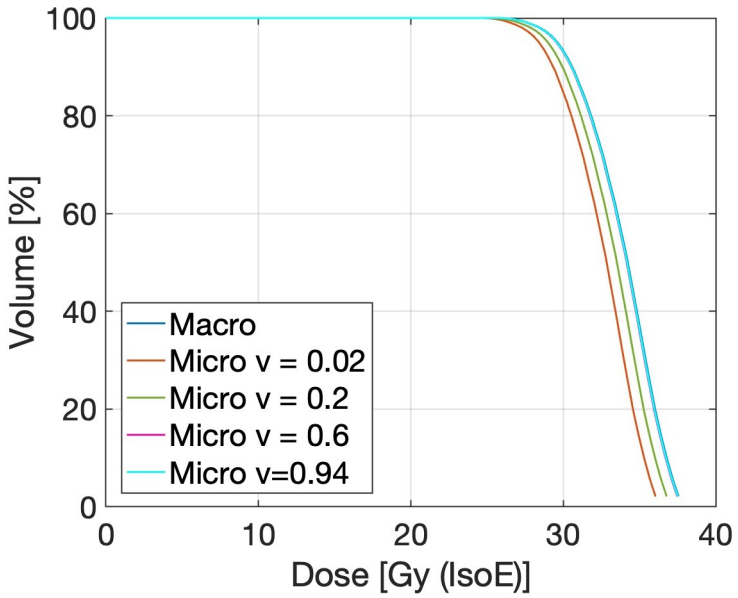

Figure III.4.2: *Dose Volume Histogram obtained with the Micro model, in which the value of the nucleus-to-cell volume fraction v was varied.*

An additional analysis was performed by varying the probability distribution of the cytoplasm-to-nucleus boron ratio a at the cellular level, assuming that within the tumor, such uptake might differ from that observed in the U-87 line. While the lognormal density function and the expected value of the cytoplasm-to-nucleus boron ratio a were maintained, different levels of variability were explored by modifying the standard deviation. Specifically, two additional distributions were considered: one with half the standard deviation of the U-87 case $\left(\frac{1}{2} \cdot \sigma_{\text{U-87}}\right)$ and one with twice the standard deviation $(2 \cdot \sigma_{\text{U-87}})$. The results were compared with those obtained using the original U-87-derived distribution, as shown in Figure III.4.3.

Figure III.4.3 reveals that varying the standard deviation σ in the lognormal distribution of the cytoplasm-to-nucleus boron ratio, while keeping the expected value constant, has a significant impact on the dose distribution in patient. In particular, in the case with $\sigma = \frac{1}{2} \cdot \sigma_{\text{U-87}}$ (light blue curve in the figure), a more concentrated distribution around the mean value is observed, resulting in a more homogeneous dose distribution and, consequently, a DVH more similar to that obtained with

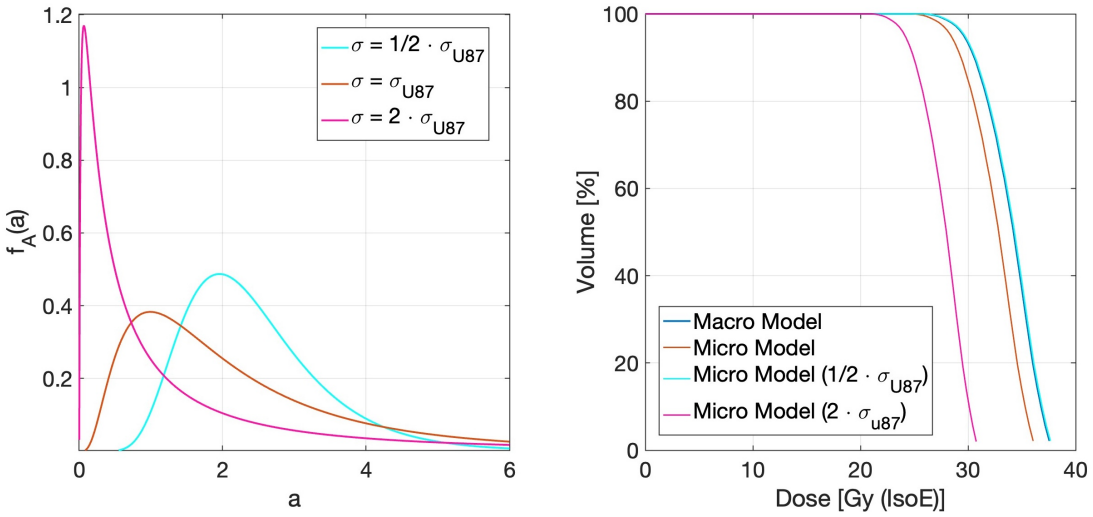

Figure III.4.3: *Left: probability densities $f_A(a)$ used in the calculations, in which the values of μ and σ of the distribution were varied, keeping the expected value of a constant and assuming σ equal to $\frac{1}{2}$ and 2 σ_{U-87}. Right: the corresponding Dose Volume Histograms obtained with the microdosimetric isoeffective photon dose model, in which the probability densities were changed.*

the *Macro Model* (blue curve). In contrast, increasing the standard deviation to $2 \cdot \sigma_{U-87}$ (curve in purple) widens the distribution considerably: some cells receive a much higher dose, while others receive less. This heterogeneity is reflected in a significant departure between the DVHs calculated with the *Macro Model* and the *Micro Model*, with a difference of about 22 %.

Overall, despite these variations, the comparison between the corrected model (*Micro Model*) and the original one (*Macro Model*) shows only a 4% difference in the clinical scenario considered, suggesting that the impact on treatment planning remains limited.

However, neglecting microdosimetric considerations can lead to inaccurate interpretations of treatment effectiveness. The similarity of the outcomes between the two models emerges not because the microdosimetric considerations and stochastic effects are irrelevant, but because both boron heterogeneity and parameter correction were consistently integrated. On the other hand, when dose is calculated in the tumor using the *Macro [RB-Micro] model*, which uses the corrected radiobiological parameters, but considers uniform boron concentration, the result is 28% lower than the *Macro Model*.

As mentioned in the Introduction, one-year Progression-Free Survival (1y-PFS) can serve as a clinical indicator of treatment efficacy. In light of the dosimetric differences discussed above, the following Part presents a biophysical model based on 1y-PFS.

Through this model, derived from data of patient treated with photon, it will be possible to quantify the expected clinical impact of the dose changes presented in

these Chapters.

Part IV

From dosimetry in cells to dosimetry in patients

CHAPTER IV.1

PROGRESSION FREE SURVIVAL MODEL

Glioblastoma Multiforme is a challenging tumor to treat, not only because of its peculiar clinical features, as presented in Chapter I.1, but also due to the difficulty in predicting and describing the therapeutic effect.
Overall Survival, OS, represents the most robust endpoint for assessing the efficacy of a treatment, as it measures the time until the patient's death, regardless of the progression of the malignancy. In the case of GBM, OS is influenced by many factors, such as age, previous surgery, and general condition.
A possible alternative to OS is **Progression Free Survival, PFS**, which is considered a surrogate endpoint for OS. The advantage of PFS is that it allows for more rapid assessment of treatment efficacy, regardless of the lifespan after the treatment.
Because of the uncertainties and complexities associated with estimating tumor volume control, in some situations PFS and OS may serve as more clinically meaningful endpoints than Tumor Control Probability, TCP.
One factor that complicates the calculation of TCP is the formation, following therapy (radiotherapy or chemotherapy), of vasogenic edema or pseudoprogressive necrosis, conditions that make it challenging to distinguish residual tumor tissue from the inflammatory reaction in the medical images. Vasogenic edema develops when the blood-brain barrier, which has the function of isolating the central nervous system from the bloodstream, loses its integrity due to increased permeability or rupture of endothelial cells. This phenomenon results in the leakage of substances such as fluids and plasma proteins, leading to accumulation in the surrounding brain tissue. Pseudoprogressive necrosis, on the other hand, consists of an apparent increase in tumor mass that does not represent disease progression but is due to a transient inflammatory and necrotic reaction following treatment. Consequently, if the tumor is not distinguishable, it becomes difficult to quantify the dimensions of the tumor after the treatment, thus leading to a possible

overestimation or underestimation of tumor control. Because of impossibility to discriminate between tumor tissue and edema, PFS and OS are preferred figures of merit in clinical trials, as they represent easier and more direct endpoints to measure.
In BNCT treatment planning, it is crucial to adopt figures of merit that not only estimate the percentage of controlled lesions but also provide reliable predictions of clinical outcomes.
In the previous Parts, both the macrodosimetric isoeffective photon dose model for GBM and the microdosimetric model, which integrates the subcellular-scale effects, have been described.
This part of the work is dedicated to a figure of merit specifically tailored to BNCT for GBM, designed to evaluate, compare, and assess the performance of the dose calculation models developed in this thesis. Consequently, the presented results provide a tool that, with sufficient future validation, may also serve as a predictor of clinical outcome.
Currently, no established figure of merit is available for GBM treated with BNCT. Given the difficulty in estimating the probability of tumor control in this tumor, due to the factors previously discussed, a *1-year Progression-Free Survival* model derived from clinical photon treatments was adopted in this study and subsequently adapted for BNCT. This choice is justified by the fact that the use of the photon isoeffective dose allows the BNCT dose to be translated into photon equivalent units; moreover, previous studies have validated this approach in other tumor types [67].
The *1-year Progression-Free Survival* (1y-PFS) model, described in [166], is based on the concept of cell survival, already introduced in Equation I.3.4 of Chapter I.3, and described by the Linear-Quadratic model.
In [166], clinical data were selected from patients with GBM and treated with *photon external beam radiotherapy*. Specifically, patients underwent a fractionated radiotherapy regimen with a total dose to the tumor ranging from 45 to 70 Gy, divided into 15 to 30 fractions with a dose per fraction ranging from 2.3 to 3 Gy.
In a fractionated regimen, in which the tumor is given a total dose D divided into n fractions, each of dose d such that $D = n \cdot d$, cell survival $S(D)$ is defined as

$$S(D) = e^{-D(\alpha+\beta d)+\frac{\ln 2}{T_d}(T-T_k)}, \tag{IV.1.1}$$

where α and β are the radiobiological parameters of photons: α represents the intrinsic radiosensitivity of the neoplasm, while β describes the repair capacity of sublethal damage. The parameter T_d indicates the re-population doubling time, T_k represents the kick-off time for tumor re-population, and T corresponds to the overall treatment time (OTT).
From the clinical data, the authors estimated the radiobiological parameters of the 1y-PFS model, which can be described by Equation IV.1.2, under the assumption that cell death events follow a Poisson probability distribution.

$$PFS = e^{-NS(D)} = e^{-N\cdot e^{-D(\alpha+\beta d)+\frac{\ln 2}{T_d}(T-T_k)}}, \tag{IV.1.2}$$

where N represents the number of clonogens for a given regimen of fractionation. Table IV.1.1 shows the values obtained by the authors from the fit of clinical data. Confidence intervals refer to a confidence level of 95%.

1y - PFS estimated parameters estimated in [166]			
α	0.12 [0.10 - 0.14] Gy^{-1}	T_d	15 [13.2 - 19.5] dasys
β	0.015 [0.013 - 0.020] Gy^{-2}	T_k	37 [29 - 46] days
$\frac{\alpha}{\beta}$	8 [5.0 - 10.8] Gy	N	$9.1{\cdot}10^3$ [$4{\cdot}10^3$ - $2.1{\cdot}10^4$] clonogens

Table IV.1.1: *The best estimated parameters for 1y - PFS model and their uncertainty intervals refer to a confidence level of 95% from [166].*

The model described was adapted to the context of BNCT, in which the treatment involves a single administration and not a fractionated regimen.
For the translation from the fractionated model to the single fraction model ($n = 1$), the concept of *Biologically Effective Dose* (BED) was introduced, which represents the measure of the biologically effective dose released from multiple dose fractions d, for a total dose D, in a given tissue characterized by a ratio α/β. The latter describes the biological response of a tissue to ionizing radiation based on dose fractionation. BED is a fundamental concept in radiation oncology, as it allows comparison of different treatment plans or different fractionation schemes. In the general case of n fractions, BED_n is defined as:

$$BED_n = -\frac{\ln(S)}{\alpha} = nd\left(1 + \frac{d}{\alpha/\beta}\right) - \frac{\ln 2}{T_d}(T - T_k)\,. \tag{IV.1.3}$$

In the case where the treatment involves a single fraction, with a dose D_{SF} the BED_1 results described by

$$BED_1 = -\frac{\ln(S)}{\alpha} = D_{SF}\left(1 + \frac{D_{SF}}{\alpha/\beta}\right). \tag{IV.1.4}$$

The 1y-PFS model, defined for a fractional regime by Equation IV.1.2, can be adapted to a single fraction model by considering that $BED_n = BED_1$, as follows

$$PFS_{SF} = e^{-NS(D)} = e^{-Ne^{-\alpha BED_n}} = e^{-Ne^{-\alpha BED_1}} = e^{-Ne^{-\left(\alpha D_{SF} + \beta D_{SF}^2\right)}}, \tag{IV.1.5}$$

where the parameters α and β are are those reported in Table IV.1.1.
The available clinical data from [166] of 1y-PFS, as a function of delivered dose, are also converted to the case of single fraction dose ($n = 1$), as shown in Figure IV.1.1. Figure IV.1.1 reproduces the results reported by Pedicini et al in [166]. In their study, the clinical data expressed in terms of single-fraction dose were divided into two sets: one (blue circles) used to fit the *1-year Progression-Free Survival* model, and the other (red circles) used as an independent validation subset. The resulting model, shown as a black line, corresponds to the fit performed by Pedicini et al. The validation strategy adopted by Pedicini et al. was twofold. First, the position of the mean normalized slope for PFS = 0.5 (γ_{50}) was verified to lie within

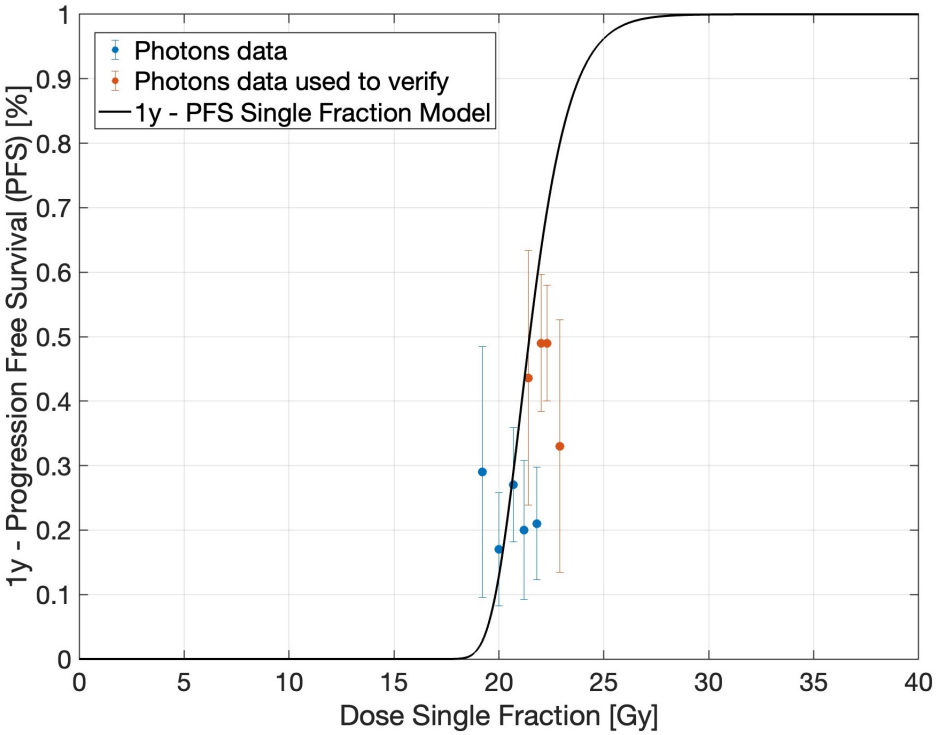

Figure IV.1.1: *1 year - Progression Free Survival Model for GBM as a function of the delivered single fraction photon dose (black curve). Blue circles are the data used for the fit while red circles the one used to verify the model. The data uncertainties correspond to a 95% confidence interval. Data from [166].*

the clinically relevant range [167, 168]. Second, the analysis was repeated using the independent validation subset to test the robustness of the fitted curve. In addition, uncertainties estimated via Greenwood's formula and propagated to all model parameters were compared with those obtained through a bootstrap resampling procedure (600 resampled datasets with fixed censoring). This approach allowed the authors to assess the consistency and stability of the model.

In the context of BNCT, the 1-yPFS given by expression IV.1.5 can be applied by using the corresponding photon isoeffective dose, calculated either from the macro- or from the microdosimetric model.

However, unlike conventional photon radiotherapy—where the dose delivered to the tumor is nearly uniform—in BNCT the dose distribution varies throughout the tumor volume. This raises the need to define a single representative value of the BNCT dose distribution in order to apply the 1y-PFS single-fraction model.

The BNCT dose distribution can be described by the *Equivalent Uniform Dose* (EUD), defined as the uniform dose in a given volume that produces the same biological effect as the dose actually delivered non-uniformly [169].

Assuming that the tumor is divided into N_v subregions in which the dose is uniform and equal to D_i (with $i = 1, \ldots, N_v$) and denoted by v_i the corresponding

volume fraction, the EUD can be expressed as

$$\mathrm{EUD} = \left(\frac{1}{N_v} \sum_{i=1}^{N_v} v_i D_i^{-a} \right)^{-\frac{1}{a}}, \tag{IV.1.6}$$

where a is an organ-specific parameter considered, in this case the tumor.
This formulation represents an adaptation proposed in this thesis of the original concept introduced in [169], specifically tailored to describe the tumor response. The parameter a was calculated from data of nine patients with GBM, treated with BNCT in Finland[1] [145, 170]. For all nine Finnish patients, the absorbed dose distributions within the tumor were available from treatment planning. Based on the distributions of absorbed dose, the Photon Isoeffective Dose Model distribution was calculated for each patient using the proposed macro model. Subsequently, the 1-yPFS was reformulated in terms of the EUD.
The model parameter a was then estimated by maximum likelihood, i.e., the value of a that maximizes the probability of reproducing the clinical responses observed in the nine patients. One of the nine patients was progression-free at one year. The expression of 1y-PFS for single fraction given in Eq. IV.1.5 can be rewritten as a function of EUD by substituting D_{SF} for EUD, obtaining:

$$PFS = e^{-Ne^{-(\alpha\,\mathrm{EUD}+\beta\,\mathrm{EUD}^2)}}, \tag{IV.1.7}$$

where EUD is defined by Eq. IV.1.6.
Define the observed *outcome* for the patient i as y_i, with

$$y_i \in \{0, 1\},$$

where $y_i = 1$ indicates one-year free progression and $y_i = 0$ disease progression in 1 year. The probability predicted by the model for patient i is given as $p_i = PFS_i$. This corresponds to the standard Bernoulli likelihood for binary outcomes.
For independent data, the likelihood function of the parameter a results

$$\mathcal{L}(a) = \prod_{i=1}^{9} p_i^{y_i} \, (1 - p_i)^{1-y_i}, \tag{IV.1.8}$$

where p_i depends implicitly on a through EUD.
It is then possible to estimate a by minimizing the minus log-likelihood:

$$-\ell(a) = -\log \mathcal{L}(a) = -\sum_{i=1}^{9} \left[y_i \, \log(p_i) + (1 - y_i) \, \log(1 - p_i) \right]. \tag{IV.1.9}$$

The minimization of the log-likelihood allowed us to estimate the parameter.

$$a = 237 \; [232, \, 238] \quad (95\% \text{ C.L.}).$$

[1] We greatly acknowledge the Finnish group for kindly providing patient data within the framework of the BNCT collaboration which enabled the setup of the PFS model.

To assess the goodness of fit, a statistical test based on Monte Carlo resampling was performed. Under the null hypothesis that the observed outcomes are consistent with the probabilities predicted by the model, 10^7 random realizations of the dataset were generated. The p-value was then computed as the fraction of realizations in which the discrepancy between observed and predicted responses was at least as large as the one found in the actual data. The resulting p-value was found to be greater than the significance threshold ($\alpha = 0.01$), indicating that the observed differences between model predictions and clinical data can be attributed to statistical fluctuations. Therefore, the null hypothesis of consistency *cannot be rejected*, and the model is statistically compatible with the available data.
Figure IV.1.2 shows the 1-year progression-free survival (1y-PFS) model curve as a function of dose (black line) and the predicted 1y-PFS for the nine Finnish patients. Triangles indicate the actual clinical outcome: filled triangles for patients who progressed within one year, and open triangles for patients who remained progression-free. The model assigns a low 1-year PFS to patients who progressed at 1 year and a high probability to the patients who did not. The total number of patients predicted to be progression-free at 1 year is close to one, in agreement with the clinical outcome (1 out of 9).

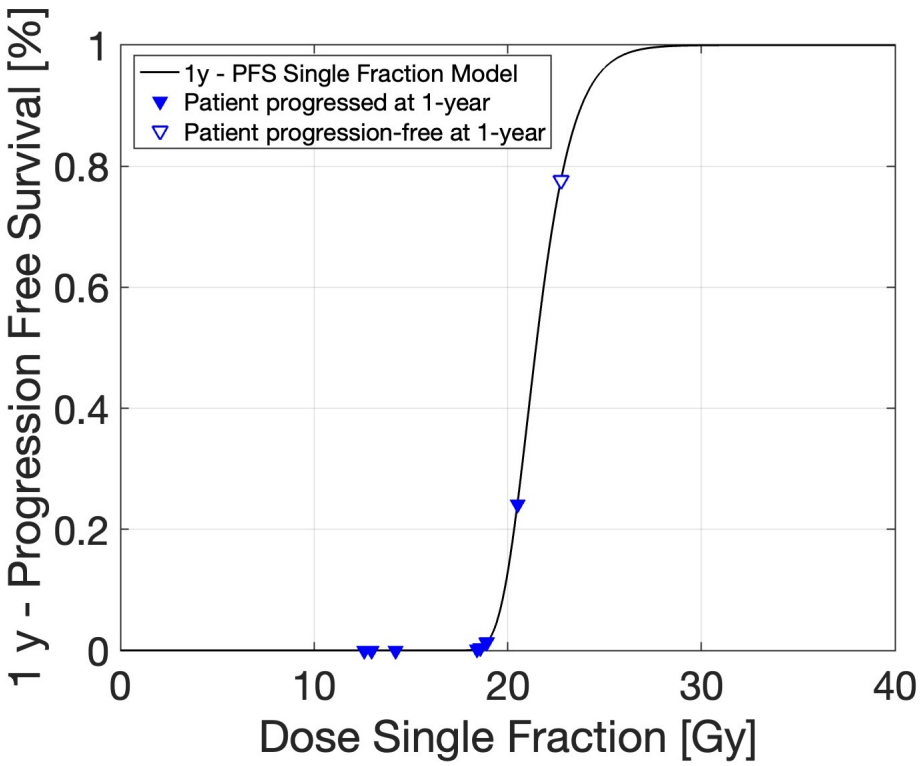

Figure IV.1.2: *Black curve model of 1-year Progression-Free Survival for single fraction. Triangles indicate the actual clinical outcome of Finnish patients: filled triangles represent patients who progressed within one year, and open triangles represent patients who were progression-free at one year.*

IV.1.1 Application of the 1-year PFS Model

The 1-year Progression-Free Survival model described above can be used as a figure of merit to assess the clinical relevance of the dosimetry differences observed in the clinical case presented in Chapter II.3. Figure IV.1.3 shows the PFS model (black curve) and the values obtained for the three models analyzed: red rhombus for the *Macro Model*, yellow triangle for the *Macro [RB-corrected] Model*, and purple square for the *Micro Model*. The calculated PFS values were 0.99 for the *Macro Model*, 0.02 for the *Macro [RB-corrected] Model*, and 0.97 for the *Micro Model*. These results reflect the same trends observed in the dosimetry estimates: a 98% difference between the *Macro/Micro Model* and the *Macro [RB-corrected] Model*, and a 2% difference between the Macro and Micro Models.
The green circle in Figure IV.1.3 represents the value of the 1-year PFS obtained when the tumor dose is calculated with the *Micro Model*, modeling the variable a with a lognormal distribution having the same expected value but twice the standard deviation of that measured in the U-87 cells ($\sigma = 2 \cdot \sigma_{U-87}$). In this scenario, the 1y - PFS value is 0.84, a reduction of 15% compared to the *Macro Model*.

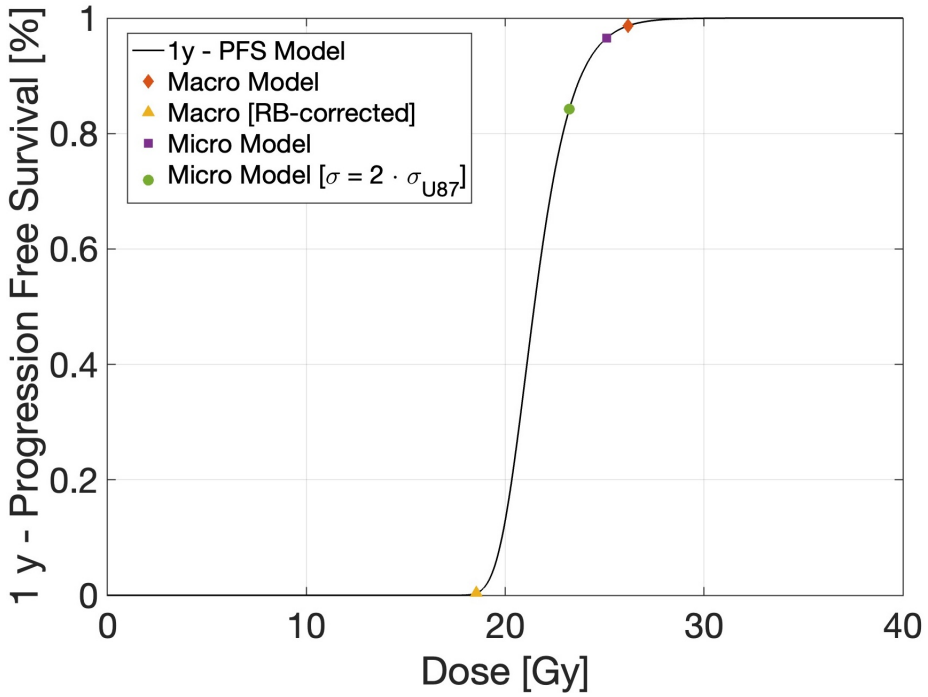

Figure IV.1.3: *Black curve model of 1-year Progression-Free Survival for single fraction and corresponding values for the three dosimetric models: Macro (red rhombus), Macro [RB-corrected] (yellow triangle), Micro (purple square), and Micro Model with $\sigma = 2 \cdot \sigma_{U-87}$ (green circle).*

The application of clinical dose–response models originally developed for photon radiotherapy to BNCT requires the introduction of a photon-equivalent dose con-

cept, in order to express the complex mixed radiation field of BNCT within a conventional radiotherapy framework. This conversion is intrinsically challenging, as BNCT involves different radiation components (boron reaction products, protons from thermal and fast neutron interactions and gamma rays), each characterised by a different biological effectiveness and by a highly heterogeneous spatial and subcellular dose distribution. Consequently, the derivation of a dose in photon-equivalent units relies on radiobiological models based on *in vitro* and *in vivo* experimental data, which currently represent the most established approach for relating BNCT doses to clinical photon experience. Despite these efforts, uncertainties remain in the conversion process. These stem not only to the complexity of the BNCT radiation field and from the assumptions underlying the radiobiological weighting factors, but also to the intrinsic uncertainties and limitations of the photon-based dose–response models themselves. In addition, BNCT dose distributions are typically more heterogeneous within the target volume and are often delivered in a single fraction. These characteristics further differentiate BNCT from conventional fractionated photon radiotherapy and may affect the applicability of standard dose–effect relationships. Nevertheless, in the absence of large and comprehensive BNCT-specific clinical datasets, the use of photon-based clinical models combined with the best available radiobiological conversion methods currently represents the most practical and clinically meaningful approach to estimate treatment outcomes in BNCT. This strategy allows BNCT results to be interpreted within a well-established clinical framework, while acknowledging that further improvements are expected as more dedicated clinical data become available.

CHAPTER IV.2

APPLICATION OF THE MODELS ON REAL CLINICAL CASES TREATED WITH BNCT

This Chapter presents the application of the developed dose models and the *1-year Progression-Free Survival* framework to two clinically representative cases of Glioblastoma Multiforme patients treated with Boron Neutron Capture Therapy in the Xiamen Humanity Hospital, in Xiamen, China.
Both patients underwent diagnostic imaging using CT and PET with ^{18}F-BPA before treatment. The latter was subsequently used to correct the dose component from boron, in relation to the heterogeneous distribution of boron in the tumor volume at the macroscopic level, as reported in [146].
The patients received the boron infusion about two hours before irradiation and, throughout the treatment, a continuous infusion.
For patient 1, the irradiation time was determined by imposing as a constraint that the brain received an average dose of 3 Gy (RBE). For patient 2, on the other hand, the irradiation time was calculated by limiting the dose to the brain but imposing that the minimum equivalent dose was 15 Gy (RBE).
The dosimetry of both patients was based on the RBE-weighted dose model described in Chapter I.3.1, which accounts for the different radiation quality components. In these calculations, a Compound Biological Effectiveness (CBE) factor of 1.3 was adopted for the boron dose, and a Relative Biological Effectiveness (RBE) of 3.2 was used for the neutron component, consistent with the clinical protocol.
The resulting irradiation times were 31.8 min and 41.8 min, respectively.
A retrospective study was conducted in which the three models (the *Macro Model* described in Chapter II.1, the *Micro Model* presented in Chapter III.1, and the *Macro [RB-corrected] Model*, in which radiobiological parameters corrected by taking into account microdosimetric considerations are employed in the macro model) were applied to both patients.

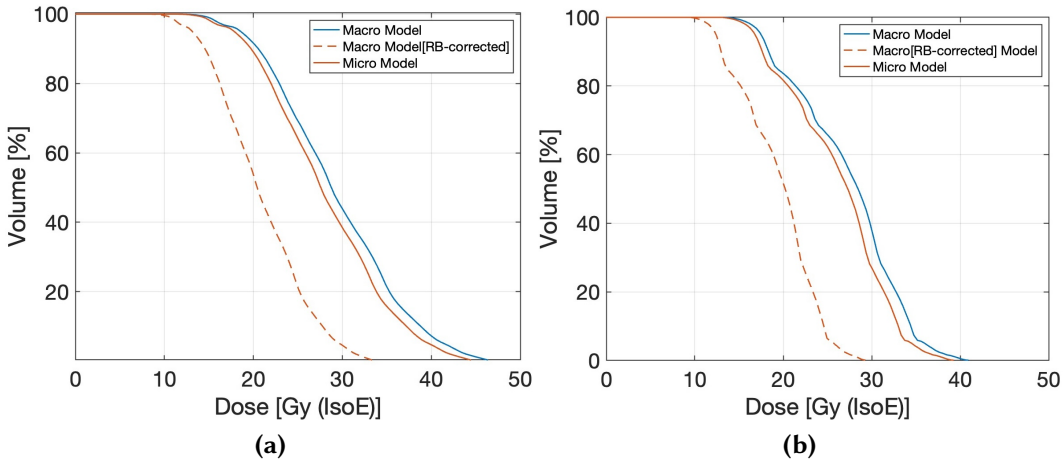

Figure IV.2.1: *Dose Volume Histograms in which the dose in the GTV was calculated using three different approaches: in blue, the curve calculated with the macroscopic model; in red, the curve calculated with the microscopic model; in dashed red, the curve obtained using the radiobiological parameters corrected for microdosimetric effects but applied assuming a uniform boron distribution in the tumor of the patient. a) Patient 1. b)Patient 2.*

The methodological novelty introduced is that, unlike the approach in the clinical case presented in II.3, in which a constant macroscopic boron concentration is assumed, in this case PET images with ^{18}F-BPA were used to partition the tumor volume into groupwise. Each group was associated with a specific value of ^{10}B concentration, based on the information provided by the PET scan, as extensively described in [146]. This adds a level of accuracy in estimating the dose distribution.

The results for the minimum, mean, and maximum absorbed dose values are shown for Patient 1 in Table IV.2.1 and for Patient 2 in Table IV.2.2, with relative differences shown respectively in Table IV.2.3 and IV.2.4.

Figure IV.2.1 shows the dose-volume histograms (DVHs): on the right, those of Patient 1 and on the left those of Patient 2. Specifically, the blue curves correspond to the macrodosimetric model, the red curves to the microdosimetric model, and the dashed red curves represent the macrodosimetric model with corrected radiobiological parameters.

The results obtained in these real cases are consistent with those reported in Chapter III.4 for the simulated irradiation of a GBM patient using RFQ epithermal beam designed for BNCT. In particular, the differences between the Macro and Micro models are about 4% both for the two Chinese patients analyzed and for the simulated patient described in Chapter III.4. The differences between the Macro model and the Macro [RB-corrected] model, as well as between the Micro model and the Macro [RB-corrected] model, remain more pronounced, with values of 28% and 26%, respectively, in line with what was observed previously (28% and 25%).

	Macro [Gy (IsoE)]	Macro [RB-Corrected] [Gy (IsoE)]	Micro [Gy (IsoE)]
D_{max}	47.7	34.3	46.8
D_{min}	11.4	8.1	11.0
D_{mean}	29.2	20.8	28.0

Table IV.2.1: *Maximum, minimum and mean photon isoeffective dose values in the tumor, calculated with the Macro Model, Macro [RB-Corrected]and Micro Model respectively.*

	Macro [Gy (IsoE)]	Macro [RB-Corrected] [Gy (IsoE)]	Micro [Gy (IsoE)]
D_{max}	41.4	29.7	39.7
D_{min}	13.6	9.5	13.1
D_{mean}	27.3	19.4	26.2

Table IV.2.2: *Maximum, minimum and mean photon isoeffective dose values in the tumor, calculated with the Macro Model, Macro [RB-Corrected]and Micro Model respectively.*

	Percentage difference [%]		
	Macro VS Micro	Macro VS Macro [RB-Corrected]	Micro VS Macro [RB-Corrected]
Max	2	28	27
Min	4	29	26
Mean	4	29	26

Table IV.2.3: *Percentage difference of maximum, minimum and mean photon isoeffective dose values in the tumor, calculated with the Macro Model, Macro [RB-Corrected]and Micro Model respectively.*

	Percentage difference [%]		
	Macro VS Micro	Macro VS Macro [RB-Corrected]	Micro VS Macro [RB-Corrected]
Max	4	28	25
Min	4	29	26
Mean	4	30	27

Table IV.2.4: *Percentage difference of maximum, minimum and mean photon isoeffective dose values in the tumor, calculated with the Macro Model, Macro [RB-Corrected]and Micro Model respectively.*

This consistency indicates that the results do not depend on the specific clinical case. The first analyzed case was never treated with BNCT; the irradiation was simulated with a simplified criterion, using a designed neutron beam. These two

last patients actually received treatment in China, and their treatment plan was optimize for the maximum clinical efficacy. In addition, the latter cases involved an extra level of complexity due to the non-uniform macroscopic distribution of boron concentration derived from PET data.
A potential future development would be to go beyond the regions approximation for boron distribution in tumor, and directly define boron concentration voxel-by-voxel from PET images. Thereby, this would enable an even more accurate assessment of the heterogeneity of boron concentration at the macroscopic level and, consequently, a refined calculation of the photon isoeffective dose.
The 1y-PFS was calculated for both patients analyzed and was zero in all three dosimetric models considered. This result is because the curve, as shown in Figure IV.1.1, only starts to differ from zero at doses above approximately 17 Gy. In all three cases, for both patients, the EUD was less than 17 Gy (see Table IV.2.5).
As for the clinical outcome, it is only available for the first patient, who presented disease progression approximately 7 months after treatment, in accordance with the 1-year PFS value of zero. The second patient, on the other hand, was lost to follow-up after treatment [1].
It is important to emphasize that the availability of clinical data is crucial for this type of innovation in dosimetry applied to BNCT. Without it, it is not possible to robustly validate dosimetric models and correlate them with the therapeutic efficacy or toxicity of the treatment.

	EUD [Gy (IsoE)]		
	Macro Model	*Macro [RB-corrected] Model*	*Micro Model*
Patient 1	11.9	8.4	11.5
Patient 2	14.16	9.9	13.6

Table IV.2.5: *EUD (Equivalent Uniform Dose) values for the two patients analyzed, calculated according to three models: Macro Model, Macro[RB-corrected] Model, and Micro Model.*

The photon isoeffective dose model can play a critical role in BNCT treatment decisions by improving the accuracy of biologically equivalent dose estimation for both tumour and healthy tissues. As BNCT irradiation time is usually dictated by the tolerance thresholds of healthy tissue, a more accurate calculation of the equivalent dose can have a direct impact on treatment duration and overall safety. Accurate estimation of the isoeffective dose helps avoid overestimating tumour dose, which could lead to unrealistic expectations for local control, or underestimating the dose to healthy tissues, which may increase the risk of toxicity. However, it should be noted that the aim of this study is to evaluate whether the incorporation of experimentally observed subcellular heterogeneity of boron and stochastic energy deposition affects radiobiological interpretation and estimates

[1] We would like to thank Professor Pan and Professor Liu of Xiamen Humanity Hospital, as well as their team, for sharing the patient data that contributed to this research.

of the photon isoeffective dose. Although an isoeffectiveness model for healthy brain tissue is available in the literature [170], based on the probability of grade III or higher somnolence syndrome, this model was not applied to the clinical cases analysed in this thesis. The aim of this study was not to replace the clinical prescription criteria currently in use, but to provide an advanced microdosimetric tool for a more realistic estimation of the isoeffective dose. The direct integration of healthy tissue toxicity models into the Micro Isoeffective Model represents a natural future development of this research, which is expected to further strengthen its clinical relevance.

CONCLUSIONS

Glioblastoma Multiforme (GBM) represents one of the most aggressive and difficult to treat neoplasms, with an unfavorable prognosis. Standard of care involves, when possible, surgery followed by post-operative radiation therapy in combination with concomitant and adjuvant chemotherapy based on the alkylating agent temozolomide. This combined approach increased the median survival of patients compared with radiotherapy alone, an outcome that remains clinically unsatisfactory nonetheless. There is thus an urgent need to develop alternative and more effective therapeutic strategies to improve the prognosis of patients with GBM. In this context, Boron Neutron Capture Therapy emerges as a promising approach, providing a tumor-selective form of particle irradiation.

This thesis aimed at deepen the capacity to deliver a safe and effective BNCT to patient affected by GBM by improving the dose calculation and developing proper methods to connect radiobiological effects with physical quantities. Dosimetry in BNCT is complex, because of its mixed radiation field, that prevents a direct comparison with conventional radiotherapy. To account for the different radiobiological effect of the dose components of the mixed field, BNCT dose is translated into photon equivalent units to predict the clinical outcome.

This thesis tackles the necessity of implementing an appropriate model for photon equivalent dosimetry in BNCT for GBM. A robust model is crucial for explaining retrospective clinical outcomes in view of their dosimetry and predicting the therapeutic effectiveness of treatment planning for future clinical trials.

The first important result concerns the influence of the selected photon reference radiation on the calculation of the radiobiological parameters needed to feed the dose model. Two photon sources for radiobiological experiments were used: a standard 160 kVp X-ray irradiator and a ^{60}Co irradiation facility, a source with higher energy, more comparable to that of clinical photon therapy (orders of few MeV). The obtained survival curves as a function of the dose were significantly different. When used to evaluate the Relative Radiobiological Effectiveness (RBE) and Compound Biological Effectiveness (CBE) at 1% survival, the two photon sources yielded differences of 44% and 37% respectively. When choosing the reference radiation to produce radiobiological parameters for the photon equivalent

dose calculation, it is important to select a photon energy as close as possible as the radiation therapy beams. In fact, when the photon equivalent dose in BNCT is calculated using low energy X-rays as the reference radiation, the resulting BNCT dose does not accurately reflect the effect achieved by clinical photons.

Orthovoltage X-rays are used in this work exclusively to probe the dependence of the radiobiological parameters on radiation quality within the isoeffective dose formalism, and not as an attempt to model clinical or BNCT photon fields.

The impact of the radiobiological system selected to construct the Photon Isoeffective Dose Model on BNCT treatment planning was assessed in a GBM patient case. Clinical BNCT dosimetry for GBM traditionally relies on factors derived from *in vivo/in vitro* experiments on the rat 9L gliosarcoma (GSM) cell line. While radiobiological data on this tumor are available in the literature, data specific to human GBM were missing. Importantly, GBM and GSM are now recognized as biologically and clinically distinct tumors, which further questions the appropriateness of extrapolating radiobiological parameters from GSM to GBM. A new set of radiobiological parameters was therefore produced using the U-87 human GBM cell line and incorporated into to the dosimetric models. The comparison with the existing parameters obtained from 9L GSM revealed significant differences: up to 31% in photon isoeffective dose and 45% in RBE-weighted dose. The doses calculated with the GBM-derived parameters resulted systematically higher than those obtained with the GSM-based set, showing the critical importance of selecting appropriate tumor-specific radiobiological models and the need of producing consistent data for each tumor type. The derivation of data specific to human GBM in this work represents a significant step forward for photon equivalent dosimetry. Future studies involving additional irradiation of GBM cell lines would further strengthen the clinical relevance of the model. Moreover, work on more realistic *in vitro* models such as tri-dimensional GBM spheroids is presently ongoing to integrate the aspects of cells interaction and heterogeneous boron distribution into the tumor in the radiobiological evaluations. The most complete radiobiological experiment will be the irradiation of small animals with GBM in order to derive dose–response data based on tumor control. However, while *in vivo* GBM models would provide an even closer link to clinical effects, such experiments are considerably more challenging. In this context, having achieved an adequate formulation based on *in vitro* data constitutes an important and novel contribution for BNCT of GBM. As previously done for head and neck cancer [67] and melanoma [38], the proposed dosimetric model should ultimately be validated through retrospective analyses of patients treated with BNCT for whom the clinical outcome is reported.

After the development of a proper Photon Isoeffective Dose Model for GBM, the work was then directed to explore the influence of the boron microdistribution in the nucleus and cytoplasm of cells. Most macroscopic approaches assume that ^{10}B is uniformly distributed at both the tissue and cellular scales. However, it is natural to question whether this assumption remains valid when moving to the subcellular scale. This insight into cells represents a paradigm shift in BNCT

dosimetry, as it raises the question of whether macroscopic dose is the correct physical quantity to associate with the biological effects observed. For the first time, this thesis proposes the inclusion of microdosimetric effects into the Photon Isoeffective Dose model for GBM. The first step of this development was the experimental characterization of boron distribution. Using the neutron autoradiography technique, the microdistribution of boron-10 in the two cellular compartments of the human GBM cell line was imaged and quantified. The results revealed a preferential accumulation of the borated molecule BPA in the nucleus compared with the cytoplasm, with nearly 2.4 times higher concentration. This finding was unexpected because it was against the common knowledge that the distribution of boron obtained with BPA should not be selective for nucleus. However, another recent work published by Chinese colleagues who produced boron distribution images at the subcellular level, confirmed this result [158]. The experimental evidence that boron is closer to the sensitive target of cell DNA, suggests that BNCT might be more effective as a function of the dose than what usually considered. Most importantly, these findings motivated the need to incorporate boron microdistribution into dosimetry models to improve the accuracy of clinical predictions in BNCT. To extend the Photon Isoeffective Dose Model, the formalism was integrated with the stochastic aspects of energy deposition related to the non-uniformity of boron concentration at the cellular level. The boron dose component was corrected using the factor $\eta'(a)$ which, integrated jointly with the probability density function of the nucleus-to-cytoplasm boron concentration ratio a, $f_A(a)$, takes into account (i) a correction for the stochastic nature of energy deposition due to intracellular boron localization, and (ii) the fact that the ratio a is a stochastic variable. Based on the analysis of the neutron autoradiography experimental data, the probability density function $f_A(a)$ was determined. The ratio a was proved to follow a lognormal distribution, consistent with the behavior of other biological processes where the uptake of substances is concerned. The correction factor was first applied to the dosimetry of U-87 radiobiological data, and its impact was analyzed through the calculation of CBE. The significant difference observed in $CBE_{1\%}$ with and without corrections to the U-87 cell survival parameters is consistent with previous findings, particularly in studies conducted on the 9L GSM rat gliosarcoma cell line [171]. In those experiments with BPA, CBE values were unusually high: 9.4 for 1 % survival. Subsequent analyses, however, revealed that the intracellular boron concentration was significantly higher than that used for dosimetric calculations, leading to an underestimation of the effective dose and, thus, an overestimation of the CBE [78].

It is important to note that the radiobiological parameters and models developed in this study were derived using a single Glioblastoma cell line. Although this is a widely used and well-characterised model, GBM is known to exhibit marked biological heterogeneity in terms of radiosensitivity and DNA repair. Consequently, the results obtained and the parameters estimated should be interpreted as specific to the cell line used and not immediately generalisable to the entire spectrum of GBM tumours.

At the same time, the model itself is not intrinsically restricted to the U-87 cell line. In principle, it can be fed with radiobiological input data obtained from other GBM cell lines, from other cell types, and also from patient-derived models, provided that the corresponding experimental characterisation is available and that the radiobiological parameters are re-estimated accordingly. This flexibility makes the proposed approach a general and extensible framework rather than a model tied to a specific biological system.
Extending this approach to multiple GBM cell lines, as well as to patient-derived models, is a natural and necessary next step in evaluating the robustness, intertumour variability, and true clinical transferability of the models developed in this study.

The observed heterogeneity in boron uptake in the U-87 cell line (especially between nucleus and cytoplasm) provides a biological basis for modeling variability at the cellular level, its translation to the tumor context remains uncertain. Nevertheless, it is reasonable to hypothesize that similar distributions may occur *in vivo*. The three models studied (*Macro, Micro and Macro[RB Corrected] models*) were designed to explore the impact of both radiobiological parameter correction and potential boron-10 distribution heterogeneity within tumor tissue.

The application of the Photon Isoeffective Dose model to a GBM clinical case highlighted the impact of microdosimetric aspects and heterogeneous boron distribution at the cellular level. Results show that the corrected model (*Micro Model*) and the original one (*Macro Model*) differ by only 4%, suggesting a limited impact in treatment settings.

This small difference, compared to the difference highlighted in radiobiological data, does not imply that microdosimetric considerations and stochastic effects are irrelevant. Rather, it reflects the fact that both boron heterogeneity and corrected radiobiological parameters were consistently integrated. Calculations that isolate the effect of radiobiological parameters correction alone, assuming a homogeneous boron distribution in the tumor (*Macro [RB-Micro] model*), resulted in a significant reduction in the estimated photon isoeffective dose values, around 28%. A perturbation analysis was finally performed, based on the premise that the heterogeneity observed *in vitro* may not be extrapolated to the tumor context. In fact, the degree of heterogeneity in boron uptake might be even greater in the tumor than that observed in the U-87 line. To explore this possibility, the cytoplasm-to-nucleus boron concentration ratio was still modeled as a lognormal distribution with a broader standard deviation (twice that measured in the experimental data) while keeping the expected value constant. This scenario reflects the plausible *in vivo* condition, where biological and physiological factors could amplify variability. This increased dispersion leads to a significant departure between the *Micro*- and *Macro Model*-based DVHs, with differences of around 22%, underscoring that the extent of cellular heterogeneity plays a crucial role in dose estimation and should not be overlooked in treatment planning. As future developments, it will be crucial to study boron concentration at the subcellular level from *in vivo* models, to understand how to properly tune this parameter in the

treatment planning.

The final part of this work focused on the development of a preliminary one-year Progression-Free Survival (1y-PFS) model, proposed as a figure of merit for the evaluation of GBM treatment, considering the inherent difficulties in calculating Tumor Control Probability (TCP) for this tumor type. Factors such as treatment-induced inflammation and edema complicate the direct assessment of tumor control, motivating the use of alternative endpoints such as PFS in the clinical setting. The 1y-PFS model, derived from clinical data of patients treated with conventional photon-fractionated radiotherapy, was transformed into single-fraction dose values. Moreover, to adapt it to BNCT where the dose distribution varies throughout the tumor volume much more than in photon therapy, it was necessary to define a single representative value of the BNCT dose to apply the model to BNCT patients. The concept of Equivalent Uniform Dose (EUD), defined as the uniform dose in a given volume that produces the same biological effect as the dose actually delivered non-uniformly, was adapted for the specific case of this thesis and used for the 1y-PSF. The parameters of the models were tuned using the previous clinical experience of BNCT in Finland. Once obtained a robust description of the 1y-PFS as a function of the Photon Isoeffective Dose, it was applied to patient cases to assess the clinical relevance of dosimetric differences. The results demonstrated that variations in dosimetry due to radiobiological parameter correction and cellular boron heterogeneity are directly reflected in predicted PFS values. In particular, differences between the Macro and Micro models were small (2–4%), whereas accounting for RB-corrected parameters led to substantial reductions in predicted 1y-PFS, up to 98%. This demonstrates how much the correct integration of microdosimetry into the models influences our ability to make reliable predictions on the clinical outcome of the irradiation. Furthermore, modeling increased variability in cellular boron distribution, consistent with plausible *in vivo* conditions, resulted in a clinically meaningful reduction in predicted PFS (15%).

Further studies on boron distribution in the tumor are thus necessary to determine whether the macroscopic approach is sufficient to represent the real dosimetry accurately. A promising future development is the refinement of PET imaging with boron-specific tracers. While in current clinical practice (e.g., in China) [^{18}F]-BPA-PET is already used to estimate boron uptake by dividing the tumor into groups of ^{10}B regions, an improved approach would be to implement a voxel-by-voxel macroscopic distribution of ^{10}B. Additionally, it would provide a more accurate boron uptake map based on the actual behavior of the therapeutic molecule. This approach would open the possibility of applying, locally for each voxel, a microdosimetric correction employing the η' factor and considering $f_A(a)$, thus obtaining a more accurate dose assessment. In this way, not only the boron distribution heterogeneity at the cellular level would be taken into account, but also its spatial heterogeneity at the macroscopic level within the tumor. This approach would result in a more accurate dose estimation, enhancing treatment personalization and efficacy. Having developed a microdosimetry model and analyzed the influence of geometrical parameters and boron microdistribution, the extension to other

targets of interest is straightforward.
Beyond the considerations about the tuning of the model to account for the microdosimetric aspects, the production of 1y-PFS model represents a valuable tool to evaluate dose distributions obtained in the treatment planning on the basis of a clinical criterion. In fact, today BNCT dosimetry has been basically descriptive, and follow up was never used as feedback for prediction models. A modern, more precise and effective BNCT will be only possible where we will gain the sufficient knowledge to link the dose distribution to the tumor control and the side effects. This thesis represents a step forward in this direction for the treatment of GBM with BNCT.
It is important to stress that the clinical application of the proposed models has been demonstrated through a single simulated case of GBM and a retrospective analysis of two patients treated with BNCT. Although this is sufficient for illustrative and demonstrative purposes within the scope of this work, such a small number does not allow for statistically robust clinical conclusions to be drawn.
It is therefore essential to emphasize that these applications are primarily intended to demonstrate the dosimetric feasibility and practical applicability of the proposed framework, rather than predicting clinical outcomes or therapeutic efficacy.
A quantitative assessment of the clinical impact and predictive capabilities of the models will necessarily require studies on significantly larger patient cohorts, which represent a next step in the development of this work.

The results described in this work contribute to the efforts for clinical application in Italy and Argentina, in the frame of the development of accelerator-based BNCT as a potential therapeutic option for patients that have no other possibilities. The aim is to innovate not only the technological tools to produce neutrons but also the approach of the dose calculation, the way to evaluate a treatment plan, and the criteria of the dose prescription.
The potential of BNCT in the treatment of GBM lies in its selectivity, that must be exploited at its fullest, building the necessary knowledge from the microscopic aspects studied in cells to the macroscopic perspective of the patient treatment. The presented findings confirm that the dose models developed in this work not only capture the physical and biological aspects of BNCT with greater fidelity but also provide a framework to quantitatively link dosimetric improvements to potential clinical outcomes, reinforcing the translational relevance of the present thesis.

BIBLIOGRAPHY

[1] Jeffrey A Coderre et al. «Boron neutron capture therapy: cellular targeting of high linear energy transfer radiation». In: *Technology in cancer research & treatment* 2.5 (2003), pp. 355–375.

[2] Andrea Monti Hughes and Naonori Hu. «Optimizing boron neutron capture therapy (BNCT) to treat cancer: an updated review on the latest developments on boron compounds and strategies». In: *Cancers* 15.16 (2023), p. 4091.

[3] Komal Anjum et al. «Current status and future therapeutic perspectives of glioblastoma multiforme (GBM) therapy: A review». In: *Biomedicine & Pharmacotherapy* 92 (2017), pp. 681–689.

[4] James J Vredenburgh et al. «Phase II trial of bevacizumab and irinotecan in recurrent malignant glioma». In: *Clinical cancer research* 13.4 (2007), pp. 1253–1259.

[5] Fausto J Rodriguez et al. «Epithelial and pseudoepithelial differentiation in glioblastoma and gliosarcoma: a comparative morphologic and molecular genetic study». In: *Cancer* 113.10 (2008), pp. 2779–2789.

[6] David N Louis et al. «The 2016 World Health Organization classification of tumors of the central nervous system: a summary». In: *Acta neuropathologica* 131.6 (2016), pp. 803–820.

[7] Luis Eduardo Werneck de Carvalho et al. «Central nervous system tumours profile at a referral center in the Brazilian Amazon region, 1997–2014». In: *PLoS One* 12.4 (2017), e0174439.

[8] Eric C Holland. «Glioblastoma multiforme: the terminator». In: *Proceedings of the National Academy of Sciences* 97.12 (2000), pp. 6242–6244.

[9] Seyed-Mostafa Razavi et al. «Immune evasion strategies of glioblastoma». In: *Frontiers in surgery* 3 (2016), p. 11.

[10] Shiao-Pei Weathers and Mark R Gilbert. «Current challenges in designing GBM trials for immunotherapy». In: *Journal of neuro-oncology* 123.3 (2015), pp. 331–337.

[11] Timothy N Phoenix et al. «Medulloblastoma genotype dictates blood brain barrier phenotype». In: *Cancer cell* 29.4 (2016), pp. 508–522.

[12] Elizabeth R Gerstner and Robert L Fine. «Increased permeability of the blood-brain barrier to chemotherapy in metastatic brain tumors: establishing a treatment paradigm». In: *Journal of clinical oncology* 25.16 (2007), pp. 2306–2312.

[13] HJ Scherer. «A critical review: the pathology of cerebral gliomas». In: *Journal of neurology and psychiatry* 3.2 (1940), p. 147.

[14] George St Stoyanov and Deyan L Dzhenkov. «On the concepts and history of glioblastoma multiforme—morphology, genetics and epigenetics». In: *Folia Med* 60.1 (2018), pp. 48–66.

[15] Felipe de Almeida Sassi et al. «Glioma revisited: from neurogenesis and cancer stem cells to the epigenetic regulation of the niche». In: *Journal of oncology* 2012.1 (2012), p. 537861.

[16] Inês Crespo et al. «Detailed characterization of alterations of chromosomes 7, 9, and 10 in glioblastomas as assessed by single-nucleotide polymorphism arrays». In: *The journal of Molecular Diagnostics* 13.6 (2011), pp. 634–647.

[17] Helmut Kettenmann and Alexei Verkhratsky. «Neuroglia: the 150 years after». In: *Trends in neurosciences* 31.12 (2008), pp. 653–659.

[18] Lisa M DeAngelis and Ingo K Mellinghoff. «Virchow 2011 or how to ID (H) human glioblastoma». In: *Journal of Clinical Oncology* 29.34 (2011), pp. 4473–4474.

[19] Ingeborg Bosma et al. «The course of neurocognitive functioning in high-grade glioma patients». In: *Neuro-oncology* 9.1 (2007), pp. 53–62.

[20] Christina A Meyers and Kenneth R Hess. «Multifaceted end points in brain tumor clinical trials: cognitive deterioration precedes MRI progression». In: *Neuro-oncology* 5.2 (2003), pp. 89–95.

[21] Roger Henriksson, Thomas Asklund, and Hans Skovgaard Poulsen. «Impact of therapy on quality of life, neurocognitive function and their correlates in glioblastoma multiforme: a review». In: *Journal of neuro-oncology* 104.3 (2011), pp. 639–646.

[22] Martin Klein et al. «Neurobehavioral status and health-related quality of life in newly diagnosed high-grade glioma patients». In: *Journal of clinical oncology* 19.20 (2001), pp. 4037–4047.

[23] Michael D Walker et al. «Evaluation of BCNU and/or radiotherapy in the treatment of anaplastic gliomas: a cooperative clinical trial». In: *Journal of neurosurgery* 49.3 (1978), pp. 333–343.

[24] Roger Stupp. «European Organisation for Research and Treatment of Cancer Brain Tumor and Radiotherapy Groups; National Cancer Institute of Canada Clinical Trials Group, Radiotherapy plus concomitant and adjuvant temozolomide for glioblastoma». In: *N. Engl. J. Med.* 352 (2005), pp. 987–996.

[25] Silvia Hofer and Richard Herrmann. «Chemotherapy for malignant brain tumors of astrocytic and oligodendroglial lineage». In: *Journal of cancer research and clinical oncology* 127.2 (2001), pp. 91–95.

[26] F Jin et al. «Comparison between cells and cancer stem-like cells isolated from glioblastoma and astrocytoma on expression of anti-apoptotic and multidrug resistance–associated protein genes». In: *Neuroscience* 154.2 (2008), pp. 541–550.

[27] Eric Barbarite et al. «The role of brachytherapy in the treatment of glioblastoma multiforme». In: *Neurosurgical review* 40.2 (2017), pp. 195–211.

[28] Nicole E Cross and Michael J Glantz. «Neurologic complications of radiation therapy». In: *Neurologic clinics* 21.1 (2003), pp. 249–277.

[29] T. Biswas et al. «Stereotactic radiosurgery for glioblastoma: retrospective analysis». In: *Radiation Oncology* 4.1 (2009), p. 11.

[30] Ian F. Parney and Susan M. Chang. «Current Chemotherapy for Glioblastoma». In: *The Cancerjournal* 9.3 (2003), pp. 149–156.

[31] Jens Overgaard. «Clinical evaluation of nitroimidazoles as modifiers of hypoxia in solid tumors». In: *Oncology research* 6.10-11 (1994), pp. 509–518.

[32] Michael D Prados et al. «A phase 3 randomized study of radiotherapy plus procarbazine, CCNU, and vincristine (PCV) with or without BUdR for the treatment of anaplastic astrocytoma: a preliminary report of RTOG 9404». In: *International journal of Radiation Oncology* Biology* Physics* 45.5 (1999), pp. 1109–1115.

[33] Shin-Ichi Miyatake et al. «Boron neutron capture therapy for malignant brain tumors». In: *Neurologia medico-chirurgica* 56.7 (2016), pp. 361–371.

[34] Tien-Li Lan et al. «Using salvage Boron Neutron Capture Therapy (BNCT) for recurrent malignant brain tumors in Taiwan». In: *Applied Radiation and Isotopes* 160 (2020), p. 109105.

[35] F Issa, JA Ioppolo, and LM Rendina. «Boron and gadolinium neutron capture therapy». In: *Bioinorganic Fundamentals and Applications: Metals in Natural Living Systems and Metals in Toxicology and Medicine* (2013), pp. 877–900.

[36] International Commission on Radiation Units and Measurements. *Radiation Quantities and Units*. ICRU Report 33. Washington, D.C.: ICRU, 1980.

[37] Jeffrey A Coderre et al. «Boron neutron capture therapy: cellular targeting of high linear energy transfer radiation». In: *Technology in cancer research & treatment* 2.5 (2003), pp. 355–375.

[38] Sara J González and Gustavo A Santa Cruz. «The photon-isoeffective dose in boron neutron capture therapy». In: *Radiation research* 178.6 (2012), pp. 609–621.

[39] Andrea Wittig and Wolfgang AG Sauerwein. «Clinical Trials in BNCT: A challenging task». In: *Neutron Capture Therapy: Principles and Applications*. Springer, 2012, pp. 369–376.

[40] W Sauerwein, A Zurlo, EORTC Boron Neutron Capture Therapy Group, et al. «The EORTC boron neutron capture therapy (BNCT) group: achievements and future projects». In: *European journal of cancer* 38 (2002), pp. 31–34.

[41] Teruyoshi Kageji et al. «Pharmacokinetics and boron uptake of BSH (Na2B12H11SH) in patients with intracranial tumors». In: *Journal of neuro-oncology* 33.1 (1997), pp. 117–130.

[42] Mariko Sato et al. «Safety of Boron Neutron capture therapy with Borofalan (10B) and its efficacy on recurrent head and neck cancer: real-world outcomes from nationwide post-marketing surveillance». In: *Cancers* 16.5 (2024), p. 869.

[43] Rolemae M. Murilla et al. «Boron delivery agents in BNCT: A mini review of current developments and emerging trends». In: *Nano TransMed* 4 (2025), p. 100081.

[44] Tianyun Zhou et al. «The current status and novel advances of boron neutron capture therapy clinical trials». In: *American journal of Cancer Research* 14.2 (2024), p. 429.

[45] «BNCT for skin melanoma in extremities: Updated Argentine clinical results». In: *Applied Radiation and Isotopes* 67.7, Supplement (2009), S50–S53.

[46] M.E. Capoulat et al. «Accelerator based-BNCT facilities worldwide and an update of the Buenos Aires project». In: *Applied Radiation and Isotopes* 219 (2025), p. 111723.

[47] Daniel N Slatkin. «A history of boron neutron capture therapy of brain tumours: postulation of a brain radiation dose tolerance limit». In: *Brain* 114.4 (1991), pp. 1609–1629.

[48] Yoshinobu Nakagawa and Hiroshi Hatanaka. «Boron neutron capture therapy: Clinical brain tumor studies». In: *Journal of Neuro-Oncology* 33.1 (1997), pp. 105–115.

[49] Maaike J. Vos et al. «Radiologic findings in patients treated with boron neutron capture therapy for glioblastoma multiforme within EORTC trial 11961». In: *International journal of Radiation Oncology*Biology*Physics* 61.2 (2005), pp. 392–399.

[50] Heikki Joensuu et al. «Boron neutron capture therapy of brain tumors: clinical trials at the Finnish facility using boronophenylalanine». In: *Journal of Neuro-Oncology* 62.1 (2003), pp. 123–134.

[51] Rolf Barth et al. «Current status of boron neutron capture therapy of high grade gliomas and recurrent head and neck cancer». In: *Radiation oncology (London, England)* 7 (Aug. 2012), p. 146. DOI: 10.1186/1748-717X-7-146.

[52] K Sköld et al. «Boron Neutron Capture Therapy for glioblastoma multiforme: advantage of prolonged infusion of BPA-f». In: *Acta Neurologica Scandinavica* 122.1 (2010), pp. 58–62.

[53] Roger Henriksson et al. «Boron neutron capture therapy (BNCT) for glioblastoma multiforme: a phase II study evaluating a prolonged high-dose of boronophenylalanine (BPA)». In: *Radiotherapy and Oncology* 88.2 (2008), pp. 183–191.

[54] Hiroshi Hatanaka and Yoshinobu Nakagawa. «Clinical results of long-surviving brain tumor patients who underwent boron neutron capture therapy». In: *International journal of Radiation Oncology* Biology* Physics* 28.5 (1994), pp. 1061–1066.

[55] Tetsuya Yamamoto et al. «Boron neutron capture therapy for newly diagnosed glioblastoma». In: *Radiotherapy and oncology* 91.1 (2009), pp. 80–84.

[56] Shin-Ichi Miyatake et al. «Survival benefit of Boron neutron capture therapy for recurrent malignant gliomas». In: *Journal of Neuro-Oncology* 91.2 (2009), pp. 199–206.

[57] Shin-Ichi Miyatake et al. «Survival benefit of Boron neutron capture therapy for recurrent malignant gliomas». In: *Journal of Neuro-Oncology* 91.2 (2009), pp. 199–206.

[58] Shin-Ichi Miyatake et al. «Modified boron neutron capture therapy for malignant gliomas performed using epithermal neutron and two boron compounds with different accumulation mechanisms: an efficacy study based on findings on neuroimages». In: *Journal of neurosurgery* 103.6 (2005), pp. 1000–1009.

[59] Shinji Kawabata et al. «Boron neutron capture therapy for newly diagnosed glioblastoma». In: *Journal of radiation research* 50.1 (2009), pp. 51–60.

[60] Hiroyuki Shiba et al. «Boron neutron capture therapy combined with early successive bevacizumab treatments for recurrent malignant gliomas–a pilot study». In: *Neurologia medico-chirurgica* 58.12 (2018), pp. 487–494.

[61] Shinji Kawabata et al. «Accelerator-based BNCT for patients with recurrent glioblastoma: a multicenter phase II study». In: *Neuro-oncology advances* 3.1 (2021), vdab067.

[62] T Yamamoto et al. «Current clinical results of the Tsukuba BNCT trial». In: *Applied Radiation and Isotopes* 61.5 (2004), pp. 1089–1093.

[63] Yi-Wei Chen et al. «Salvage Boron Neutron Capture Therapy for Malignant Brain Tumor Patients in Compliance with Emergency and Compassionate Use: Evaluation of 34 Cases in Taiwan». In: *Biology* 10.4 (2021).

[64] J.W. Hopewell et al. «The radiobiological principles of boron neutron capture therapy: A critical review». In: *Applied Radiation and Isotopes* 69.12 (2011), pp. 1756–1759.

[65] Edward L Alpen. *Radiation biophysics*. Academic press, 1997.

[66] Jeffrey A Coderre and Gerard M Morris. «The radiation biology of boron neutron capture therapy». In: *Radiation research* 151.1 (1999), pp. 1–18.

[67] SJ González et al. «Photon iso-effective dose for cancer treatment with mixed field radiation based on dose–response assessment from human and an animal model: clinical application to boron neutron capture therapy for head and neck cancer». In: *Physics in Medicine & Biology* 62.20 (2017), p. 7938.

[68] Thomas E Schmid et al. «Differences in the kinetics of γ-H2AX fluorescence decay after exposure to low and high LET radiation». In: *International journal of radiation biology* 86.8 (2010), pp. 682–691.

[69] Harald H Rossi. «Specification of radiation quality». In: *Radiation research* 10.5 (1959), pp. 522–531.

[70] Harald H Rossi and Walter Rosenzweig. «A device for the measurement of dose as a function of specific ionization». In: *Radiology* 64.3 (1955), pp. 404–411.

[71] Albrecht M Kellerer and D Chmelevsky. «Concepts of microdosimetry: III. Mean values of the microdosimetric distributions». In: *Radiation and Environmental Biophysics* 12.4 (1975), pp. 321–335.

[72] Albrecht M Kellerer and D Chmelevsky. «Concepts of microdosimetry: II. Probability distributions of the microdosimetry variables». In: *Radiation and Environmental Biophysics* 12.3 (1975), pp. 205–216.

[73] Albrecht M Kellerer and D Chmelevsky. «Concepts of microdosimetry: III. Mean values of the microdosimetric distributions». In: *Radiation and Environmental Biophysics* 12.4 (1975), pp. 321–335.

[74] M Zaider, By Harald H Rossi, and Marco Zaider. *Microdosimetry and its Applications*. Springer, 1996.

[75] Aneta Kawa-Iwanicka et al. «Dose distribution homogeneity in two TBI techniques—Analysis of 208 irradiated patients conducted in Stanislaw Leszczynski Memorial Hospital, Katowice». In: *Reports of Practical Oncology and Radiotherapy* 17.6 (2012), pp. 367–375.

[76] R. G. Zamenhof. «Microdosimetry for boron neutron capture therapy: A review». In: *Journal of Neuro-Oncology* 33.1-2 (May 1997), pp. 81–92. DOI: 10.1023/A:1005725415807.

[77] C. S. Wuu et al. «Microdosimetry for boron neutron capture therapy». In: *Radiation Research* 130 (1992), pp. 355–359.

[78] Gustavo A Santa Cruz and Robert G Zamenhof. «The microdosimetry of the 10B reaction in boron neutron capture therapy: a new generalized theory». In: *Radiation research* 162.6 (2004), pp. 702–710.

[79] Yang Han et al. «Microdosimetric analysis for boron neutron capture therapy via Monte Carlo track structure simulation with modified lithium cross-sections». In: *Radiation Physics and Chemistry* 209 (2023), p. 110956.

[80] Tatsuhiko Sato et al. «Microdosimetric modeling of biological effectiveness for boron neutron capture therapy considering intra-and intercellular heterogeneity in 10B distribution». In: *Scientific reports* 8.1 (2018), p. 988.

[81] Andrea Wittig et al. «Boron analysis and boron imaging in biological materials for boron neutron capture therapy (BNCT)». In: *Critical reviews in oncology/hematology* 68.1 (2008), pp. 66–90.

[82] International Atomic Energy Agency. *Advances in Boron Neutron Capture Therapy*. Vienna: International Atomic Energy Agency, 2023.

[83] R. L. Fleischer, P. Price, and R. M. Walker. *Nuclear Tracks in Solids*. Berkeley: University of California Press, 1975.

[84] S. A. Durrani, R. K. Bull, and D. ter Haar. *Solid State Nuclear Track Detection: Principles, Methods and Applications*. Oxford: Pergamon Press, 1987.

[85] Shi-Lun Guo, Bao-Liu Chen, and S. A. Durrani. «Solid-State Nuclear Track Detectors». In: *Handbook of Radioactivity Analysis*. Ed. by Michael F. L'Annunziata. San Diego, CA: Academic Press, 2004. Chap. 4, pp. 234–289.

[86] H. A. Khan and I. E. Qureshi. «Title not provided». In: *Radiation Measurements* 31 (1999), pp. 25–36. ISSN: 1350-4487.

[87] G. S. Martin, L. López, and O. A. Bernaola. «Neutron dosimetry device using PADC nuclear track detectors». In: *Journal of Radioanalytical and Nuclear Chemistry* 287.2 (2011), pp. 635–638. DOI: 10.1007/s10967-010-0835-7.

[88] T Konishi et al. «Imaging uranium distribution on rat kidney sections through detection of alpha tracks using CR-39 plastic nuclear track detector». In: *Radiation Protection Dosimetry* 183.1-2 (2019), pp. 242–246.

[89] RL Fleischer. «Nuclear track production in solids». In: *Chalmers anniversary volume*. 1981, pp. 97–123.

[90] Maria Sol Espain et al. «Optical density of high fluence autoradiographic images to study boron microdistribution: validation of the technique in tissue sections». In: *Frontiers in Nuclear Engineering* 3 (2024), p. 1363880.

[91] Agustina M Portu et al. «Neutron autoradiography with nuclear tracks detectors: an imaging technique for Boron Neutron Capture Therapy». In: *Journal of Physics: Conference Series*. Vol. 2605. 1. IOP Publishing. 2023, p. 012010.

[92] A. Portu et al. «Measurement of 10B concentration through autoradiography images in polycarbonate nuclear track detectors». In: *Radiation Measurements* 46.10 (2011), pp. 1154–1159.

[93] G Somogyi and I Hunyadi. «Etching properties of the CR-39 polymeric nuclear track detector». In: *Solid State Nuclear Track Detectors*. Elsevier, 1980, pp. 443–452.

[94] Agustina Portu et al. «Simultaneous observation of cells and nuclear tracks from the boron neutron capture reaction by UV-C sensitization of polycarbonate». In: *Microscopy and Microanalysis* 21.4 (2015), pp. 796–804.

[95] A Portu et al. «Qualitative autoradiography with polycarbonate foils enables histological and track analyses on the same section». In: *Biotechnic & Histochemistry* 88.5 (2013), pp. 217–221.

[96] Hiroki Tanaka et al. «Development of a simple and rapid method of precisely identifying the position of 10B atoms in tissue: an improvement in standard alpha autoradiography». In: *Journal of radiation research* 55.2 (2014), pp. 373–380.

[97] GR Solares and RG Zamenhof. «A novel approach to the microdosimetry of neutron capture therapy. Part I. High-resolution quantitative autoradiography applied to microdosimetry in neutron capture therapy». In: *Radiation research* 144.1 (1995), pp. 50–58.

[98] K Amemiya et al. «Soft X-ray imaging using CR-39 plastics with AFM readout». In: *Nuclear Instruments and Methods in Physics Research Section B: Beam Interactions with Materials and Atoms* 187.3 (2002), pp. 361–366.

[99] GR Solares and RG Zamenhof. «A novel approach to the microdosimetry of neutron capture therapy. Part I. High-resolution quantitative autoradiography applied to microdosimetry in neutron capture therapy». In: *Radiation research* 144.1 (1995), pp. 50–58.

[100] Mario A Gadan et al. «Neutron autoradiography combined with UV-C sensitization: toward the intracellular localization of boron». In: *Microscopy and Microanalysis* 25.6 (2019), pp. 1331–1340.

[101] R. Ramani and C. Ranganathaiah. «Degradation of acrylonitrile-butadiene-styrene and polycarbonate by UV irradiation». In: *Polymer Degradation and Stability* 69.3 (2000), pp. 347–354.

[102] Agnès Rivaton, Daniel Sallet, and Jacques Lemaire. «The photo-chemistry of bisphenol-A polycarbonate reconsidered: Part 2—FTIR analysis of the solid-state photo-chemistry in 'dry'conditions». In: *Polymer degradation and stability* 14.1 (1986), pp. 1–22.

[103] Agnès Rivaton. «Recent advances in bisphenol-A polycarbonate photodegradation». In: *Polymer Degradation and Stability* 49.1 (1995), pp. 163–179.

[104] Agustina Mariana Portu et al. «Experimental set up for the irradiation of biological samples and nuclear track detectors with UV C». In: *Reports of Practical Oncology and Radiotherapy* 21.2 (2016), pp. 129–134.

[105] G. Saint Martin et al. «UV-C radiation effect on nuclear tracks of different ions in polycarbonate». In: *Radiation Physics and Chemistry* 173 (2020), p. 108936.

[106] David N Louis et al. «The 2007 WHO classification of tumours of the central nervous system». In: *Acta neuropathologica* 114.2 (2007), pp. 97–109.

[107] C Ryan Miller and Arie Perry. «Glioblastoma: morphologic and molecular genetic diversity». In: *Archives of pathology & laboratory medicine* 131.3 (2007), pp. 397–406.

[108] Bertrand Actor et al. «Comprehensive analysis of genomic alterations in gliosarcoma and its two tissue components». In: *Genes, Chromosomes and Cancer* 34.4 (2002), pp. 416–427.

[109] Rudolf H Boerman et al. «The glial and mesenchymal elements of gliosarcomas share similar genetic alterations». In: *Journal of Neuropathology & Experimental Neurology* 55.9 (1996), pp. 973–981.

[110] James R Perry et al. «Clinicopathologic features of primary and postirradiation cerebral gliosarcoma». In: *Cancer* 75.12 (1995), pp. 2910–2918.

[111] Johannes Lutterbach, Roland Guttenberger, and Axel Pagenstecher. «Gliosarcoma: a clinical study». In: *Radiotherapy and oncology* 61.1 (2001), pp. 57–64.

[112] Irwin H Feigin and Sidney W Gross. «Sarcoma arising in glioblastoma of the brain». In: *The American journal of pathology* 31.4 (1955), p. 633.

[113] T. Ehrenreich and J. F. Devlin. «A complex of glioblastoma and spindle-cell sarcoma with pulmonary metastasis». In: *A.M.A. Archives of Pathology* 66.4 (1958), pp. 536–549.

[114] Maj Donald R Smith, Ltc John M Hardman, and Kenneth M Earle. «Contiguous glioblastoma multiforme and fibrosarcoma with extracranial metastasis». In: *Cancer* 24.2 (1969), pp. 270–276.

[115] Thomas L Beaumont et al. «Gliosarcoma with multiple extracranial metastases: case report and review of the literature». In: *Journal of neuro-oncology* 83.1 (2007), pp. 39–46.

[116] Lise Mette Gjerdrum and M Bojsen-Møller. «October 1998–61 year old male with brain tumor and oral, lung, and palpebral masses.» In: *Brain pathology (Zurich, Switzerland)* 9.2 (1999), pp. 421–422.

[117] David Weaver et al. «Selective peripancreatic sarcoma metastases from primary gliosarcoma: case report». In: *Journal of neurosurgery* 61.3 (1984), pp. 599–601.

[118] Fausto J Rodriguez et al. «Gliosarcoma arising in oligodendroglial tumors ("oligosarcoma"): a clinicopathologic study». In: *The American journal of surgical pathology* 31.3 (2007), pp. 351–362.

[119] Guobin Zhang et al. «Clinical outcome of gliosarcoma compared with glioblastoma multiforme: a clinical study in Chinese patients». In: *Journal of neuro-oncology* 127.2 (2016), pp. 355–362.

[120] Marie Allen et al. «Origin of the U87MG glioma cell line: Good news and bad news». In: *Science translational medicine* 8.354 (2016), 354re3–354re3.

[121] Ana Mailén Dattoli Viegas et al. «Detailed dosimetry calculation for in-vitro experiments and its impact on clinical BNCT». In: *Physica Medica* 89 (2021), pp. 282–292.

[122] S Bortolussi et al. «Neutron flux and gamma dose measurement in the BNCT irradiation facility at the TRIGA reactor of the University of Pavia». In: *Nuclear Instruments and Methods in Physics Research Section B: Beam Interactions with Materials and Atoms* 414 (2018), pp. 113–120.

[123] Ian Postuma et al. «An improved neutron autoradiography set-up for B concentration measurements in biological samples». In: *Reports of practical oncology and radiotherapy* 21.2 (2016), pp. 123–128.

[124] Laura Cansolino et al. «Comparative study of the radiobiological effects induced on adherent vs suspended cells by BNCT, neutrons and gamma rays treatments». In: *Applied Radiation and Isotopes* 106 (2015), pp. 226–232.

[125] Claretta Guidi. «Irradiation of Reconstructed Human Skin Cultivated In-vitro: Computational Dosimetry and Preliminary Radiobiological Evaluations for BNCT Studies». Supervisor: Silva Bortolussi, Co-supervisor: Dr. Ian Postuma. Master's thesis. Università degli Studi di Pavia - Facoltà di Scienze MM. FF. NN., 2019.

[126] T. Goorley et al. *MCNP6 User's Manual, Version 6.1.1.* Technical Report LA-UR-14-24680. Los Alamos National Laboratory, 2014.

[127] Erica Simeone. «Studi dosimetrici per la BNCT del Glioblastoma Multiforme con acceleratore». Anno accademico 2021/2022. Supervisor: Silva Bortolussi, Co-supervisor: Dott. Ian Postuma. Tesi di Laurea Magistrale. Università degli Studi di Pavia - Facoltà di Scienze MM. FF. NN., 2022.

[128] Cholpon S Djuzenova et al. «Differential response of human glioblastoma cell lines to combined camptothecin and ionizing radiation treatment». In: *Cancer Biology & Therapy* 7.3 (2008), pp. 364–373.

[129] Ming Tsuey Chew et al. «Potential lethal damage repair in glioblastoma cells irradiated with ion beams of various types and levels of linear energy transfer». In: *Journal of radiation research* 60.1 (2019), pp. 59–68.

[130] Thomas E Schmid et al. «Differences in the kinetics of γ-H2AX fluorescence decay after exposure to low and high LET radiation». In: *International journal of radiation biology* 86.8 (2010), pp. 682–691.

[131] Yusuke Matsuya et al. «Quantitative estimation of DNA damage by photon irradiation based on the microdosimetric-kinetic model». In: *Journal of Radiation Research* 55.3 (2014), pp. 484–493.

[132] Jeffrey A Coderre and Gerard M Morris. «The radiation biology of boron neutron capture therapy». In: *Radiation research* 151.1 (1999), pp. 1–18.

[133] B Marcaccio et al. «Towards an adequate description of the dose-response relationship in BNCT of glioblastoma multiforme». In: *Medical Physics* 52.4 (2025), pp. 2606–2617.

[134] Python Software Foundation. *Python Language Reference, version 3.9*. https://www.python.org/. 2020.

[135] Cristina Pezzi et al. «Dosimetric comparison of the BNCT treatment planning performances when using a nnU-NET to automatically segment Glioblastoma Multiforme». In: *Health and Technology* (2025), pp. 1–12.

[136] Hong-Ming Liu. «Beam Collimator Design for the Epithermal Neutron Beam at the Tsing Hua Open-Pool Reactor (THOR)». In: *Frontiers in Neutron Capture Therapy: Volume 1*. Springer, 2001, pp. 325–329.

[137] Kunio Yokoyama et al. «Pharmacokinetic study of BSH and BPA in simultaneous use for BNCT». In: *Journal of Neuro-oncology* 78.3 (2006), pp. 227–232.

[138] Ian Postuma et al. «A novel approach to design and evaluate BNCT neutron beams combining physical, radiobiological, and dosimetric figures of merit». In: *Biology* 10.3 (2021), p. 174.

[139] Sara J González et al. «Voxel model in BNCT treatment planning: performance analysis and improvements». In: *Physics in Medicine & Biology* 50.3 (2005), p. 441.

[140] A. Allisy et al. *ICRU Report 44: Tissue Substitutes in Radiation Dosimetry and Measurement*. Technical Report 44. International Commission on Radiation Units and Measurements, 1989.

[141] Giuliano Franco Perotti Bernardini et al. «Comparison of photon isoeffective dose models based on in vitro and in vivo radiobiological experiments for head and neck cancer treated with bnct». In: *Radiation Research* 198.2 (2022), pp. 134–144.

[142] Tatsuhiko Sato et al. «Microdosimetric modeling of biological effectiveness for boron neutron capture therapy considering intra-and intercellular heterogeneity in 10B distribution». In: *Scientific reports* 8.1 (2018), p. 988.

[143] Kristin J Redmond, Minesh Mehta, and Minesh P Mehta. «Stereotactic radiosurgery for glioblastoma». In: *Cureus* 7.12 (2015).

[144] Adomas Bunevicius et al. «Stereotactic radiosurgery for glioblastoma considering tumor genetic profiles: an international multicenter study». In: *Journal of Neurosurgery* 137.1 (2021), pp. 42–50.

[145] Leena Kankaanranta et al. «L-boronophenylalanine-mediated boron neutron capture therapy for malignant glioma progressing after external beam radiation therapy: a Phase I study». In: *International journal of Radiation Oncology* Biology* Physics* 80.2 (2011), pp. 369–376.

[146] Yi-Chiao Teng et al. «Correcting for the heterogeneous boron distribution in a tumor for BNCT dose calculation». In: *Scientific Reports* 13.1 (2023), p. 15741.

[147] S Chandra et al. «Quantitative evaluation of boron neutron capture therapy (BNCT) drugs for boron delivery and retention at subcellular-scale resolution in human glioblastoma cells with imaging secondary ion mass spectrometry (SIMS)». In: *Journal of microscopy* 254.3 (2014), pp. 146–156.

[148] Leena Kankaanranta et al. «Boron neutron capture therapy (BNCT) followed by intensity modulated chemoradiotherapy as primary treatment of large head and neck cancer with intracranial involvement». In: *Radiotherapy and Oncology* 99.1 (2011), pp. 98–99.

[149] Susana Maria Oliveira et al. «Dosimetric effect of tissue heterogeneity for I prostate implants». In: *Reports of Practical Oncology and Radiotherapy* 19.6 (2014), pp. 392–398.

[150] G Saint Martin et al. «Stochastic simulation of track density in nuclear track detectors for 10B measurements in autoradiography». In: *Nuclear Instruments and Methods in Physics Research Section B: Beam Interactions with Materials and Atoms* 269.23 (2011), pp. 2781–2785.

[151] Laura Cansolino et al. «Comparative study of the radiobiological effects induced on adherent vs suspended cells by BNCT, neutrons and gamma rays treatments». In: *Applied Radiation and Isotopes* 106 (2015), pp. 226–232.

[152] M Miller et al. «New irradiation facility for biomedical applications at the RA-3 reactor thermal column». In: *Applied Radiation and Isotopes* 67.7-8 (2009), S226–S229.

[153] M Gadan et al. «Preliminary liver dose estimation in the new facility for biomedical applications at the RA-3 reactor». In: *Applied Radiation and Isotopes* 67.7-8 (2009), S206–S209.

[154] Marcelo E Miller et al. «Rhodium self-powered neutron detector as a suitable on-line thermal neutron flux monitor in BNCT treatments». In: *Medical Physics* 38.12 (2011), pp. 6502–6512.

[155] The MathWorks Inc. *MATLAB version: 9.13.0 (R2022b)*. Natick, Massachusetts, United States, 2022. URL: https://www.mathworks.com.

[156] M. A. Gadan. «Estudio y caracterización de los distintos aspectos físicos para el tratamiento del cáncer de mama HER2+ y sus recaídas con BNCT empleando liposomas como transportadores de boro». Spanish. PhD Thesis. Universidad Nacional de San Martín, 2022.

[157] G Saint Martin et al. «UV-C radiation effect on nuclear tracks of different ions in polycarbonate». In: *Radiation Physics and Chemistry* 173 (2020), p. 108936.

[158] Yan Wu et al. «Optimization of subcellular boron distribution measurement using UV-C imprint and neutron autoradiography in boron neutron capture therapy». In: *Radiation Measurements* 181 (2025), p. 107351.

[159] Richard E Carson. «Precision and accuracy considerations of physiological quantitation in PET». In: *Journal of Cerebral Blood Flow & Metabolism* 11.1_suppl (1991), A45–A50.

[160] J Martin Bland and Douglas G Altman. «Statistics Notes: Transforming data». In: *BMJ* 312.7033 (1996), p. 770.

[161] Sara González. «Developments in computational dosimetry and treatment optimization for boron neutron capture therapy». Ph.D. Thesis. Universidad de Buenos Aires, Facultad de Ciencias Exactas y Naturales, Departamento de Física, 2005.

[162] M Miller et al. «New irradiation facility for biomedical applications at the RA-3 reactor thermal column». In: *Applied Radiation and Isotopes* 67.7-8 (2009), S226–S229.

[163] Agustina Portu et al. «Inter-comparison of boron concentration measurements at INFN-University of Pavia (Italy) and CNEA (Argentina)». In: *Applied Radiation and Isotopes* 105 (2015), pp. 35–39.

[164] Tatsuhiko Sato et al. «Recent improvements of the particle and heavy ion transport code system–PHITS version 3.33». In: *Journal of Nuclear Science and Technology* 61.1 (2024), pp. 127–135.

[165] Weida Wu et al. «Plasma membrane folding enables constant surface area-to-volume ratio in growing mammalian cells». In: *Current Biology* 35.7 (2025), pp. 1601–1611.

[166] Piernicola Pedicini et al. «Clinical radiobiology of glioblastoma multiforme: estimation of tumor control probability from various radiotherapy fractionation schemes». In: *Strahlentherapie und Onkologie* 190.10 (2014), pp. 925–932.

[167] Alexandru Dasu, Iuliana Toma-Dasu, and Jack F Fowler. «Should single or distributed parameters be used to explain the steepness of tumour control probability curves?» In: *Physics in Medicine & Biology* 48.3 (2003), p. 387.

[168] Paul Okunieff et al. «Radiation dose-response of human tumors». In: *International journal of Radiation Oncology* Biology* Physics* 32.4 (1995), pp. 1227–1237.

[169] Andrzej Niemierko. «Reporting and analyzing dose distributions: a concept of equivalent uniform dose». In: *Medical physics* 24.1 (1997), pp. 103–110.

[170] Ana Mailén Dattoli Viegas et al. «Predicting radiotoxic effects after BNCT for brain cancer using a novel dose calculation model». In: *Physica Medica* 128 (2024), p. 104840.

[171] Jeffrey A Coderre et al. «Derivations of relative biological effectiveness for the high-LET radiations produced during boron neutron capture irradiations of the 9L rat gliosarcoma in vitro and in vivo». In: *International journal of Radiation Oncology* Biology* Physics* 27.5 (1993), pp. 1121–1129.

APPENDIX A
CALIBRATION CURVE

In [92], the experimental set up concerning the calibration curve is described in detail. To determine the correlation between density and boron-10 concentration, small Lexan Cases (SLCs) were constructed and assembled using cut sheets in a rectangular shape (25 mm × 15 mm). Two 'L' shaped spacers were applied to define a uniform thickness of 0.25 mm. The entire system was then closed and sealed with a solution of polycarbonate and chloroform (see Fig. A.1).
The resulting containers, with a usable volume of approximately 100 μL, were filled with boron-10 solutions (99.99% purity) at concentrations ranging from 0 to 100 ppm, allowing for subsequent exposure to neutrons and analysis by autoradiography to determine the concentration-dependent response of the detector.

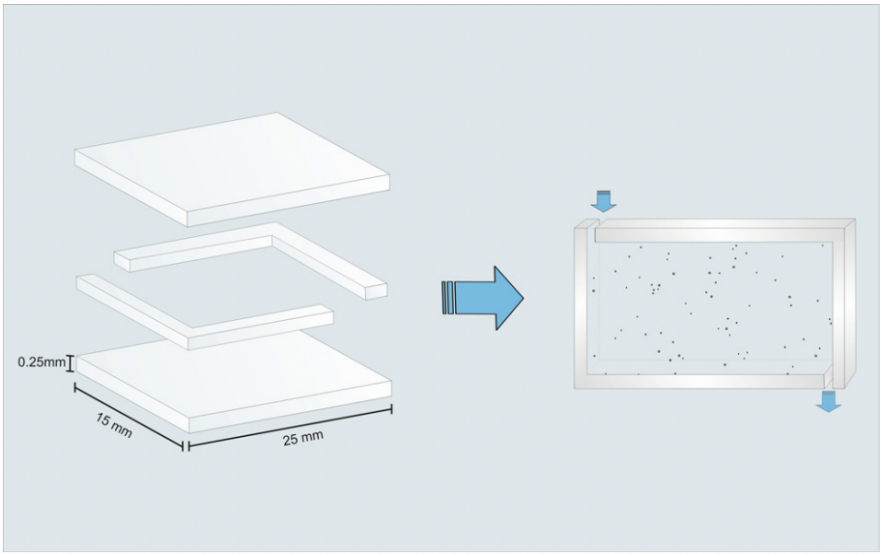

Figure A.1: *Small Lexan Cases system (SLCs): scheme of the construction process. Illustration from [92]*

Figure A.2 shows the calibration curve, obtained under the same conditions as those used for the neutron autoradiography experiments conducted on U-87 cells, specifically with a neutron fluence of 10^{12} n · cm^{-2} and an etching time of 4 minutes. This ensures consistency between the calibration phase and biological measurements.

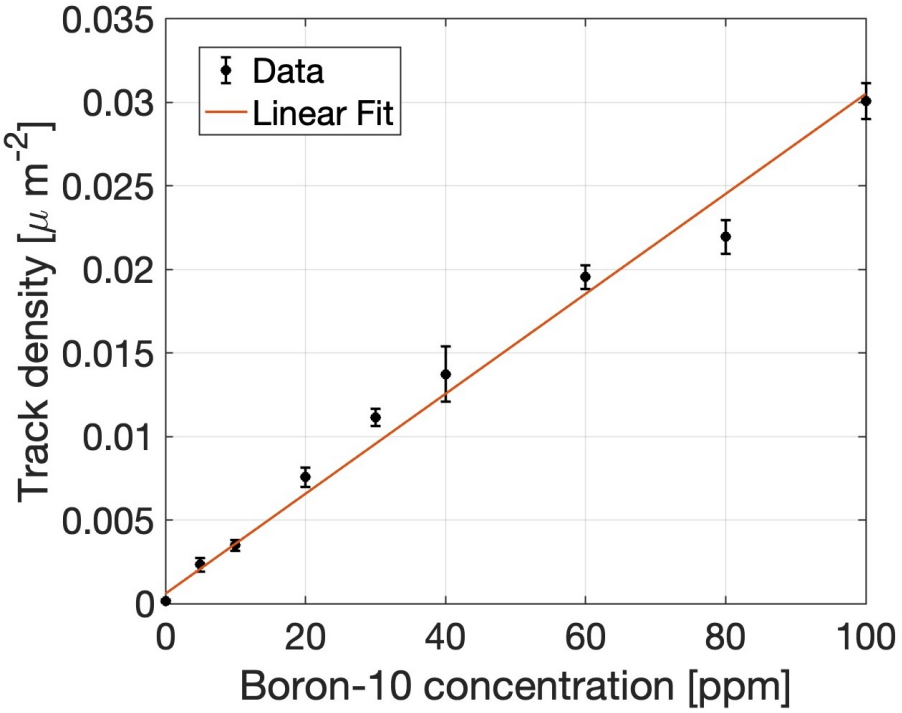

Figure A.2: *Track density versus ^{10}B concentration in aqueous solution for 10^{13} n · cm^{-2} neutron fluences. slope = $3.11 \cdot 10^{-4}$, intercept = $5.88 \cdot 10^{-4}$*

APPENDIX B

SUMMARY OF RESULT OF CHAPTER II.2

Summary of radiobiological and repair parameters for GBM				
(A) SLD repair kinetics				
	Characteristic time [min]	Low LET [%]	High LET [%]	
		Photons	Neutrons/Boron*	
t_{0f}	91 ± 45	$0.77 \pm 0.54^{\dagger}$	0.2	
t_{0s}	1238 ± 1237	0.23 ± 0.54	0.8	
(B) Radiobiological parameters				
	^{60}Co photons		160 kVp X-rays	
	Neutrons	Boron	Neutrons	Boron
α [Gy^{-1}]	0.5 ± 0.9	3.0 ± 0.6	0.1 ± 0.9	3.0 ± 0.6
β [Gy^{-2}]	0.5 ± 0.6	0	0.5 ± 0.6	0
(C) RBE and CBE values				
	^{60}Co		X-ray	Clinic
RBE$_{1\%}$	4.8 ± 0.7		2.5 ± 1.4	3.2
CBE$_{1\%}$	7.5 ± 0.9		4.7 ± 1.5	3.8

Table B.1: *Summary of (A) SLD repair kinetics parameters, (B) radiobiological parameters obtained from survival curve fits, and (C) RBE$_{1\%}$ and CBE$_{1\%}$ values for GBM cells. Uncertainties correspond to a 68% confidence level. †Constant c in Eq. II.1.4. *High-LET data from [130].*

Vent'anni di scrittura
son come una frittura
ruffiana e inadempiente
di pesce già pescato
da tempo congelato
e forse puzzolente.
Chi mai saprà se è vero
quello che nero è stato
se intorno al nero andato
il bianco sia più vero.
Se è stato sufficiente
riscrivere il passato
se dentro ogni dettato
il bello è prevalente.
Resta il sapore antico
di forme ricercate
genuine o riciclate
resta un sapore amico,
che aiuta nei momenti
depressi e tormentati:
i versi indovinati
generano sentimenti.

Massimo Marcaccio